Polyelectrolyte Building Blocks for Nanotechnology: Atomic Force Microscopy Investigations of Polyelectrolyte – Lipid Interactions, Polyelectrolyte Brushes and Viral Cages

Dissertation zur Erlangung des Doktorgrades der Naturwissenschaften der Fakultät für Physik der Universität Leipzig

Vorgelegt von

José Luis Cuéllar Camacho

aus San Luis Potosí

30.01.2013

Leipzig 2012

Acknowledgements

First of all, I would like to thank Professor Edwin Donath for the opportunity to take me as a Ph.D. student at the University of Leipzig and to invite me to work in his group at the Medical Institute of Physics and Biophysics. Also, to share with me the scientific enthusiasm, interchange of ideas and invaluable helpful discussions. I would like to thank him for the enormous patience and the great freedom during this period.

I would like to thank Professor Sergio Moya to offer me the connection to do my Ph.D. in Leipzig and to let me work with his team at the CICBiomagune in San Sebastian. For the parallel collaboration with Spain, to Iranzu and Jagoba which work with me in the characterization of the Polyelectrolyte brushes.

To Martin Fischlechner, for the frequent motivating discussions on bionanotechnology and virus related topics. To Guido Köhler for his guidance on my initial steps to use the AFM and for fruitful discussions on the mechanics of Rubella VLPs.

To Felix Meinhövel and Thomas Beruda to allow me the exciting opportunity to advise their research topics and for the uncountable measurements we performed and discussed together. Also to Paula Pescador, for teaching us the secrets of surface functionalization.

To Irina, for initial discussions on the topic of polyelectrolyte adsorption and multilayers. To Uta Reibetanz, Marco Dorn and Jana Flederman for their helpful advices on biological issues the many times they save me when working with cells. To Elke Typelt for the enormous patience and efficiency with the instruments in the lab in the last years.

To my splendid ad friendly coworkers Maria, Sophie and Martin which whom not only through nice scientific talks in company with a good coffee allowed me to

enjoy from Leipzig, but also for the great company and friendship they gave to have the chance for a delightful stay in Germany.

To my entertaining and always convivial roomates on the Riemman street for the countless occasions we had a good time together.

I would like to enormously thank my family for the great comprehension and constant support I have always received from them.

To Cynthia for having such a confidence on me and back me up in the pursue of my Ph.D. abroad.

To David González and David Alvaréz, for their constant friendship, support and interesting scientific discussions through the last years.

Finally I would like to thank CONACYT in Mexico for the unique opportunity to study abroad with an excellent scholarship.

Content

1. Introduction

1.1 From single molecules to self-assembled materials for nanotechnology

The XXth century witnessed groundbreaking discoveries in the physical sciences with the development of quantum mechanics, the theory of relativity and the description of chaotic systems as the most remarkable examples. Richard Feynman famous for his contribution to quantum field theory was convinced that that science and technology could bring a wealth of new opportunities and challenges when looking into the nanoscale (1 – 1000 nm). He acknowledged the relevance of fundamental physical phenomena occurring in the nanodimension giving emphasis to the biological machinery with proteins as remarkable nanoactuators. The complexity of living systems could be then unveiled by explaining the behavior of its individual parts.

Entities at the nanoscale experiences forces and effects usually negligible or even absent between macroscopic objects. In the nanoscale, gravitational effects are discarded, while the ratio volume to surface among interacting particles becomes dominant. Even when the laws of physics are the same in both scales, the mode of operation among the interacting subunits are subject to new effects.

For example thermal motion of molecules becomes increasingly important at smaller dimensions. The 3D-configuration of long chain molecules in solution like DNA is governed by the Brownian motion of the surrounding water molecules. The description of their behavior at the single molecular level by statistical models like the Freely Jointed Chain model (FJC) or the Worm-Like Chain model (WLC) has importantly contributed to understand their behavior.

On the other hand, organization plays a central role at the nanoscale since individual elements gather to form larger structures in an orderly fashion. According to their size, shape and range of the mediating forces, nanoscopic components assemble into larger structures [1]. Frequently the newly formed assembly,

possess a defined symmetry. Preferred geometries usually follow from a minimization of the energy of the system and topological restrictions of the assembled structure. Therefore, many formed assemblies remain in a metastable state. These principles of self-assembly are of paramount importance for the development of new technologies [2].

Directed self-assembly by means of electric or magnetic fields or by variation of pH, ionic concentration and temperature of the media could for instance, allow the fabrication of materials with unique properties [3]. If the interparticle interaction among subunits is not so strong, the assembled structure could show a pronounced mechanical flexibility or even display an inherent self-repair capacity upon mechanical deformation. This is usually the case in many biological systems where most of the processes are dominated by noncovalent interactions. This represents an advantage because many biological materials must evolve through different states or conformations to perform determined tasks. Organizing forces have not to be too strong because dynamic versatility is required. Here thermal motion interferes with stability. Self-assembly between molecules and in a wider sense self-assembly within single molecules like during protein folding accounts for a good example. Self-assembly of molecules is the major mechanism of work in the nanodimension. A remarkable example is the self-assembly of individual proteins into closed viral capsids. For many viruses, no external energy input is required during the assembly process.

1.2 From physics in the nanoscale to nanotechnology

The top down approach is the basis of our technology in the macroscale. It is limited toward the nanoscale. That is why self-assembly is of overwhelming importance for nanotechnology and needs to be properly understood and explored. Although there are general principles, every system may have specific aspects regarding self-assembly. Self-assembly depends on which forces are important for a specific system: for example, lipid membranes are excellent example of a self-

assembled nanosystem, where individual amphiphilic molecules assemble with a preferred orientation to avoid unfavorable interactions. In solution, the interaction among individual water molecules plays a central role. The arrangement of water molecules close to interfaces modifies the strength of the interactions, for example during the formation of closed lipid vesicles and protein folding.

Therefore a bottom-up approach methodology with single macromolecules interacting in the nanometer scale performing well defined tasks have changed the perspective of modern biologists to take biophysical parameters into account. For example the active transport of molecules within the cell or in the case when nucleic acids adopt intertwined conformations or highly condensed toroidal shapes in order to fit in the cell nucleus or within the capsid of a virus.

The collective interaction of individual receptor molecules at the cell surface accounts for the stable adhesion of cells onto substrates or against other cells. Another remarkable example in biology of an assembled functional material is that of the cytoskeleton. Within a cell, the cytoskeleton confers structural support through a network of actin filaments and microtubules resulting from the assembly of thousands of proteins working simultaneously. In some cells displaying filopodia, the interaction of these individual elements is transduced into mechanical movement.

Therefore, the detailed characterization of the mechanical properties and binding mechanism of individual cellular elements like proteins and nucleic acids will contribute directly to establish a bridge between structure and function in biological systems [4].

The assembly of oppositely charged polymers into multilayers by subsequent deposition is driven by electrostatic attraction and entropy increase due release of counterions. The mechanical, swelling, and hydrophobic properties of the resulting film can be tuned by the appropriate selection of the polyelectrolytes. Thus the chemistry of the layer at the surface is also known. These assembled multilayers offer a plethora of possibilities for future applications because multiple

functionalities can be tailored at their surface. For example the fabrication of biosensors is possible by the attachment of specific ligand molecules onto patterned multilayered surfaces. The coating process of a multilayer with a fluid lipid bilayer with free mobile inserted proteins could lead to the formation of a biocompatible interface.

Grafting polyelectrolytes to surfaces is another possibility. While the freely mobile side of the chain will extend in solution, electrostatic self-repulsion and steric effects arises when the space between the grafting points is reduced. This will make the chains to attain a stretched state. This new kind of assembly or polyelectrolyte brush shows novel interesting features. For example, the brush layer can be highly responsive to changes in the pH or ionic strength of the media. The hydrophobicity of the coated surface can be modified according to the type of polyelectrolyte used or the grafting density at the surface. Combination of polyelectrolytes with opposite pH or ionic strength sensitivities could be used for the fabrication of smart materials. With polyelectrolyte brushes is possible to fabricate nanoactuators based on mechanochemistry which could be regarded as first steps in the development of nanomachines.

Viruses represent another formidable example of a highly ordered nanostructured material. The assembly of the proteins composing the coat is driven by the specificity of protein-protein interactions among the subunits and their precise topological arrangement. Revealing the mechanical properties of this protein shells will increase our understanding of hierarchically designed materials by nature. By deletion of certain genes, the design of viral capsids with novel architectures with a differently modified amino acid composition would allow to use them as platforms for posterior chemical modification. The use of viruses in nanotechnological applications has considerably increased within the last decade, mostly due their biological relevance and flexibility to control their assembly [5]. To their capacity to be used as nanocarriers for material transportation, empty viral capsids or virus-like particles (VLPs) have acquired central attention in the scientific community for

their potential application as delivery vehicles for therapeutic molecules. These protein cages can be used as nanoreactors for chemical reactions as well.

The field of life sciences and medicine will be enormously benefited from advances achieved by nanotechnology. Living organisms, originally described by biologists in macroscopic terms, are now being investigated at the level of their most fundamental building blocks. Before structural characterization of organs, tissues and cell differentiation in the micrometer range used to play a central role in biological research. Nowadays, the link between single molecule protein structure and function has narrowed down and hence the origins of many old known diseases have started to be revealed. Furthermore the realization of highly specialized nanomachines to perform specific tasks, will aid to fight complicated diseases like cancer and genetic disorders so far unmanageable by conventional medical treatments [6].

To confront the mentioned challenges, nanoscience has developed and refined new experimental tools within the last three decades. Interrogation of single molecules at the nanoscale requires the application of ultrasensitive techniques able to measure forces in the range of typical bio molecular processes. Techniques like the Optical Tweezers, Magnetic Tweezers, Atomic Force Microscopy (AFM), the Bio membrane Force Probe technique, the Flow Chamber Assay and the Micropipette Aspiration Technique to mention the most outstanding examples [7-11].

These techniques allow the measurement of the minute intra and intermolecular forces governing most biological processes, e.g. hydrogen bonding, Van der Waals forces, hydrophobic interactions and electrostatic forces with picoNewton resolution.

Additionally to force measurement, manipulation of elements at the nanoscale like single atoms, molecular chains and Nano aggregates is expected to open new avenues in the fabrication of self-replicative molecular machines [12, 13].

1.3 Aims and Objectives

The work presented here has a multidisciplinary character, having as a common factor the characterization of self-assembled nanostructures through force spectroscopy. Exploring AFM as a tool for characterizing self-assembly and interaction forces in soft matter nanostructures, three different Bio and nonbiological systems where investigated, all of them share the common characteristic of being soft matter molecular structures at the nanoscale. The studied systems in question are: a) Polyelectrolyte – lipid nanocomposites. Single polyelectrolyte adsorption-desorption from supported lipid bilayers, b) Polyelectrolyte brushes and c) Virus-Like particles (VLPs). The scientific interest and industrial applications for each of these different nanostructures is broad, and their potential uses in the near future ranges from smart nanocontainers for drug and gene delivery, surface platforms for molecular recognition to the development of new nanodevices with ultrasensitive external stimuli responsiveness. These nano-structures are constructed following assembly of smaller subunits and belong to representative examples of soft matter in modern nanotechnology.

The stability, behavior, properties and long term durability of these self-organized structures depends strongly on the environmental conditions to which they are exposed since their building mechanism is a balance between attractive noncovalent interactions and momentum transmitted collisions due Brownian motion of the solvent molecules. For example a set of long chain molecules firmly attached to one end to a surface will alter their conformation as the space between them is reduced or the environmental conditions are modified (i.e. ionic strength, pH or temperature). For a highly packed condition, this fuzzy surface known as a polyelectrolyte brush will then behave as a responsive material with tunable responsiveness.

Thus the objective in the present case was to investigate the change in morphology and the mechanical response of a polyelectrolyte brush to external forces by application of AFM nanoindentations under different ionic strength

conditions. The degree of penetration of the AFM tip through the brush will provide insights into the forces exerted by the brush against the tip. Compressions on the brush should aid to characterize its changes in compressibility for different salt concentrations.

For the second chosen system, the interaction between two assembled interfaces was investigated at the single molecular level. A multilayered film formed by the consecutive assembly of oppositely charged polyelectrolytes and subsequently coated with a lipid membrane represents a fascinating soft composite material resembling more than a few structural components emerging in living organisms. The fluid bilayer, thus provide a biocompatible interface where additional functionalities can further be integrated (fusion peptides for instance). The smooth polymer cushion confers not only structural flexibility but also adaptability of the chosen substrate properties to be coated. This type of interface could be useful in the development of novel molecular biosensors with single molecule recognition capacities or in the fabrication of assays against pathogenic agents. The aim of this project was to study the molecular binding mechanism between the last polyelectrolyte layer and the lipid head group of the lower lipid leaflet. Understanding this adsorption mechanism between both interfaces, should likewise contribute to improve the fabrication of lipid coated polymeric nano/micro capsules with targeting properties. For example this could be critical in the field of nonviral gene therapy, where the improvement in the design of condensates of nucleic acids and other polymers with lipids (lipoplexes) are of main interest for its posterior use as delivery vectors.

Finally, viral capsids were investigated. These naturally occurring assembled nanocontainers within living organisms stand for a remarkable example of nature's morphological designs. These structures self-assemble from a small number of different proteins occurring in identical copies. The capsid as a self-assembled structure carries multiple functions: compaction of the genome, protection against external chemical threats, target recognition, structural support and finally facilitating the release of the genome into the host cell. It is highly interesting how

these different functions are organized within the capsid which consists, for example, in the case of the norovirus of 180 identical copies of one single protein.

Therefore, the mechanical stability and elastic properties of virus-like particles of Rubella and Norovirus were investigated by external application of loading forces with an AFM tip. The measurements were performed under conditions relevant for the virus infection mechanism. The applied compressions on these protein shells at pH values mimicking the virus life cycle will aid to learn about possible internal transitions among proteins which may be important for switching between the various functions of the capsid. The choice of two unrelated viral systems with different entry pathways into the cell and with different morphological architectures is expected to reveal crucial information about the stability and mechanical resistance to deformation of these empty membrane-coated and bare viral capsids. This last might provide clues on the stage of particle disassembly and cargo release during the final step of the infection process.

2. Polyelectrolytes and Lipids as building elements for nanotechnology

2.1 Introduction

Importance of polyelectrolytes. The interaction of polymers at interfaces plays a central role in diverse fields of science and is fundamental for technological applications. Sterical stabilization of colloidal solutions by tethered polymer chains has been one of the earliest applications of polymers in industrial processes, where coagulation and aggregation of the solute is an undesired effect. The adsorption of polyelectrolytes (particular case of polymers with ionizable groups) on the other hand, offers a practical approach to change the charge of a surface, or allows tuning the wetting characteristics of a substrate by increasing or reducing its hydrophobicity. The conformational sensitivity of polyelectrolytes to environmental conditions like pH, temperature or ionic strength makes them perfect building

blocks for the design of smart responsive materials. Polyelectrolyte molecules are further interesting because their chemical sequence will thus determine intramolecular interactions within the polyelectrolyte itself and intermolecular interactions with surrounding molecules. This defines the final configuration state of the molecule for a particular environmental condition. For the case of the mutual interaction of a group of polyelectrolytes in solution, electrostatic forces become long range facilitating synergetics in polyelectrolyte assemblies at the level of single chains and the whole assembly. The nonlinear optical properties presented by some polymer coatings have also been investigated [14], as well as the reversible photo-mechanical transition that single azobenzene molecules experience when irradiated with the right light frequency [15]. This has resulted in the design and characterization of highly efficient light-powered molecular machines and has provided new insights into future nanotechnological applications.

Biopolymers are polyelectrolytes. There is a plethora of polymers being used by living organisms for structural, recognition, chemical and functional purposes. For instance three of the most relevant groups of biomacromolecules are proteins, carbohydrates and nucleic acids. Proteins are polymers of differently concatenated amino acids units. Among them 5 out of the 20 canonic amino acids carry extra charged groups apart from the carboxyl and primary amino group, Lysine, arginine, histidine, asparaginic and glutaminic acid. Their three dimensional configuration is fully determined by its amino acid sequence as well as its surrounding media and temperature which has a direct impact on the intramolecular interactions taking place within the protein. Electrostatic and dispersion forces, hydrophobic effects, disulfide bridges and hydrogen bonds are usually responsible for the final stable arrangement of protein subunits into their native conformation. Proteins may adopt more than one conformation during its function. Each such conformation represents a local minimum of free enthalpy. Examples of carbohydrate polyelectrolytes are, Chitosan, Chondroitine and Dermatan sulfate being present in connective tissues. Charged carbohydrates can be also found at the cell surface

extending outwards, offering structural integrity to the cell wall or cellular recognition. Their structure is not restricted to be solely linear but could also be highly branched.

DNA is another good example of a linear biopolymer, being a polyelectrolyte. It carries a charge per monomer along its molecular backbone. Nucleic acids are important molecules due their information storage capacity and their ability to transfer this contained information through chemical reactions. A classic case is that of messenger RNA where the molecule encodes a fraction of a chemical sequence to generate a protein product. The magnitude of the intermolecular interactions between complementary strands has been investigated because specific recognition properties can be advantageous for the design of novel delivery vectors where nucleic acids are tightly bound to other polyelectrolytes, drug or lipid molecules. Of main concern is also the interaction of nucleic acids with other molecules of foreign origin for which it has been probed to have a direct impact on the development of hereditary genetic disorders or congenital malformation due genome damage at the molecular level during replication. The high affinity of unpaired RNA or DNA to specialized enzymes like polymerase transcriptase is another good example of information processing and represents a pivotal mechanism in the synthesis of nucleic acids. The complex functionality of the ribosome as an accurate reading code nanomachine allows the subsequent production of proteins. The intricate pathway followed by small interfering RNA molecules during gene silencing is, for instance, another remarkable example of finely regulated polyelectrolyte interactions taking place in the cell cytoplasm.

Nucleic acid - protein interactions are crucial inside the cell. In chromatin, which is the result of highly packed DNA by histones, the efficient condensation of the genetic material necessary during cell division is attained. Noncovalent interactions are required between DNA and the histones for posterior gene regulation at different stages of cell division.

Lipids. Lipid molecules possess an amphiphilic nature. Consequently a group of lipid molecules when immersed in water will gather exposing their hydrophilic parts to the solution and hiding their hydrophobic part into the bulk of the final assembled structure. Membranes are self-assembled structures that result from the collective self-arrangement of individual lipid molecules with a preferential orientation within a water. The emergence exhibited by lipid based structures like spherical vesicles, tubular fibers, planar bilayers and multilayers make lipid molecules essential elements as building blocks in the formation of organized molecular assemblies. Their fluidity and dynamical properties enhance their versatility as biomaterials in biotechnology. After assembly, individual lipid molecules conserve their own mobility across the plane due Van der Waals and electrostatic interactions but the newly assembled structure as a whole will display additional global properties depending on its size and geometry. Two main characteristic parameters of these lipid assemblies are the bending rigidity κ and the surface tension σ which define mechanical and elastic properties. Through hydrogen bonding, lipid molecules can form stable aggregates with certain polyelectrolytes making them excellent candidates as biocompatible materials for nucleic acid complexation [16].

Polyelectrolyte lipid interaction. The use of a multilayered polymeric composite as a scaffold for further coating affords an interesting and convenient strategy to obtain biocompatibility between surfaces of distinct nature. Depending on certain surface parameters like degree of ionization, roughness, available area, etc, a preferred polyelectrolyte molecule can be used to fulfill the requirements for proper adsorption. The topmost layer of polyelectrolyte interacting directly with additional lipid coverage will contribute importantly to determine the final behavior of the lipid coat. Coated spherical colloids in the previous described way, resembles therefore some dynamic features of a living cell. In such a way the main interest for studying the interaction between polyelectrolyte and lipid bilayers is to use them as model systems that mimic biological behavior, and on the other hand to produce biocompatible interfaces for molecular recognition.

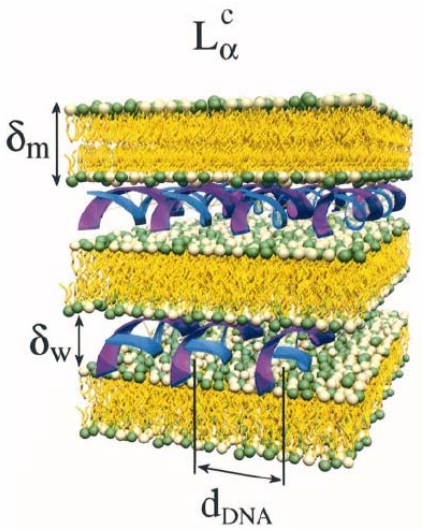

Figure 2.1 Lamellar phases formed by complexation between DNA molecules and lipid bilayers. Image taken from reference [16].

Delivery Lipoplex. Complexation of polyelectrolytes with lipids is currently a very active field of research since transfection of nucleic acids into cells promises to fight genetic disorders which remain intractable [17, 18]. Their application to specific tumor tissues has gained increasing interest as novel therapeutic nanoparticles with reduced toxicity and increasing targeting capacities are currently being developed [19]. However most of the aggregation or condensation properties of such particulate complexes are not entirely understood and proper characterization is needed before practical application (see figure 2.1).

2.2 Supported lipid membranes

Three principal methods can be used to form a supported lipid membrane. One is by transference of a floating monolayer to a particular substrate with the Langmuir-Blodgett technique. Another is when the substrate is exposed to a solution of oppositely charged lipid vesicles. In the latter process, attachment and rupture of the vesicles onto the substrate will proceed if the attractive interaction between

them is strong enough. The rupture of the vesicles promoted by fusion onto the substrate will create patches of lipid until a continuous bilayer is formed. Finally, a solid substrate can be coated with a lipid layer by evaporation of a lipid solution at its surface. This can be carried out using highly volatile solvent solutions like chloroform.

The final main characteristics of the supported membrane concerning lateral mobility of the lipid, fluidity of the membrane as a whole and surface coverage, are determined by a variety of factors such as lipid composition, chemical structure and roughness of the substrate, temperature and buffer conditions [20-22].

Artificial planar lipid bilayers have important uses not only for biology and medicine, but also in the development of optoelectronic devices, semiconductors and in general in nanotechnology [23, 24]. The membrane itself can be studied as a model of the cell surface, where interesting functionalities can be integrated on its surface [25].

There is an advantage in using supported lipid membranes for the study of ligand-receptor interactions. They provide a natural environment for the immobilization of proteins, provide lipid mobility, proper orientation and prevent protein denaturation.

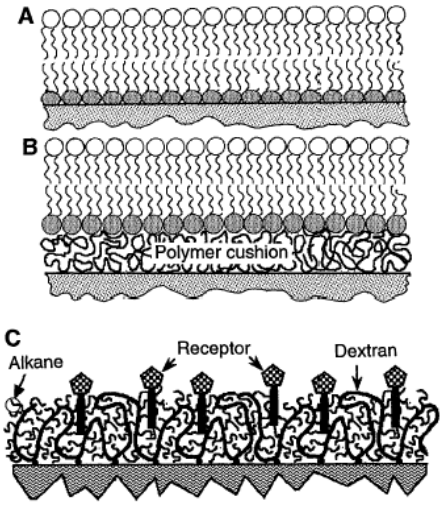

Figure 2.2 Solid supported lipid membranes. a) Covalently attached lipid membrane. b) Mobil polyelectrolyte supported lipid bilayer. c) Polymer cushion as support for monopolar receptors. The image was taken from reference [26].

As the liposome solution can be exposed to a variety of peptides, antibodies, hormone receptors and polymers, their potential as a platform for single molecule sensor technology has already started to be explored [27, 28] . As shown in figure 2.2, the bilayers will follow the surface texture of the underlying substrate as in the case of a polymer coated surface [29]. The bilayers maintain fluidity. They rest on an ultrathin (~2 nm) lubricating layer of water between the lower lipid leafleat and the substrate. Moreover, supported lipid bilayers can be intensively studied with experimental surface techniques like ellipsometry, atomic force microscopy, X-ray surface reflectivity, Fourier transform infrared spectrometry, etc [30, 31].

2.3 Polyelectrolyte multilayers

In the layer by layer approach of oppositely charged polyelectrolytes, the continuous assembly of subsequent nanofilms is possible [32-34]. Electrostatic interactions and gain of entropy as a result of release of counter ions are the main driving forces responsible for polymer adsorption. Polyelectrolyte multilayers (PEMs) can be used as a scaffold for posterior modification/deposition due their flexible chemistry of the last layer. Depending on the chemical groups of the topmost layer, the LBL technique allows to tailor surface functionalities with pending ligands according to well established conjugation protocols.

The growth of multilayered composites is not restricted to flat substrates or to the use of only linear polymers, but almost any surface displaying an opposite charge to that of the polymer in solution can be used. However, the final quality of the surface coverage strongly depends on the molecular structure of the polyelectrolyte as well as its response to the pH, ionic strength and temperature of the surrounding media. For example spherical colloids in the nano and micrometer range can be coated to investigate their mutual interaction through colloidal force microscopy [35].

With removable colloidal cores, the fabrication of polymeric capsules is possible [36]. The swelling properties of microcapsules in response to changes of the pH value for specific polyelectrolytes with certain degree of ionization have been exploited for the fabrication of drug and plasmid delivery systems [37, 38]. This sponge-like responsive effect facilitates the release of the cargo within endosomes after endocytosis [39]. The LBL technique allows also for incorporation of molecules of interest between the layers during the coating process as has been demonstrated for the case of DNA delivery [40]. Nanopatterning with the LBL technique can be combined with self-assembled monolayers of mercapto terminated alkyl chains on gold to fabricate nanopatterned surfaces [41].

2.4 Polyelectrolyte multilayer supported lipid membranes

The field of supported lipid membranes found in PEMs an attractive new platform to study the formation and stability of lipid bilayers, in comparison to other solid substrates [42, 43]. Polyelectrolyte multilayers covered by fluid lipid membranes serve as suitable model system for the study of cellular structures, since the polymeric scaffold offer a mechanical resistance resembling that of the Cytoskeleton. Moreover, micro sized colloidal particles coated with PEMs whose core can be optionally removed are subsequently covered with lipid bilayers after incubation with liposome solutions (see figure 2.3) [44-46]. These lipid coated colloids or capsules with biocompatible surfaces have recently attracted attention as they could potentially be used as cellular devices for delivery [47, 48]. Furthermore the lipid coated surface provides a platform for posterior integration of protruding peptides or other proteins of interest to identify binding interactions [26, 49, 50].

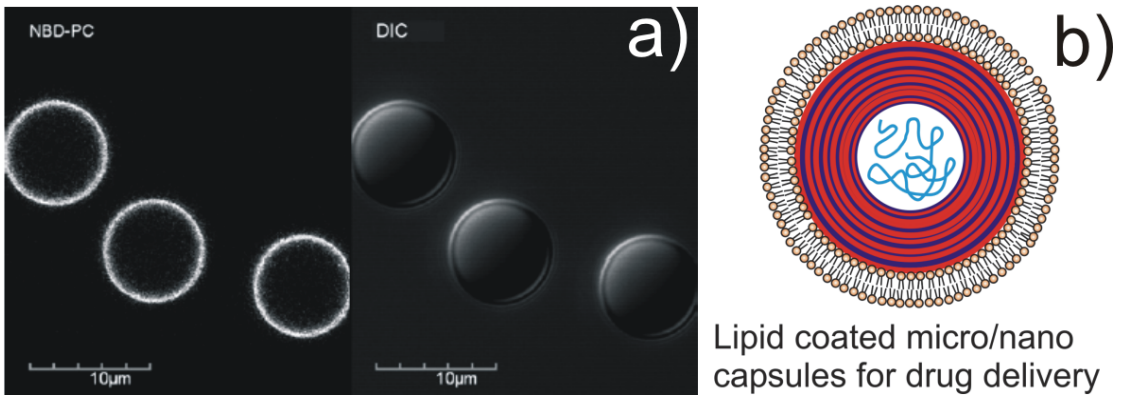

Figure 2.3 Polyelectrolyte supported lipid bilayers using the LBL technique. a) Fluorescence microscopy image of lipid coated Silica colloids. Image taken from reference [44]. b) Schematic representation of ideally coated microcarrier for drug delivery.

Either used as platforms for lipid adsorption or anchored thorough lipid membranes, the binding interaction between polyelectrolytes and lipid molecules plays a determinant role to account for the stability, softness and binding capacity of the system in question [51].

Although the fabrication and use of lipid coated surfaces has been successfully applied, the characterization of the coating quality and the molecular driving forces enhancing bilayer formation, have just started to be revealed [52]. The control and prediction of the final state of the lipid coat is not a trivial task, since the attachment, rupture and spreading of lipids on the last layer strongly depends on the binding interactions at the interface between the topmost polyelectrolyte layer and the lipid mixture (see figure 2.4).

An extensive study by different experimental techniques on polyelectrolyte supported membranes of Phosphatidylserine and Phosphatidylcholine onto Polyallylamine hydrochloride coated surfaces have pointed out that hydrogen bonding seems likely to be the driving binding mechanism between the lower lipid leaflet and the top polyelectrolyte layer during membrane formation [53].

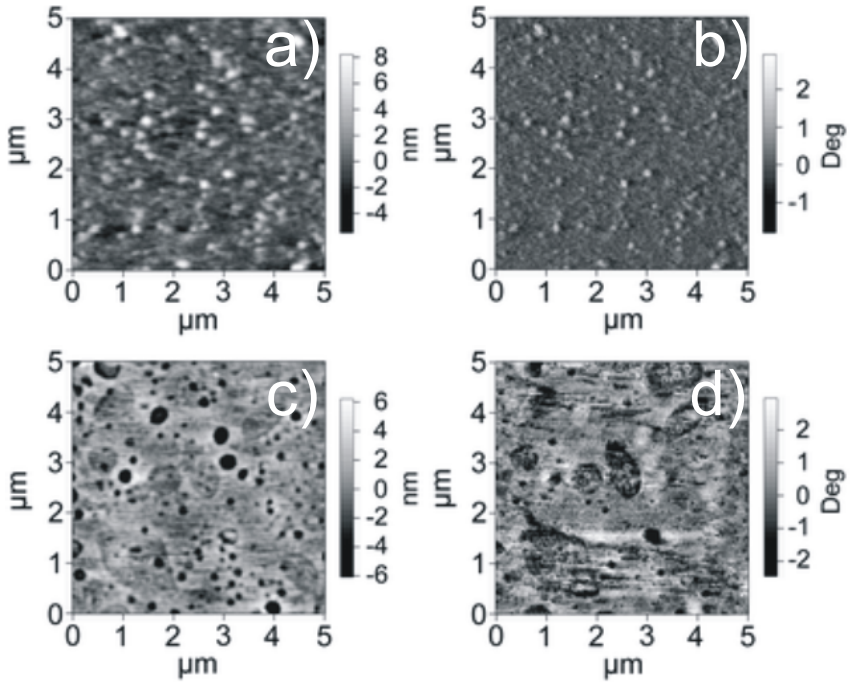

Figure 2.4 Atomic force microscopy images of polyelectrolyte supported lipid layers. A buildup of 9 layers of Polystyrenesulfonate/PolyDADMAC with PolyeDADMAC as topmost layer is made with the LBL technique. a) and b) shows height and phase images in tapping mode of the topmost PolyDADMAC layer. c) and d) same sample after incubation with a liposome solution of POPSPOPC 1:1 in NaCl. A remarkable change in the surface topography can be observed where a lipid multilayer appears to generate a sponge-like structure with overlapped layers and pores. Image taken from reference [53].

For the last reasons, a more detailed analysis on the interaction range and binding forces at the single molecule level could provide a more complete picture on the molecular binding mechanism formed between the polyelectrolyte subunits and the lipid head group. Single molecule experiments could importantly contribute to identify the binding sites between the lipid headgroups and the chemistry along the polyelectrolyte chain.

2.5 Polyelectrolyte brushes

Polyelectrolyte brushes are systems where one end of the polyelectrolyte chains is anchored to a surface while the rest of the chains are free.

The configuration of the chain will be determined by the environmental conditions of the media (ionic strength, pH, temperature, etc) together with the intrinsic properties of the polymer chain (charge, monomer chemistry, length). The chain can adopt a mushroom-like structure protruding normal to the surface for low grafting densities (see figure 2.5). These end-grafted polymers occur also in biological interfaces like in some virus capsids and bacteria. A nice example represents polysaccharide chains protruding from surfaces of the cell. If the surface gets crowded with anchored polymers up to a point where the volume occupied by the polymers starts to overlap, then the grafted polymers will be forced to stretch upwards to minimize their volume of interaction. A more strict definition of a polyelectrolyte brush has been proposed by Brittain et al. [54]. Therefore a *polyelectrolyte brush* is a monolayer of end-tethered polymer chains with a brush height h which is larger than the end-to-end distance $\langle r^2 \rangle^{1/2}$ of the same individual unattached chains when dissolved in the same solvent conditions.

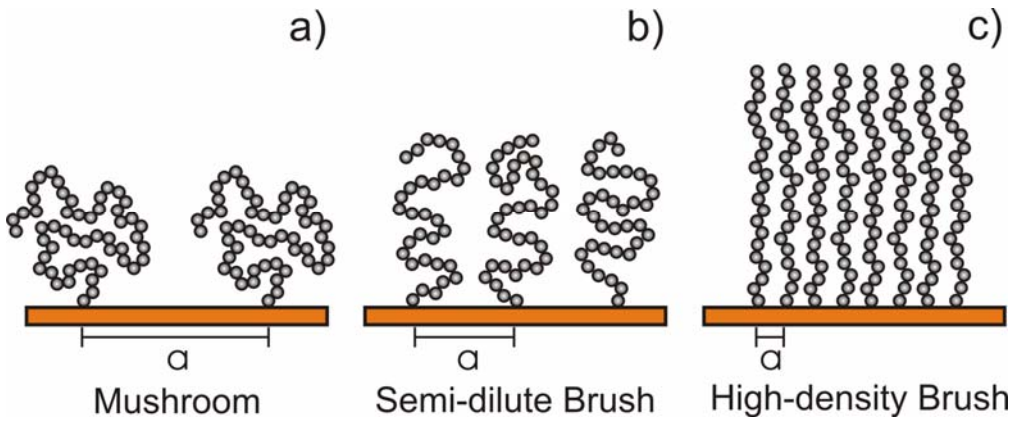

Figure 2.5 2D representation of end-grafted polymer onto a flat substrate at increasing surface densities.

Hence the final height reached by the stretched polymer chains is the result of the excluded volume effect among them counterbalanced by the elastic energy of the stretched polymer coils. The stretching of the polyelectrolytes is equivalent to a loss of conformational entropy. Polyelectrolyte brushes can be grown onto flat, cylindrical, spherical and even single molecular surfaces. Furthermore the substrate used can be a solid (like a glass plate, silicon wafer or gold coated surface) or a liquid (like a fluid lipid membrane), and the grafting is normally achieved through covalent bonds, electrostatic interactions, van der Waals interactions or hydrogen bonding.

In polyelectrolyte brushes (PE), the polymer backbone carries ionizable groups [55]. A striking difference with neutral brushes is that PE brushes possess a pronounced sensibility to external variations of ionic strength and in certain occasions also to pH. In good solvent conditions a PE brush swells in response to the electrostatic interactions among neighboring polymer chains within the brush and self-repulsive interactions along single chain subunits. When exposed to good solvent conditions and low ionic strength conditions, the PE brush also suffers a strong expansion, due a change in osmotic pressure. This difference in osmotic pressure arises when the counter ions present in the bulk solution are drawn into the brush to establish neutrality. When salt is introduced in a PE brush, the charge along the polymer chains becomes effectively screened. This consequently leads to a collapse of the brush into a thinner and more compacted structure. Collapse of the brush is accompanied by water release from its inside.

The PE brush is thus a material whose responsiveness directly depends on changes of macromolecular conformations when external stimuli are applied [56]. Besides ionic strength, external stimuli like changes in temperature, pH, surfactants and irradiation with light have been used to trigger molecular responses in PE brushes in order to measure variations in basic parameters of PE brushes such as surface morphology, hardness, collapse or brush height, hydrophobicity, adhesion and refraction index [57, 58]. The wettability range of PE brushes of poly(potassium 3 - sulfopropyl methacrylate or PSPM) a polyanionic brush has

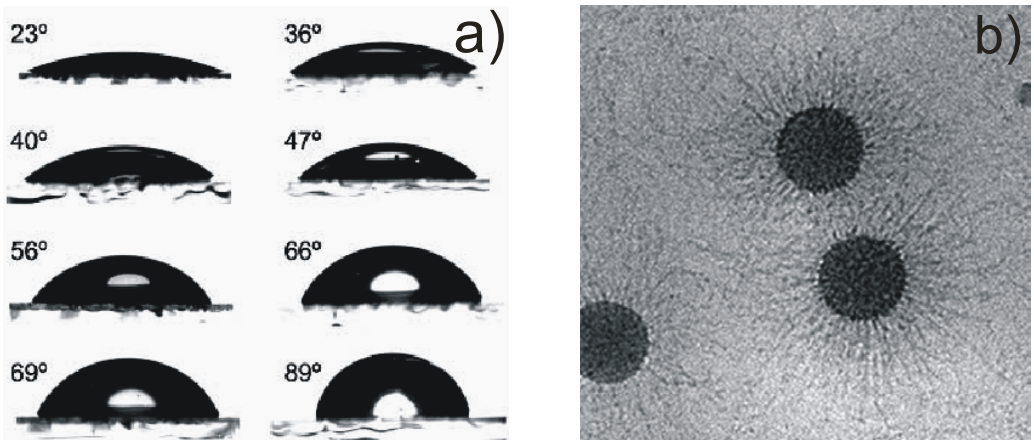

Figure 2.6 Change of properties of polyelectrolyte coated surfaces with brushes. a) Increase in the measured contact angle accounts for the gain in hydrophobicity by the surface. Image taken from reference [59]. b) Colloids displaying stability in solution due steric interactions through tethered chain molecules. Image taken from reference [60].

been studied by Moya et. al. by exchange of counter cations [59]. Cation exchange induced a drastic collapse of the brush which was followed with the quartz microbalance and through contact angle measurements it was shown that the water contact angle could be increased reversibly from 36° to 89° (See figure 2.6). This allowed tuning the surface from hydrophobic to hydrophilic.

Nanotechnological applications of Polyelectrolyte brushes. Although features and, especially the behavior of polyelectrolyte brushes is still extensively studied, controlled and understood, the practical use of these nanodevices has just started. For example stealth liposomes (spherical lipid vesicles with Polyethylene glycol molecules protruding from their surface) or other new particulate drug delivery systems are frequently equipped with a corona of light, pH or ionic strength sensitive polymers with a particular function. Also, many medical instruments are desired to maintain antiseptical properties since microbial contamination is a constant risk during a medical intervention [61]. A thin brush layer could reduce profoundly adhesion of such external parasites. Induced mechanotransduction from changes in chemical potential to mechanical force has been probed by Huck

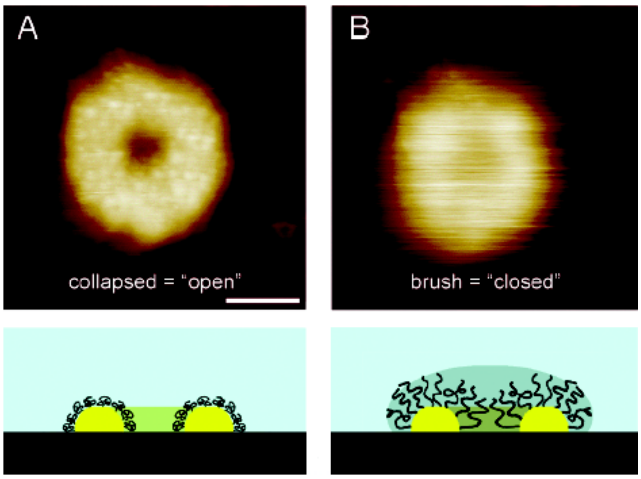

Figure 2.7 A brush nanogate. A polyelectrolyte brush patterned with a ring geometry rendering a pore with an open-close mechanism. Image taken from reference [62].

et. al. in brush coated gold microcantilevers [63]. In good solvent conditions brush swelling is accompanied by a measurable deflection of the cantilever, making the cantilever beam to behave as a nanoactuator. Another similar and promising application is the fabrication of diameter-variable pores that mimic some protein assemblies on the cell surface and which could be used as controllable nanoshutters (See figure 2.7) [62]. Further optimization and characterization is expected to speed up the practical use of these molecular arrangements in coming years.

3. Measuring forces at the nanoscale

In 1982 a new type of microscope was invented by G. Binnig and H. Rohrer, the Scanning Tunneling Microscope (STM) [64]. A major difference in the operating mode of the STM with other microscopy techniques is that no lenses or beams of light crossing the sample were required. Instead a voltage applied between a fine metallic tip and a conductive surface when approached at close separation, permitted the establishment of an electronic current between the gap. The origin of the flowing separation dependent current between the tip and the surface is based

on a quantum effect. The *quantum tunneling* effect created by the flowing current of electrons from the atoms on the tip towards the atoms on the sample through a vacuum gap, make by the first time possible to *"visualize"* individual atoms by observation of their electronic density clouds. Scanning the surface with this technique provided a tridimensional reconstruction of the surface topography with a high spatial resolution of a few Å laterally and 0.1 Å vertically [64]. A few years later, it was proved that the STM could be used to position single atoms by increasing the flowing current which strengthened the adhesive force between tip and atoms [65]. Manipulation of single atoms eventually led to the formation of interesting structures like "quantum corrals" where the pattern of the electron waves of the surface interfere with those of the imposed atoms forming the corral [66]. Although the power of the STM as a surface technique and as a nanomanipulation device was almost immediately recognized, this microscope presented an important drawback. It could only be used with conductive samples.

3.1 Atomic Force Microscope - a surface profiler and a force sensor

A consequence of these technological achievements with the STM, a decade later the Atomic Force Microscope (AFM) was invented by Binnig G. and F. Quate [67]. Contrary to its antecessor, the AFM could be used to explore the surface topography of nonconductive samples. The AFM uses an ultrasharp tip which is attached at the end of a flexible cantilever to explore the surface features of a sample. At very close separation distances between tip and sample, interaction forces will induce bending of the cantilever whose deflection is measured by a laser beam which hits the back of the cantilever and is then reflected to a 4 segmented position-sensitive photodiode. The sample is mounted onto a piezo-electric crystal which controls the movement of the sample in the x-y plane with subnanometer resolution. An externally applied voltage to an additional z-piezo is used to approach and retract the tip to the sample surface while a feedback circuit maintains the separation distance between tip and sample close to a constant

value. Whence, every raster line represents the surface profile for the tip-sample interaction. After the full scanned area is completed, the final set of collected profiles is used to reconstruct a three-dimensional representation of the sample surface.

Figure 3.1 shows the main components of an AFM unit and scanning electron microscopy images of the typical AFM tips and cantilevers.

Therefore, the mode of operation of an AFM is similar to the one followed by the blind man walking on the street guided only with a stick. Or in other words, the blind man perceives the world through the contact of the stick against the surrounding objects.

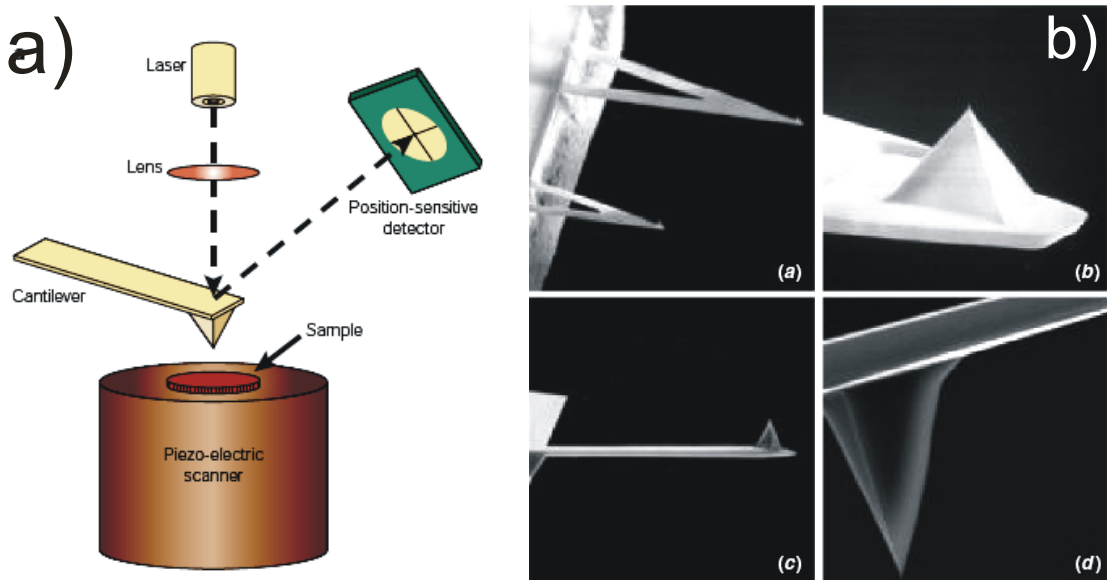

Figure 3.1 Main components of an Atomic Force Microscope. a) Schematic representation of the critical elements of an atomic force microscope. b) Micro fabricated Silicon nitride cantilevers and tips observed by scanning electron microscopy. Image taken from reference [68].

Normally this tip has its pyramidal or conical base attached at the end of a flexible beam or microcantilever followed by an acute apex at the lower extreme ending in a quasi-spherical shape of about 20 nm in diameter. Cantilever and tip are made of the same material with well characterized mechanical properties, usually silicon

nitride with Y = 270 - 290 GPa. A very soft cantilever with k = 0.01 N/m would provide a theoretical force resolution of 1.0 pN. However, during experiments, the resolution limit decreases because small forces (1.0 - 10 pN) are often overwhelmed by the thermal noise.

With stiffer cantilevers, forces up to 100 nN can be measured. Manipulation of nanoobjects with AFM is also possible. Manipulation of objects is possible by two different methods: a) Application of shear forces to induce mechanical disruption on the sample. With this method the dissection of cylindrical viruses has been reported [69]. Also, nanolithography has been produced onto soft films as the tip scratches the sample with a constant force [70]. b) Chemical functionalization of the AFM tip with specific molecules like long polymer chains or antibodies, allows the positioning and measurement of individual binding interactions.

The AFM utilizes the optical lever technique to measure deflections in the cantilever as the tip encounter obstacles on the surface. This light-lever yield a maximal sensitivity in the vertical direction when the cantilever length is small compared to its distance from the detector. This accounts for the magnification capacity of the technique. With the optical lever technique cantilever deflections in the order of 0.1 nm in the z direction are possible. Within the range of elastic deformations the deflection of the cantilever can be modeled as a spring obeying Hooke´s law F = kZ, with Z as the cantilever deflection. The applied force can thus be calculated once the spring constant of the cantilever has been independently determined. Calibration of the cantilever has been initially determined through the added mass method [71] and lately by the more commonly used thermal noise method [72]. However, resolution in the plane is dependent on the acuteness of the AFM tip. Larger or blunted tips will not easily penetrate deep within narrow edges among nanoscale objects as ultrasharp tips. This will reduce, but nonetheless, not avoid a convolution effect that leads to an overestimation of the width of the imaged objects and makes measurements of shape below the equator impossible.

Of major importance in AFM technology was that samples could be imaged in dry as well as under fluid conditions [73]. This remarkable faculty of the technique overcomes the unnatural, problematic and sometimes time consuming fixation methods mandatory for transmission electron microscopy (TEM) and scanning electron microscopy (SEM). Additionally, sample preparation in AFM is usually a mild procedure. Simple deposition of the sample onto a solid substrate is frequently enough for imaging. Preferred due their atomically flat external features, cleaved mica and roughly cleaned glass have shown to provide suitable platforms for the imaging with defects below 1 nm. In case of unfavorable electrostatic attachment between substrate and sample, the substrate can be further coated with a film of oppositely charged polymers or be functionalized to gain specific binding affinity to the chemical groups in the sample.

The advent of the AFM brought to biology a new powerful technique to investigate processes that could take place under close physiological conditions [74-78].

The basic operation modes in atomic force microscopy imaging are "*contact*" mode (CMAFM) and "*Tapping*" mode (TMAFM). In CMAFM the tip is pressed against the sample until certain predefined deflection value is attained. The feedback loop will maintain this constant deflection along the scan which is ultimately converted in force through the cantilever stiffness. By the contrary in TMAFM an integrated resonator will induce an oscillatory movement on the cantilever close to its resonance frequency. As a consequence, the tip is approached to the sample surface as it continues to oscillate. In this mode the tip taps the surface only periodically, and deformation due shear forces during scanning as well as contact time with the sample are thus reduced. The former mentioned advantages over CMAFM are evidently useful for the study of biological specimens, where most of their constituent elements are formed through noncovalent interactions, regarded as soft matter [79].

In general, three principal signals are displayed in an AFM image as the data is being recorded. A *height* image represents the measured error signal or the z-

voltage output scaled by the piezo sensitivity. The *deflection* shows the DC deflection of the signal from the cantilever (difference between upper and lower detector segments). And finally a *lateral* image which accounts for the twisting effect the cantilever suffers when displaced sideways from the its longitudinal axes (difference between right and left detector segments). On the other hand, for TMAFM the two main parameters to control are the amplitude and frequency of the oscillating cantilever. Besides the *height* signal, two other signals provide useful information about the sample. The *Amplitude* signal represents the AC amplitude of the cantilever deflection will interacting onto the sample. The *Phase* signal renders the phase lag between the free oscillating tip, to the closely approached tip onto the sample surface.

The AFM has thus become a versatile tool in biology, physics and material science laboratories where it has been applied to observe details and structural changes of biological membranes in their native state [80-82]. The group of Andreas Engel has successfully characterized the morphology of the purple membrane of *halobacterium salinarum* up to a lateral resolution between 1.1 and 1.5 nm to a vertical resolution of ~ 0.1 nm [83]. Likewise, the native extended conformation of individual polypeptide loops that connect the transmembrane α-helices E and F of Bacteriorhodopsin were identified in great detail.

Lipid bilayers formed onto solid supports show smooth textures on planar patches which can be studied within modest periods of time in presence of protein or drugs. The dynamics of lipid bilayers and their subsequent alterations with the antibiotic azithromycin has been investigated by the group of Yves F. Dufrêne in real-time [81]. Erosion and disappearance of the bilayers were observed after 60 minutes incubation with the antibiotic. Imaging the surface of living cells as originally demonstrated by F.M. Ohnesorge et al. showed the outstanding capacity of the AFM to visualize dynamic processes at the cell surface, as is the interaction with viruses [84]. Multilayered flat films [85, 86] and spherical shells made of polyelectrolytes have also been the focus of the AFM technique to understand their mechanism of assembly, as shown by Leporatti et al [87].

AFM has also been applied for the rapid identification of some viruses as reported by the group of A. McPherson where high resolution images allowed the clear observation of individual capsomers at the surface of the virus [88]. Finally, single molecules have been characterized when strong or weakly attached to surfaces. The topological, structural and functional properties of double stranded DNA have been intensively studied by AFM where the molecule can be manipulated to the point of single chain dissection by the AFM tip [89]. When weakly attached to the surface, the dynamics of enzymatic action can be studied [90]. The binding and action of enzymatic activity like endonuclease to plasmid DNA onto mica have been reported by D.P. Allison et al. [91].

Force sensor

The evolution of the atomic force microscope from an imaging technique into a force sensor device occurred simultaneously with its initial development. Imaging in AFM contact mode requires stable *engagement* between tip and sample, which in some cases is not trivial, because the intermediate interaction forces between tip and sample depend strongly on the properties of the sample and the environmental conditions. When this *engagement* between tip and sample is established, the attractive Van der Waals forces pulling the tip against the surface are counterbalanced by the Born repulsion that arises as the electron clouds overlap among atoms. It was then clear that the precise control of the cantilever deflection during compression of a soft sample would not only reveal material properties of the sample upon compression but also short (1-10 nm) and long range interaction forces (10-200 nm) above the sample as well.

However, in dry state, surface forces are hidden within the strong adhesion arising from the meniscus force of a frequently involved ultrathin water film (<100 nm) condensed above the sample surface. This is nonetheless solved by immersing the system under liquid conditions which is in fact advantageous, since plenty of systems of interest in colloidal science and biophysics take place under a fluid

environment. Force spectroscopy, where the AFM tip is approached and retracted vertically in a controlled fashion was therefore applied to a wealth of different situations where surface forces played a central role (see figure 3.2).

Thus the recorded force-separation curves describe the range and the strength of the interaction. In this way relevant molecular forces acting between interfaces in a variety of electrolytic solutions have been investigated. Original experiments have shown the measurement of forces between an AFM tip or a colloidal probe attached to a tipless cantilever and a particular substrate as they are monitored as a function of their separation distance [92, 93].

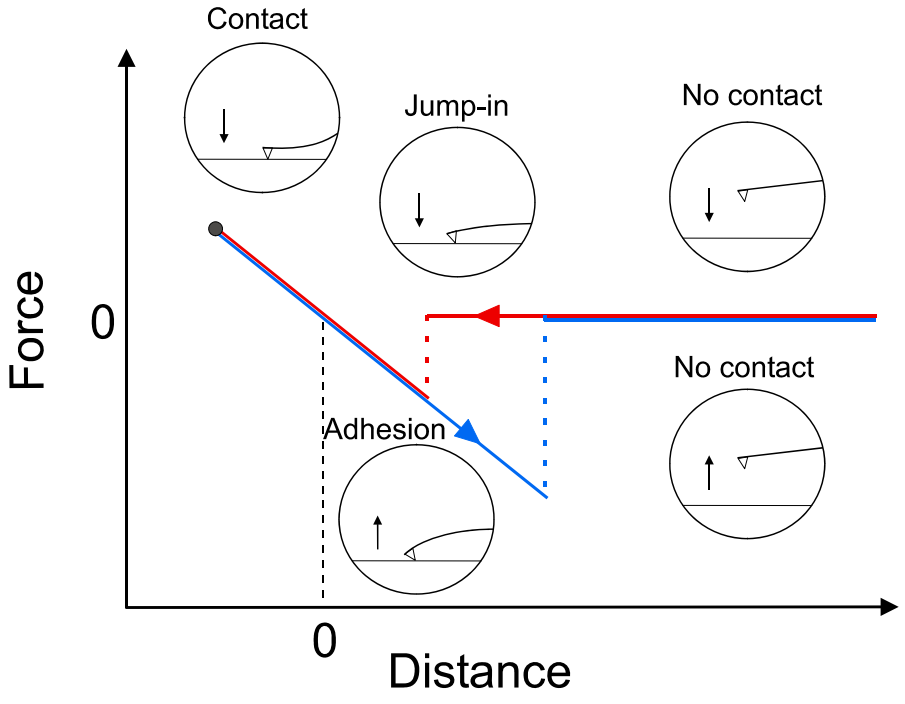

Figure 3.2. Schematic representation of principal stages in a Force-Distance curve. Red line represents *approach* against the surface while blue is retraction *from* the surface. A sudden jump-in to contact upon approach is depicted as well as an adhesion peak upon tip withdraws.

As first shown by Senden et al., electrical double layer forces have been exploited to image silicon nitride surfaces [94]. These experiments were pivotal for the further improvement of the microscope. In pioneering experiments conducted by

Hans-Jürgen Butt, repulsive forces between AFM tip and equally charged substrates in pure water showed a decaying exponential behavior within the range of the Debye length [95, 96]. These interaction forces depended on the salt concentration. This behavior was attributed to have an electrostatic origin. Nevertheless at much closer distances (~ 1nm) from the surface, VdW forces overcome the cantilever restoring force and the tip is suddenly pulled onto the sample usually represented by an attractive jump-in in the force curves. For higher ionic concentrations electrostatic forces are negligible (> 1M KCl, a λ_D~0.1 nm) and hydration forces of about 70 pN where measured.

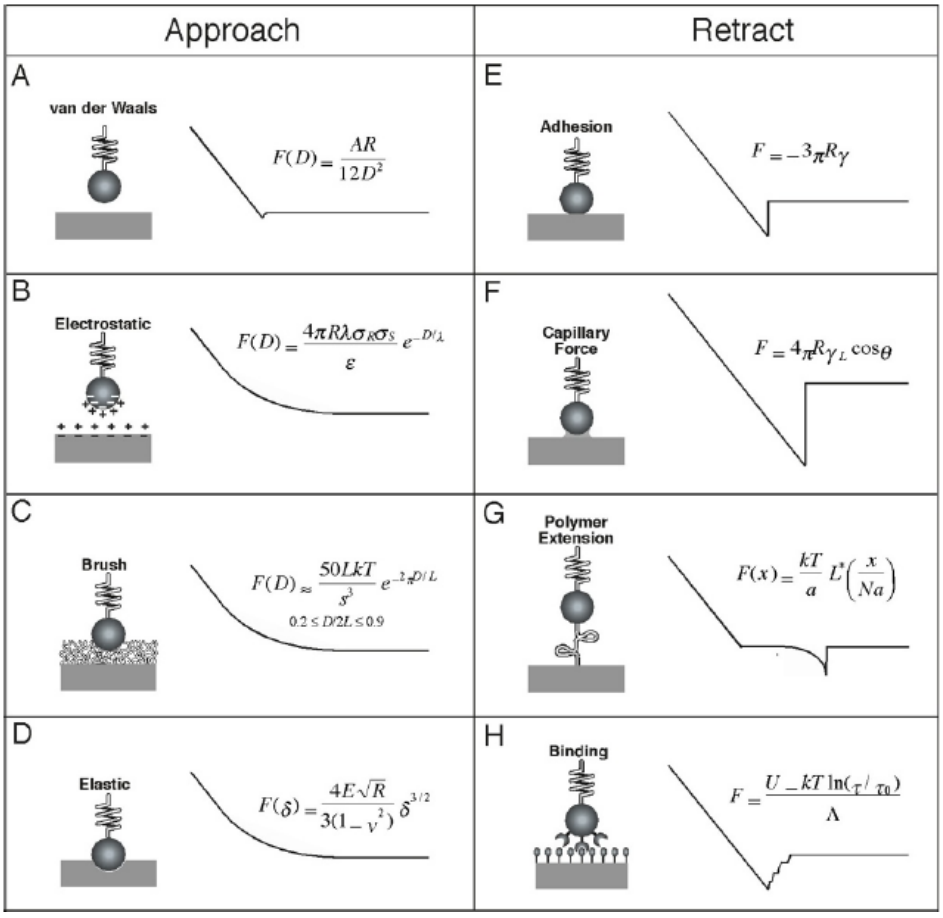

Figure 3.3 Examples of measurable surface forces with the AFM in force spectroscopy mode. Image taken from reference [97].

First experiments devoted to investigate the interaction forces between silicon nitride AFM tips and lipid coated surfaces in electrolyte solutions were reported by the group of Beveridge [98]. It was observed that a long range force dominated the interaction upon approach and it was concluded that the surface carried an intrinsic surface charge even for neutral lipid layers. Yet, the elusive quantum fluctuations induced by Casimir forces have been measured with this sensitive technique [99].

Measurements of minute forces like the ultimate breaking of single molecular bonds are possible with the AFM, where forces small within the range 20 – 100 pN are ordinary. For such measurements, it is required that the apex of the AFM tip as well as the opposing substrate be fully coated with the target molecules as shown in figure 3.3H. The use of very small forces during tip approach, permits the close approach between both target molecules to slightly contact each other to induce bond formation followed by withdraw of the AFM tip at a constant rate.

This fishing technique or chemical force microscopy, allows to measure the forces required to break single bonds and therefore to investigate the strength among different chemical species [100]. First measurements on the physical quantification of single covalent bonds and ligand-receptor interactions were reported by the group of Hermann Gaub [101-103]. A few years later, it became possible to firmly attach linear polymer chains to the AFM tip and to investigate their subsequent desorption from solid substrates. From these experiments, the unbinding force per segment from the substrate can be extracted and conclusions about the origin of the chemical binding groups could be drawn [104, 105]. With this approach the interrogation of pathogens like bacteria and viruses as well as single membrane proteins will be possible [106]. An excellent report covering applications and interpretation of data of with the AFM has been given by Butt and Capella [107].

3.1.2 Single-molecule force spectroscopy to test polyelectrolyte desorption from interfaces

Atomic force microscopy has become a major technique to measure binding forces between single molecules. Single molecule force spectroscopy (SMFS) is based on the appropriate surface modification of the AFM tip with a molecule of interest to be tested against a complementary molecule usually located at the sample surface. The modified tip is then approached and retracted at a constant rate to obtain force – separation curves. Information about the range and magnitude of the single binding/unbinding interactions can be extracted.

The power of this approach relies mainly in three points: First, the distance between the two samples with unknown interaction is varied with high accuracy, by monitoring the force between them with picoNewton (10^{-12} N) resolution during the approaching- withdraw cycles. Second, a variety of chemical cross linking methods allows exploring an increasing amount of molecular species. And third, the environmental conditions can be changed according to the desired experimental requirements. This is particularly useful in the biological sciences where molecules perform different functions while are exposed to a wealth of different buffers and electrolytic solutions.

Through single molecule experiments of long polyelectrolyte chains covalently attached to the AFM tip it is possible to explore intramolecular interactions and intermolecular interactions as well.

Desorption of single polyelectrolyte chains from solid substrates renders a typical step-like pattern or Plateau upon retraction, as shown in figure 3.4a). For this case, it has been considered that polyelectrolyte chain is peeled-off the substrate segment by segment at a rate that is much slower that the kinetic rate of bond dissociation-reassociation between the chain and the substrate [108-115]. This desorption process is regarded to take place in thermal equilibrium, to be reversible and independent of the loading rate. A Gaussian distribution is expected to be obtained in the histogram for force desorption.

On the other hand, intramolecular interactions are observed when a single chain is stretched out from its equilibrium conformation, for instance, by fixing the other pending side of the chain to the substrate and increasing their separation by retraction of the tip.

This leads to a nonlinear force response as the one shown for the case of PAH in figure 3.4b). Stretching the polyelectrolyte close to its contour length, results in a maximal extension from bond angles and covalent bonds briefly before the chain suddenly desorbs. During extension the decrease of entropy due polyelectrolyte stretching determines the magnitude of the restoring force.

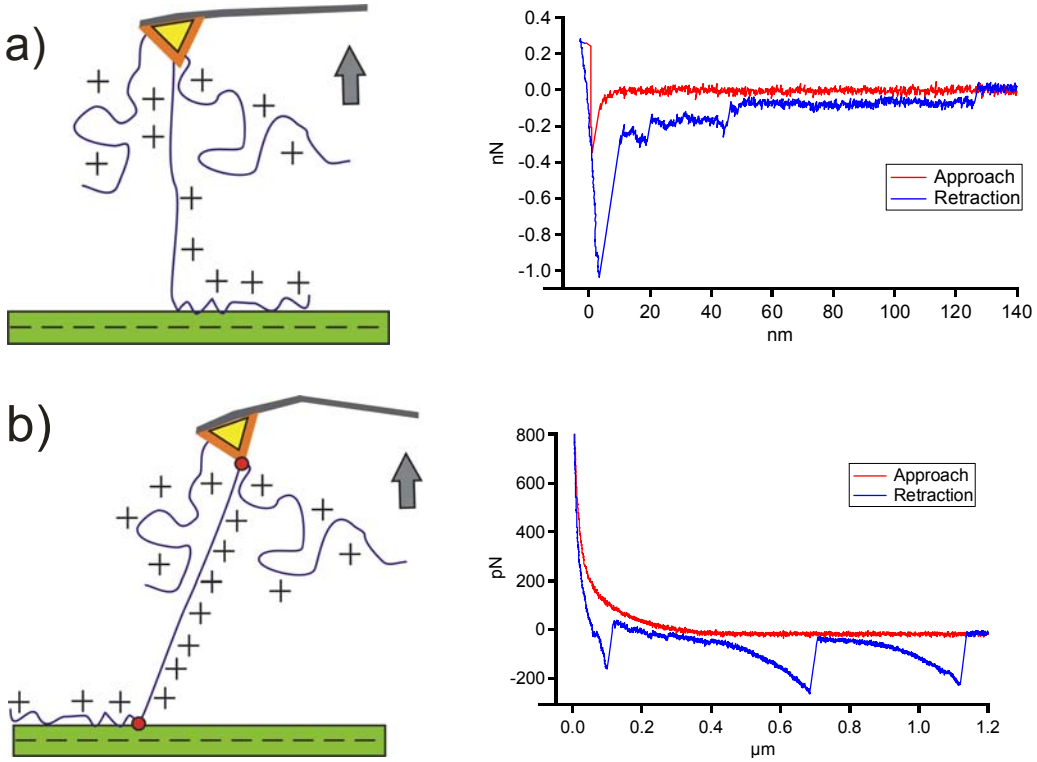

Figure 3.4. Representative approach (red) and retraction (blue) Force-Separation curves for the case of Poly(allyl amine) hydrochloride and bare glass surface. a) Polyelectrolyte desorption. Four steps represent that four single molecules have been desorbed. b) Polyelectrolyte stretching. Inverted saw tooth patterns show clearly how three single molecules were stretched.

The conformational transition that a charged molecule suffers from a possible initial coiled state to a final extended configuration is also influenced by the properties of the media (pH, ionic strength, and temperature).

In this way important physical parameters of the molecule can be estimated like its persistence length l_p and its bending rigidity κ, by making use of approximated models as the Freely jointed chain and the Worm like chain model. The study of the tensile strength of single polyelectrolytes and in general of polymers could lead to the development of advanced materials with reinforced mechanical properties.

Attachment of molecules to the AFM tips has been successfully achieved by mainly two methods. The first is based on amination by silanization applied directly to the silicon nitride AFM tip. The second method and the one which has shown to render effective long term measurements without loss of the testing molecule, is based on coupling chemistry of thiols [116]. In this approach a self-assembled monolayer (SAM) of alkanethiol molecules is formed onto a gold coated surface, which can be for example a gold coated AFM tip. Once the SAM is formed, the test molecule (polymer, antibody, etc) with a pending carboxyl groups or amine group are bound through peptide bonds to the AFM coated tip.

3.2 AFM Nanoindentation: A new approach to test mechanical properties of soft materials

If the AFM tip is used as an indenter to induce deformations onto the sample surface with a defined loading force, elastic and material properties of the sample can be extracted. Analysis of the induced deformation ξ through force-separation curves can thus yield important information about basic intrinsic parameters of homogeneous or composite materials. By applying equations taken from continuum mechanics or thermodynamics it is possible to measure material properties like its Young Modulus (Y) or bending rigidity (κ). This technique has been successfully applied to a variety of tissues and biomaterials, for instance

cartilage, bone, polymeric multilayers and continuous gelatin films, collagen, mollusk shells, ionic crystals and single cells [117-127]. Learning from these naturally designed structures could provide some clues for the development of modern hierarchically constructed materials in the nano, micro or even macro scale. Loading and unloading the tip in a controlled manner could also reveal if the sample displays elastic or plastic mechanical features. Relaxation times of force responsive materials stimulated by differently applied loading-unloading rates could be deduced.

Nanoindentation has become a very popular tool to test hard, soft and force reactive samples for which little is known, because of the earlier impediment of positioning with subnanometer accuracy. The AFM allows observing the sample topography before an indentation is performed onto a predefined position. This is particularly useful when probing highly symmetric assembled nanomaterials where their geometry and the specific point of applied force play a central role to describe the force response. Moreover, individual nanometer scale entities can be compressed with the tip to reveal how soft, elastic or brittle they could be. Supported lipid bilayers, carbon nanotubes, enzymes with globular structure, protein microtubules, lipid vesicles and wild type or empty viruses are a few examples of possible targets for AFM nanoindentation.

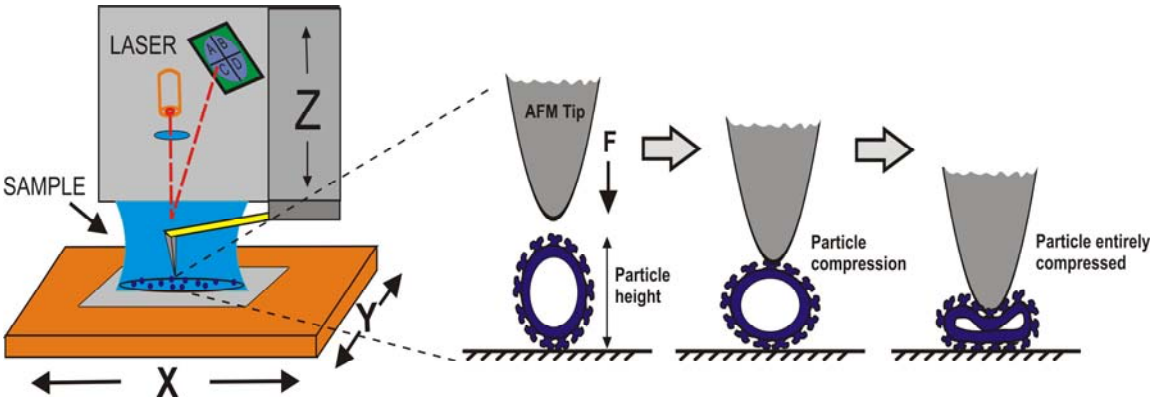

Figure 3.5 Schematic representation of the experimental setup to study mechanical properties of viruses with AFM nanoindentations.

A schematic representation of a typical Nanoindentation experiment is shown in figure 3.5. De Pablo et al. reported the elastic behavior of in vitro assembled hollow microtubules when locally compressed with radial nanoindentations [128, 129]. It was shown that loading forces of about 400 pN were required to induce a crack onto the upper wall of the protein tube which leads to nonlinear response in the force. A Young's modulus of ~ 0.8 GPa was obtained. Through the visualization and further compression of individual liposomes with a radius < 200 nm, N. Delorme and A. Fery obtained a Young's modulus of E = 110±15 MPa [130]. Y. Dufrêne used contact mechanics to characterize the elastic deformation of lipid bilayers, for which a Young modulus of Y = 2.1 x 10^8 N/m^{-2} was estimated [131].

Nanoindentation studies of viruses and viral capsids. An advantage on the study of the mechanical properties of viruses is that from a coarse point of view where the viral particle whole dimension contributes more significantly than its local molecular details, (like space between surface proteins) viruses adopt certain restricted and well defined geometries, for instance sphere-like, rod-like and icosahedral-like morphologies. This facilitates the application of available theories, for example the deflection of thin shells to describe empty viral shells [132].

Furthermore in this particular case, the simplicity of the AFM experimental set up allows to treat the system Cantilever + Capsid as two springs in series from which the effective response is obtained in a force measurement (see section 6.3).

Interesting questions can be addressed, such as on capsid elasticity and on stability and on how the capsid responds to repetitive deformations. The influence of the core on the mechanical properties is another important question. From the point of view of Virology it is interesting to know whether the material properties change during maturation or during the virus life cycle.

First experiments were conducted by Ivanovska et al. on empty φ29 bacteriophage proheads. These are 54 x 42 nm nanocontainers [133]. It was noticed that the shell could withstand and provide a linear response for deformations up to 30% of the total capsid height. Above ~ 2.8 nN the capsid response deviated from linearity and

after repetitive indentations, breakage of the shell was observed. The Cowpea chlorotic mottle virus (CCMV) is a round plant virus of about 30 nm in diameter. Its empty capsid was also investigated [134]. In this study it was shown that both full and empty capsids were also highly elastic with a spring constant of 0.20 ± 0.02 and 0.15 ± 0.01N/m respectively. A Young modulus of 140 MPa was obtained for the empty shell. It was observed that a single point mutation in the amino acid sequence of the capsid was enough to increase the capsid stiffness. While the hardness of phage φ29 could be compared to that of hard plastics, the CCMV capsid strength belong to that of soft-like plastic materials.

Even higher stiffness values have been reported for the minute virus of mice (MVM) where fine AFM imaging permitted to discern among different capsid symmetries before compression [135, 136]. For this small empty capsid (~ 25 nm in diameter) values of about 0.5 N/m were obtained. Is worth at this point to mention that the ratio between capsid thickness to diameter is expected to have a considerable impact on the force response. For the wild type virus a DNA mediated reinforcement within the capsid was clearly obtained. The ultimate internal pressures that these stuffed capsids are capable to withstand, play an important role concerning the infective functional properties of the capsid as well as its stability. Internal pressures inside viral capsids have been investigated through different approaches to account for the influence of the encased genome together with the capsid strength.

The osmotic pressure exerted by the confined nucleic acid against the internal capsid walls has been estimated for λ-phage, where it was observed that wild type capsids were twice stronger and more stable than those which contained shorter genome segments [137]. For λ-phage, a Young modulus of E = 1.0 GPa was obtained.

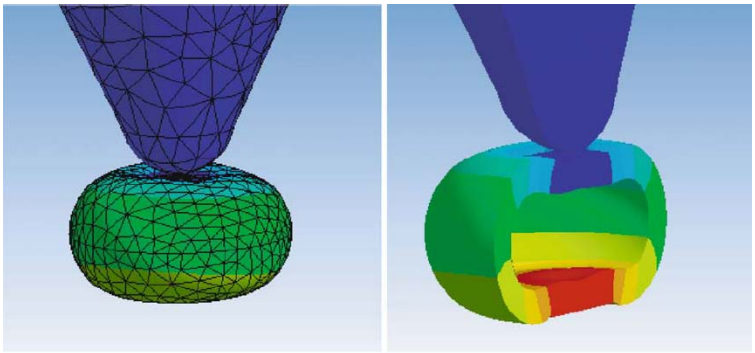

Figure 3.6. The finite element method (FEM). Computer modeling with the finite element method has been frequently applied to extract material properties and stress distributions of materials when deformed by external forces and aid to interpret results from nanoindentation experiments. Image taken from reference [138]

The effect of change of stiffness during maturation in viral retroviruses has been reported for Leukemia murine virus (LMV) and Immunodeficiency virus (HIV) [139, 140]. A two-fold stiffer shell is found for immature particles in LMV than for mature. In the former the shell presented more brittle features. On the other hand for HIV, a 14-fold increment in stiffness is found for immature particles than for mature shells, which provided insights into the internal morphological changes involved during the infection process. The harder virus system reported to date with AFM nanoindentations, is that of Herpex simplex virus I (HSV-1) where forces about 6 nN were necessary to reach full compliance onto the wild type capsid [141]. This study probed that it was possible to squeeze out the contained genome by extreme compression and the genome contributed directly to the stability of the particle.

In order to understand if the force response of these molecular nanoassemblies resembles that of larger objects, the classical theory of continuum mechanics has also being used in attempt to describe and compare the material behavior of the regular protein arrangements with larger shelled structures. Theoretical models for capsid elasticity have been developed to explore the elastic properties of these nanocontainers and to extract mechanical parameters which could be tested by controlled AFM nanoindentation experiments [142-147].

Computational models where the finite element method (FEM) has been used provided information about the stress distribution across thick shells and allowed to vary certain parameters of the shell in order to observe their contribution to the force response (see figure 3.6).

The exciting area of mechanical characterization of viral particles has just started [148, 149]. However experimental results establishing a connection between their mechanical properties with their biological functionality in the process of viral infection are still scarce. These promising first results have paved the way to understand new physical features of entities with a biological character to further aid to understand their hidden structural features. Moreover their mechanical properties will aid to increase our knowledge on their mechanical design which could further promote the vast potential of viruses as tools in medicine and nanotechnology.

4. Polyelectrolyte – Lipid Interaction

4.1 Polyelectrolytes and Lipids

Understanding the interaction between polyelectrolytes and lipid bilayers is important for the fabrication of supported lipid membranes by means of the layer by layer technique. Such systems are promising for the development of novel nanodevices with biomimetic features. The appropriate attachment of lipid vesicles to the substrate, their subsequent rupture, fusion, and, finally spreading at the surface, is controlled by the molecular interaction of the chemical groups of the substrate with lipid headgroups. A functional and continuous lipid layer is a compromise between adhesion, lateral lipid mobility, and organization at the interface. The work presented in this chapter explores the interaction between polyelectrolytes and lipids on the level of single molecules. The processes of adsorption and desorption of individual polyelectrolyte molecules onto lipid membranes are monitored by means of by single molecule force spectroscopy experiments. The interaction energy per monomer can be derived. This allows drawing conclusions concerning the involved binding sites and the related mechanisms. Furthermore, the dynamics of the system are important for the adsorption behavior, because the adopted conformation of the adsorbed chains determines their subsequent desorption characteristics.

As the polyelectrolyte Poly(allylamine) hydrochloride (PAH) was used. PAH is a linear cationic polymer. It has been employed as the substrate for the adsorption of lipid layers on polyelectrolyte multilayers to provide, for example, microcapsules for drug delivery with biomimetic properties. Pure phosphatidylserine (PS), phosphatidylcholine (PC) as well as their mixture were selected for membrane formation.

Scheme 4.1 illustrates the experimental protocol. The AFM tips were functionalized with PAH by means of conjugation. Then test measurements were performed on

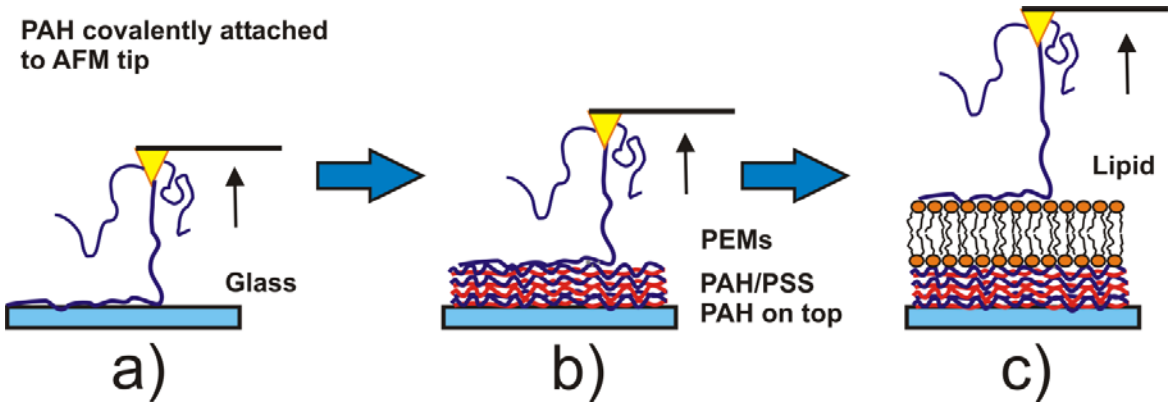

Figure 4.1 Schematic representation of the followed approach to measure single polyelectrolyte-lipid interactions between PAH and polyelectrolyte supported lipid membranes. a) Testing the presence of conjugated PAH chains by means of measuring the interaction with glass; b) Testing for a proper adsorbed polyelectrolyte multilayer with PAH as the topmost layer; c) Measuring the interaction of individual PAH chains with the lipid substrate, which has been deposited onto the polyelectrolyte multilayer.

glass to test for successful functionalization of the tip. PAH chains attached to the tip reveal themselves by the presence characteristic desorption plateaus in the retraction part of force-distance curves. Next, the glass surface was coated with at least 7 polyelectrolyte multilayers having PAH as topmost layer and force distance curves were measured to ensure proper multilayer formation. Finally, lipid layers of various compositions were deposited onto the multilayer cushion followed by respective approach/retraction cycles conducted on different positions of the substrate.

4.2 Materials and methods

4.2.1 Materials.

Microscope glass slides purchased from Carl ROTH GmbH were used as substrates for the posterior assembly of polyelectrolyte multilayers. Poly(allylamine) hydrochloride (PAH MW 70, 000), Poly(styrenesulfonate, sodium salt) (PSS MW 70,000), 16-mercaptohexadecanoic acid (50%), 11-mercapto-1-

undecanol (50%) and N-(3-Dimethylaminopropyl)-N´-ethylcarbodiimide hydrochloride (EDC) were purchased from Aldrich. N-Hydroxysuccinimide (NHS) was purchased from MERK (Schuchardt OHG). Ethylene diamine tetraacetic acid (EDTA) was from Fluka chemika. NaCl was obtained from VWR and KH_2PO_4 from Roanal (Budapest, Hungary). MES was purchased from Sigma. 1-Plamitoyl-2-oleoyl-sn-glycero-3-[phosphor-L-serine] (POPS, sodium salt, 10mg/mL in Chloroform) and 1- Palmitoyl-2-oleoyl-sn-glycero-3- phosphocholine (POPC, 10mg/mL in Chloroform) were purchased from Avanti Polar lipids, Inc. Gold coated cantilevers were obtained from Veeco (Model NPG-10).

4.2.2 Methods

Substrate preparation

Glass slides were cleaned with the RCA-1 protocol t [150]. The glass slides were immersed in a Pyrex bath container solution of Millipore water, ammonium hydroxide (27%) and hydrogen peroxide (30%) in a proportion 5:1:1 and incubated at 70ºC for 30 minutes. Thereafter the slides were rinsed extensively in Millipore water.

Polyelectrolyte multilayer coating

Polyelectrolyte multilayers were deposited by means of the LbL approach. Briefly, 7 layers of PAH/PSS with PAH as the top layer were formed by dipping the glass slides alternately into respective polyelectrolyte solutions of PAH or PSS, 3mg/mL in 0.5 M NaCl, for 20 minutes. Between every coating step the slides were submersed into a 0.1 mM NaCl solution to wash away possible weakly absorbed polymers.

Lipid layer deposition

Unilamellar vesicles, 5 mg/mL lipid in 0.1 M NaCl, were prepared by extrusion of 50 µl of the lipid suspension through a polycarbonate membrane with a pore diameter of 50 nm (Avestin Inc., Canada). The following lipids were used: POPS, POPC, and a 1:1 w/w mixture of POPS and POPC. 30-50 µl of the vesicle suspension were applied onto the multilayer and incubated for 40 minutes at room temperature. After incubation, the lipid coated surface was rinsed several times with 0.1 M NaCl to remove any remaining lipid vesicles. The sample was never allowed to dry and experiments were always, unless specified, performed in 0.1 M NaCl solution.

AFM measurements

After formation of the lipid bilayer the sample was mounted on the scanner of a Molecular Force Probe 3D AFM (Santa Barbara CA, USA). 0.5 ml of 0.1 M NaCl was deposited as a single drop between the cantilever and the multilayer. Before measurement the system was allowed to equilibrate for 20 min. All measurements were conducted at room temperature. The rate on approach was 300 nm/sec. The maximum loading force was limited to 500 pN. Calibration of the cantilever was performed after functionalization by measuring the sensitivity of the optical lever detection after indenting onto the glass. The spring constant of the cantilever was determined by the thermal noise method [72]. The spring constants of the used cantilevers ranged between 0.05-0.1 N/m.

4.2.3 Tip functionalization.

AFM tips can be functionalized either following a silanization protocol or employing thiol chemistry on gold coated tips. The latter method was chosen because its simplicity and good control of the grafting density. The gold coated tips were

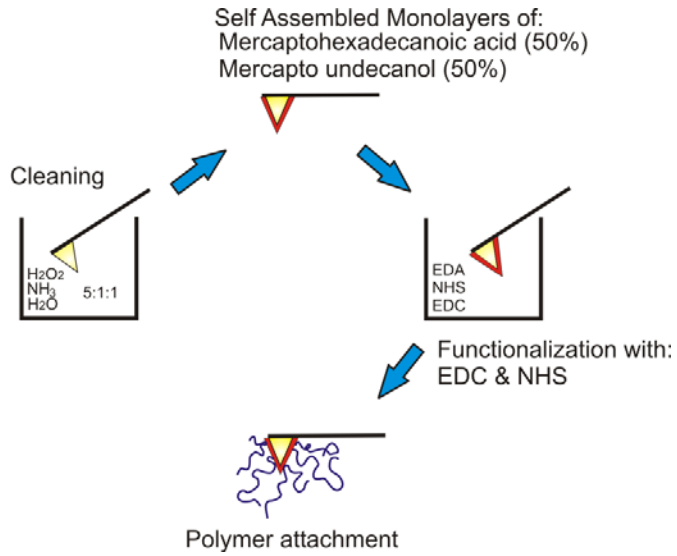

Figure 4.2. AFM tip functionalization with self-assembled monolayers of alkanethiols.

functionalized following the protocol described by Gaub et al [116]. Fig. 4.2 illustrates the conjugation protocol. Gold coated AFM tips were cleaned by immersion of the cantilevers in an aqueous solution of ammonia (30%) and hydrogen peroxide (30%) for 1 hour at 70ºC and finally rinsed with Millipore water. A self-assembled thiol monolayer was formed on gold by incubating the cantilevers for 24 hours in 10 ml ultrapure ethanol containing 1.0 mg 11-mercapto-1-undecanol and 1.44 mg 16-mercaptohexadecanoic acid, respectively. Afterwards the cantilevers were washed repeatedly with ethanol and finally dried. A stock solution containing 1mg N-Hydroxysuccinimide (NHS) and 5mg N-(3-Dimethylaminopropyl)-N´-ethylcarbodiimide hydro-chloride (EDC) in 333 µl MES buffer was prepared by vortexing. 50µl of this stock solution were added to 4950µl MES and the cantilevers were incubated in this solution for 20 min. Immediately afterwards the cantilevers were transferred into a 40% PAH solution and incubated for 3 hours.

Finally, the cantilevers were repeatedly rinsed with Millipore water and stored for at least 6 hours in a 100 mL solution of 1mM EDTA and 0.1 mM NaCl, to prevent contamination from surrounding divalent metal ions.

4.3 Results and discussion

4.3.1 Topology of layers

The topology of the adsorbed polyelectrolyte multilayers followed by the adsorption of the lipid layer was imaged in 0.1 M NaCl immediately after fabrication. Fig. 4.3 displays the obtained images in two different lateral resolutions. The polyelectrolyte coated surface (5.4. a and b) shows a grainy morphology. Distinct grains of about 50 – 70 nm in diameter can be identified. Most of the grains seem relatively flat. A small number of white spots indicate the presence of larger grains on top of the multilayer surface. The roughness of the multilayer surface given by the variance in height was approximately 15.5 nm. Such a topology characteristic for multilayers has been observed before [87]. On the contrary, the roughness of the glass substrate was of the order of only 0.5 nm.

Figures 4.3c and 4.3d show the surfaces after the sample was incubated with POPS/POPC vesicles. The surface texture changed drastically in comparison with the appearance of the polyelectrolyte multilayers. The surface became much more flat and homogeneous. Only a few elevations can be detected. These probably represent the locations of the pronounced spots, which have been detected on the surface of the multilayers.

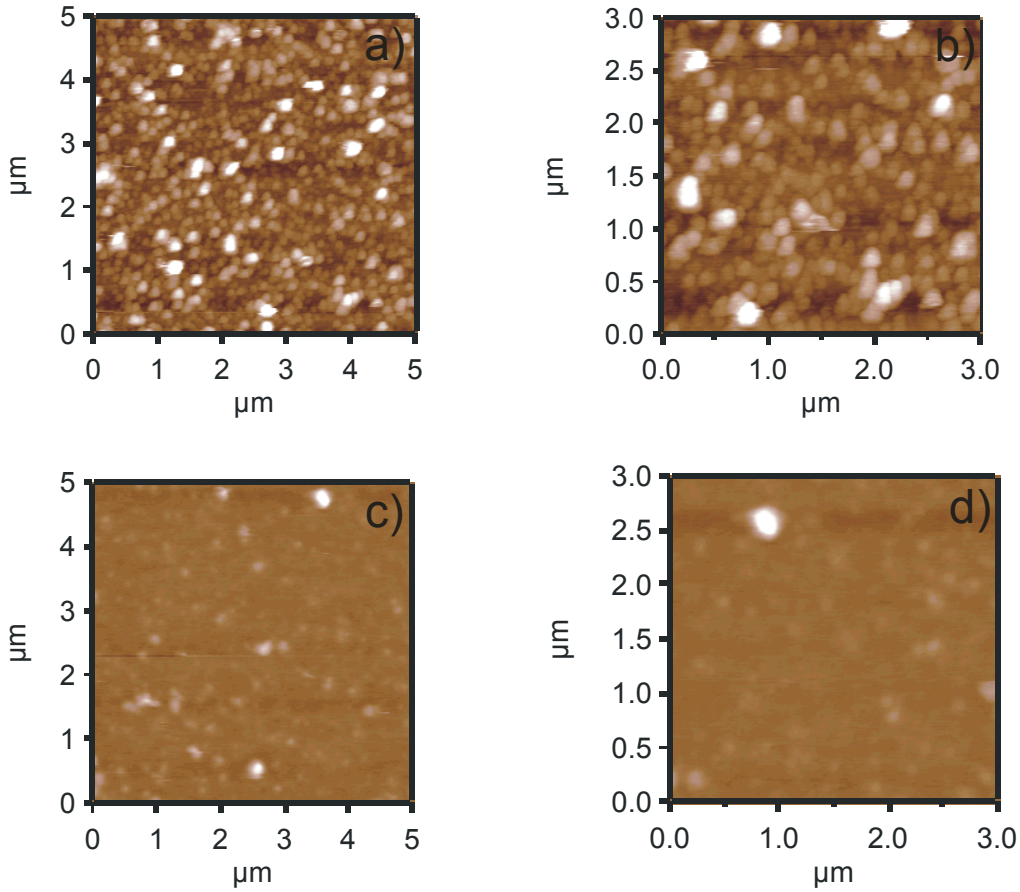

Figure 4.3 Height images in contact mode of polyelectrolyte coated surfaces with the LBL technique of PAH/PSS with PAH as a topmost layer before and after incubation with liposomes. a) and b) without lipid. c) and d) after incubation with POPSPOPC liposomes.

The roughness of the lipid coated surfaces was about 5 nm. It follows from these images that indeed a continuous lipid layer was deposited onto the polyelectrolyte support. Incubation with POPC as well as with POPS vesicles did not result in such a homogeneous and smooth coverage. In this way, the imaging data confirm recently reported experimental results that vesicles composed of a 1:1 mixture of POPS/POPC provided the best results regarding continuity and homogeneity of the obtained lipid coated surface [53].

4.3.2 Desorption of single Poly(allyl amine) hydrochloride polymers from lipid coated surfaces

After covalent functionalization of AFM tips with PAH employing the primary amino groups of PAH, force spectroscopy measurements consisting of repetitive approach-retraction cycles of the tip against the surface under study were performed. It is important to avoid deep penetration of the AFM tip into soft surfaces or even through the lipid layer, otherwise the approach-retraction cycles may yield erroneous results as a consequence of layer destruction and adsorption of layer components onto the functionalized tips. Correspondingly, a force threshold of at most 500 pN was applied.

PAH vs glass.

As a first step, the tip was pushed against the bare glass surface until a maximal loading force of about 500 pN was reached and then it was immediately retracted at a constant rate of 500 nm/sec. In figure 4.4a an approach (red) - retraction (blue) curve of the PAH functionalized tip against bare glass is shown. Upon approach to the surface there is a minimal distance where the sufficiently strong attractive interaction between the coated tip and the glass surface causes the tip to suddenly jump into contact with the surface. This so-called jump-in is essentially an instability phenomenon, caused by the attractive force growing faster with decreasing separation than the bending resistance of the cantilever may compensate for.

The PAH chains adsorb to the glass surface during approach, whenever they get sufficiently close. The following retraction pulls the adsorbed chains off the glass surface. This results in well defined force plateaus in the retraction curves. Whenever a chain finally desorbs a terminating desorption step can be seen. In the provided force-distance curve desorption of two single PAH molecules can be

clearly observed. During the first plateau (left) both molecules are simultaneously desorbed, while in the following plateau (right) only the last remaining single PAH molecule desorbs from the surface. This last desorption plateau accounts for the total unbinding force required to pull an entire single chain off the substrate. These long ranging force plateaus are characteristic for desorption of linear train-like molecules. The presented picture of desorption furthermore proves that the functionalization conditions were appropriate. The number of attached PAH chains was sufficiently low for identifying single chain desorption events. The observed pattern was reproducible over hundreds of force curves. Of course, the number of desorbing chains detected in every cycle is randomly distributed around a mean value.

PAH vs PAH coated surface

In the following experiment the PAH-functionalized tip was probed against the multilayer with PAH as the top layer. A typical approach-retraction cycle is shown in Fig. 4.4b. In this particular experiment the glass surface was coated with 9 layers of PAH/PSS beginning and ending with PAH. A smooth long range repulsive interaction extending over about 50 nm is observed upon approach and retraction of the tip from the PAH coated surface. There is no hysteresis either. This finding is consistent with the intermolecular repulsion of the positively charged PAH on the tip from the PAH at the surface of the multilayer. The Debye length in 0.1 M NaCl is about 1 nm. Therefore one may conclude that the decay of the forces over 50 nm reflect the spatial distribution of the PAH segments around the tip. Assuming that the PAH on the multilayer forms a stratified layer one can therefore conclude that the loose PAH corona around the tip has a thickness of about 50 nm. Further remarkable is that this repulsive hysteresis-less pattern was stable over hundreds of cycles and varying the location on the multilayer. This can be considered as evidence of the stability of the multilayer.

PAH vs supported lipid layer consisting of a 1:1 mixture of POPS and POPC

Fig. 4.4c shows a representative approach-retraction cycle recorded between a PAH coated tip and a polyelectrolyte supported lipid membrane consisting of POPC and POPS in equimolar proportion. The nature of the interaction differs substantially from that recorded on glass and on the polyelectrolyte coat. This proves first of all the presence of a lipid layer, as the tip feels the topmost lipid layer rather than the underlying PAH layer. The approach-retraction cycle contains a number of characteristic features. Upon approach one may observe a jump in at very short distances of the order of 50 - 100 nm in front of the lipid layer. This is evidence of an attractive interaction pulling the cantilever toward the surface. This behavior will be detailed in Fig. 4.5.

When the tip comes very close to the surface, the attractive force changes to a repulsive one. The loading force was restricted to a maximum of about 500 pN in order to avoid perforation of the lipid layer. Such forces are quite below the average normal forces required to perforate a lipid membrane with a regular AFM tip [107, 151]. Withdrawing the tip from the surface leads to an initial pronounced adhesion force of about 1.7 nN with a broad desorption well of about 500 nm in width. Within this distance the shape was quite complex. For larger retraction distances, the single molecule behavior of PAH appeared and constant force plateaus with a final desorption step are obtained. The depth in the adhesion force observed at the start of the retraction curve indicates the total contribution of multiple chains desorbing simultaneously from the membrane surface. As shown in figure 4.4c every desorption step brings the cantilever closer to the base line which is finally approached after the last desorption step. On average the desorption force for a single chain from the POPC/POPS layer was of 114±5 pN. Fig. 4.5 reveals further details. Quite remarkably, there were also plateaus upon adsorption albeit smaller in length than recorded upon retraction. The height of these plateaus was similar to the height of the desorption steps.

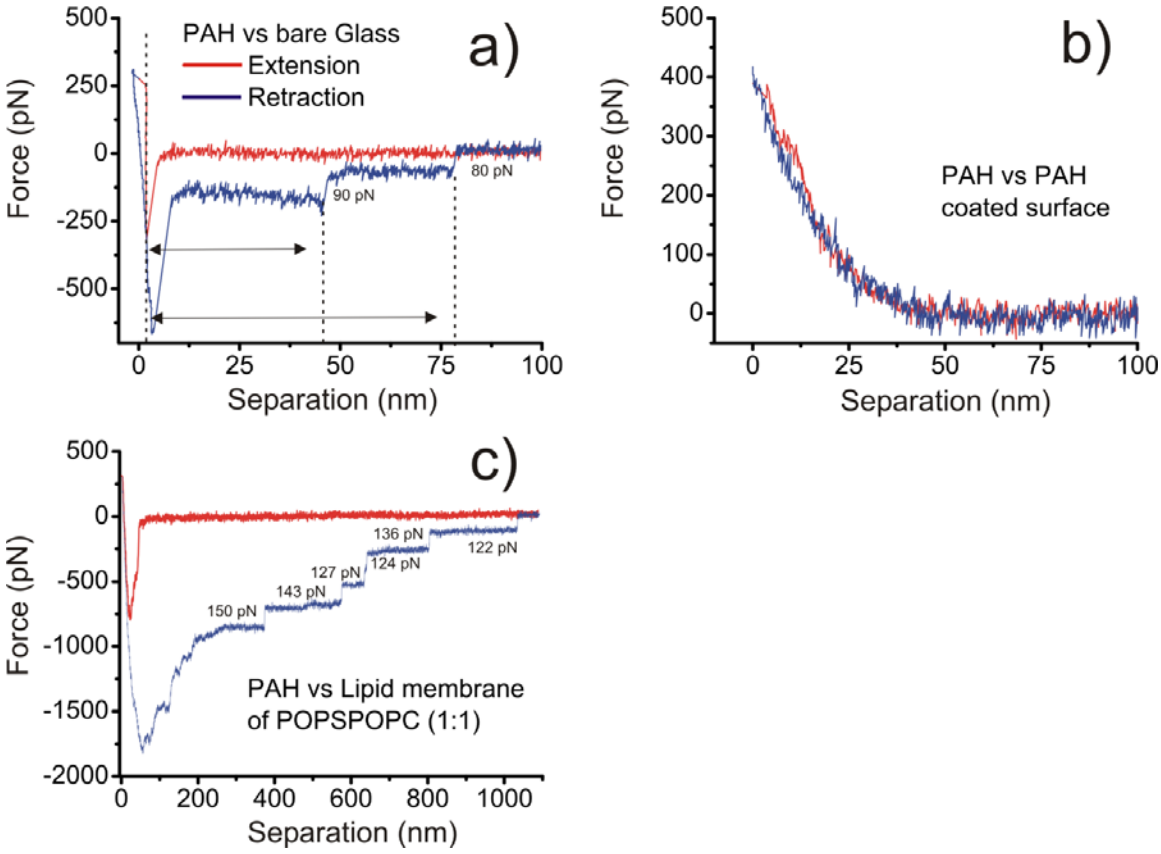

Figure 4.4 Typical approach-retraction curves of PAH functionalized tip against different coated surfaces in 0.1 M NaCl. The approach curves are in red; the retraction part is in blue. a) Glass surface. b) Glass coated with 9 alternate layers of PAH and PSS with PAH as the topmost layer. c) Lipid layer consisting of POPC and POPS (1:1) deposited on the polyelectrolyte layer in b.

The presence of these plateaus evidences a stable situation in contrast to the jump-in behavior recorded, for example, on glass.The plateaus recorded upon approach can only be explained with a constant force pulling the tip toward the surface. This is a rather remarkable behavior, which is not seen in other systems.

When comparing the PAH pulling off the glass surface with that off the lipid layer it is evident, that in case of the lipid layer the desorption plateaus were much longer. This is illustrated in the inset of Fig. 4.6 in the inset. From this observation follows that on lipid surfaces adsorb much larger parts of the PAH chains than on a glass surface although the adsorption/desorption forces are quite similar.

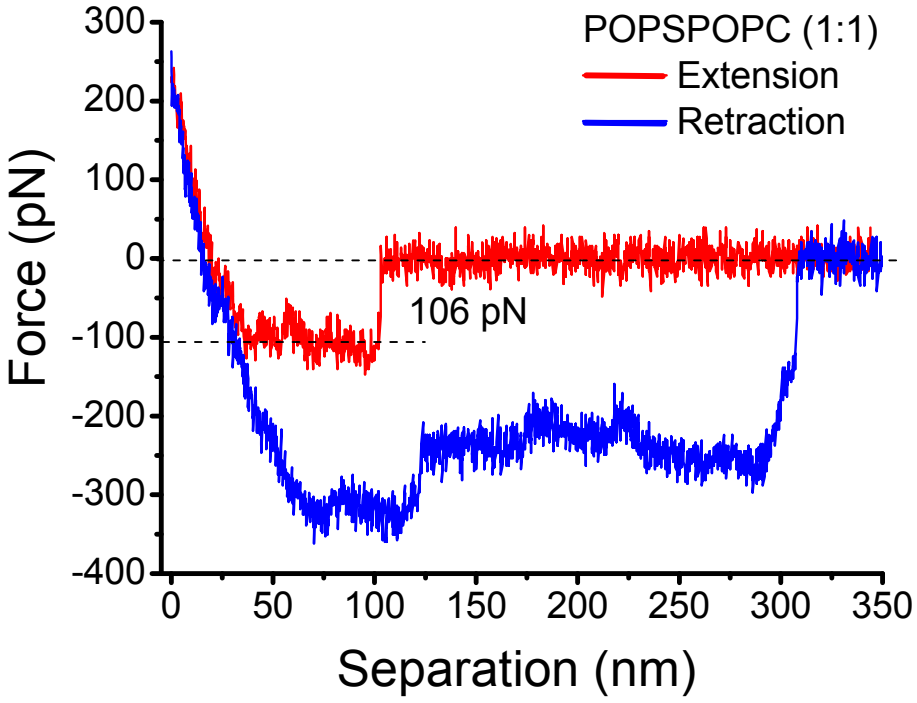

Figure 4.5 Single molecule adsorption. Force-Sep curve with an obvious plateau upon adsorption of more than 60 nm in length.

This is a very interesting finding, which we explain with the fluid nature of the lipid layer in contrast to the solid glass surface. Upon adsorption the PAH monomers bind to the lipid headgroups. The latter are mobile and are thus capable of moving off the spot of the incoming PAH chain. In this way already adsorbed parts of the PAH chain are carried away from the region of adsorption and more and more parts of the PAH chain will subsequently adsorb. Such a situation is not possible on a solid surface.The already adsorbed parts of the polymer prevent further parts of the polymer chain to adsorb at the same site by means of occupying binding sites and also by means of intramolecular electrostatic and steric repulsion between the already adsorbed parts of the chains and the continuously advancing chain. The plateaus on adsorption observed in the case of the lipid surface confirm the suggested mechanism.

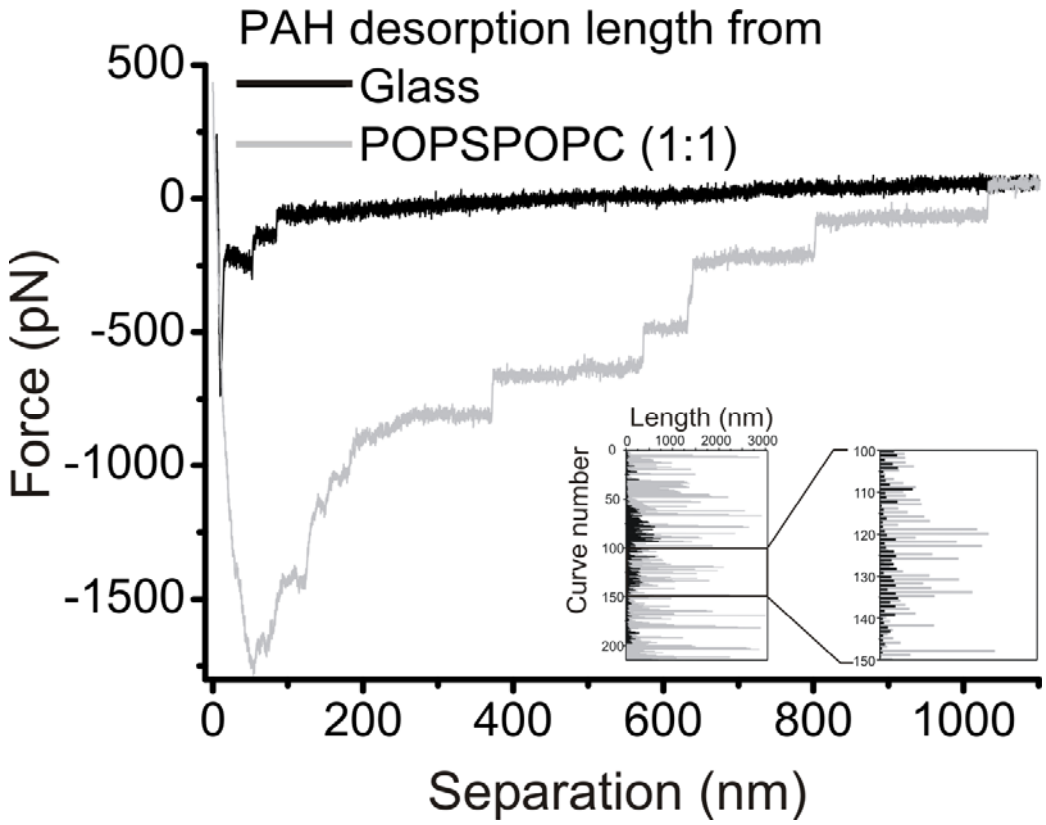

Figure 4.6 Retraction force-separation curves of PAH coated tip from bare glass (dark) and lipid coated (light gray) surface with a POPSPOPC bilayer. The inset shows the clear contrast in desorption length from both surfaces.

They prove that comparatively large segments of the adsorbing chain are continuously deposited on the lipid layer driven by the binding forces between the PAH monomers and the lipid headgroups. This observation is also in line with previously published data on lipid diffusion in polyelectrolyte multilayer supported membranes [53].

We also analyzed the fluctuations of the recorded force curves. The fluctuations contain information about the nature of the support. Fig.4.7 displays typical autocorrelation functions of the force fluctuations for three situations, i) a freely moving cantilever as the control, ii) force noise in the plateau region of a desorbing PAH chain from a lipid surface, and iii) desorbing PAH chain from glass. One can

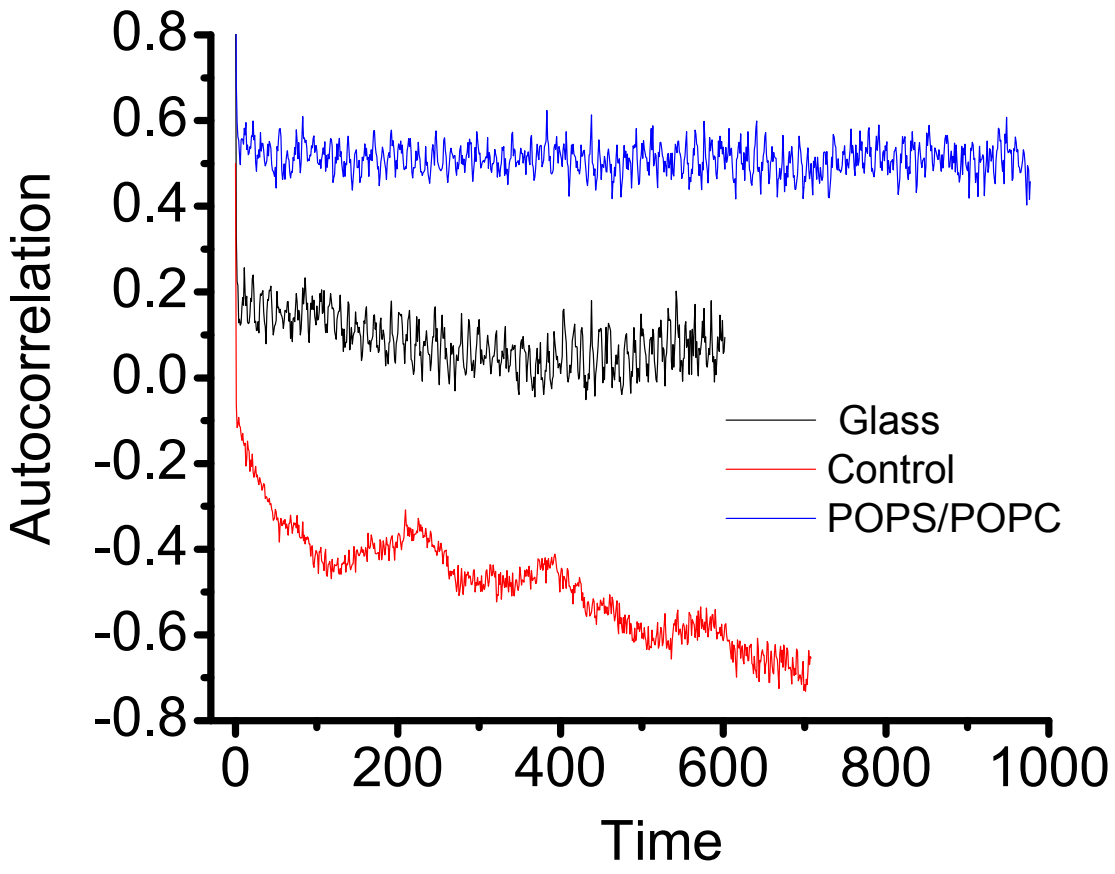

Figure 4.7 Autocorrelation functions of the fluctuations in force in different situations. Free cantilever as a control, PAH detaching from POPS/POPC, and from glass. The measuring frequency was 2000 Hz. 1000 data points are thus equivalent to 0.5 s.

clearly recognize a small periodic component in the case of the control as well as in the case of the desorbing chain from the lipid layer. This periodic component of the force fluctuations is related due to the internal back circuiting of the AFM device, as it appears also in the control.

Fig. 4.8 provides the respective spectral decompositions of the noise in force. Data points are recorded with a frequency of 2 KHz. The periodic component is seen as a peak around 50, which corresponds to a frequency of about 390 Hz. If the tip is connected with the surface by the stretched desorbing chain, damping of the

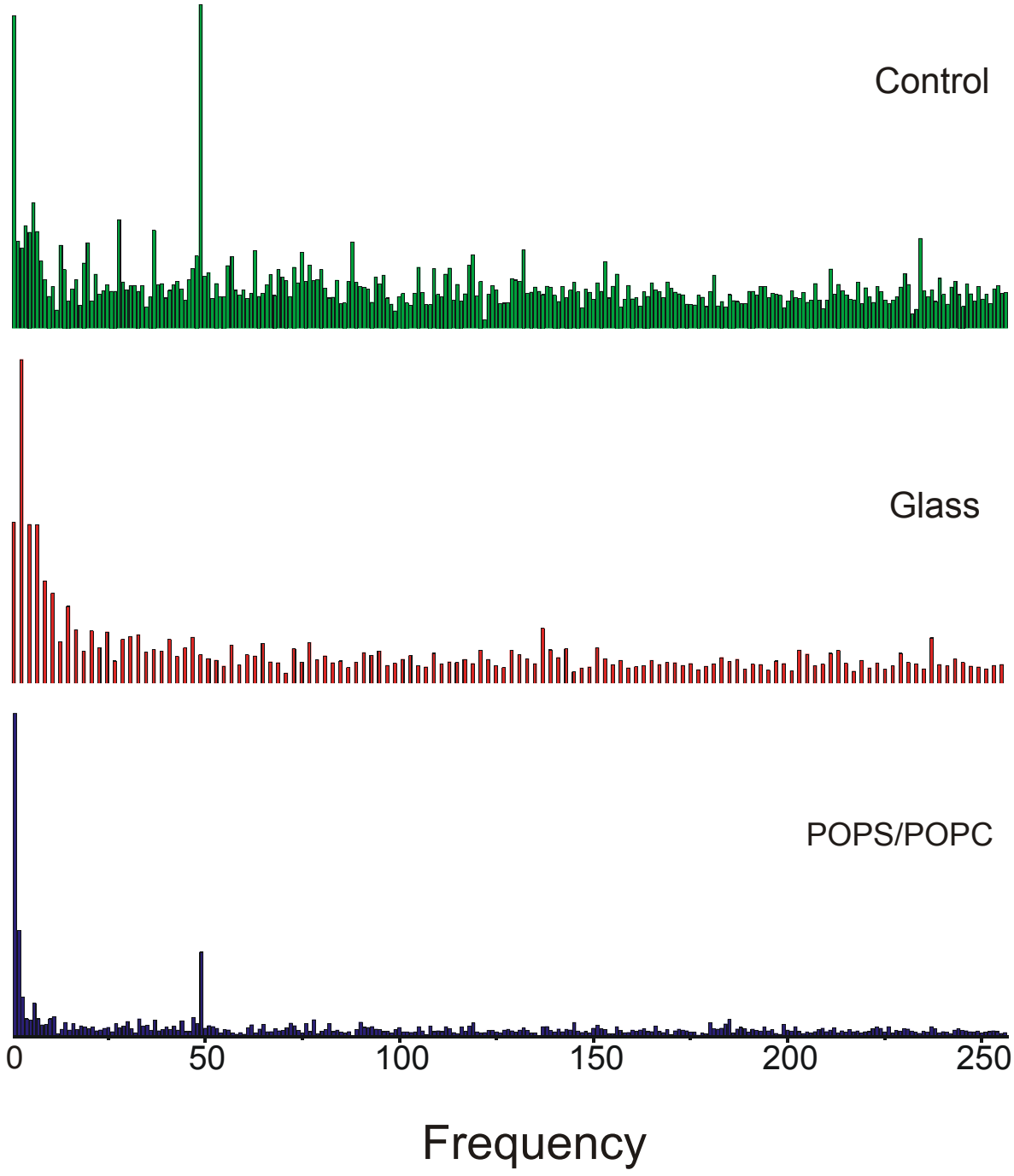

Figure 4.8 Spectral decomposition of the recorded fluctuation of the force corresponding to the autocorrelation functions shown in Fig. 4.7.

periodic component can be expected provided the surface is solid. This was indeed the case for glass. However, when PAH is pulled off from the lipid surface, which is a fluid membrane, damping is insufficient and the fluctuations are still present. This represents further proof of the presence of a fluid lipid layer on top of the polyelectrolyte multilayer.

PAH vs POPS

Fig 4.9 displays a typical approach-retraction curve describing desorption of PAH from a POPS coated multilayer. Two regions have been magnified for sake of a more detailed analysis. The interaction of PAH with the POPS coated membrane resembles with regard to the general pattern that of PAH with the lipid membrane consisting of POPS and POPC in equal proportions. However the curves are noisier and there is a pronounced repulsion occurring over a wider range upon approach. Nevertheless, small plateaus on adsorption can be identified.

The retraction curve in Figure 4.9 shows an interesting feature that occurred sometimes when PAH was desorbed from POPS or its mixture with POPC. It can be seen in the magnification that the final desorption step consisted of two distinct steps. This feature was identified in about 15 % of the recorded desorption plateaus. It can be ruled out that occasionally two independent chains have been simultaneously desorbed because the probability of such an event is much less than 15% given the high temporal resolution of the device.

Therefore, one possible conclusion is that the chain was actually a loop and not a single chain. In this case always two monomers will be almost simultaneously desorbed from the surface. This follows from the consideration that always both parts of the loop must be stretched.

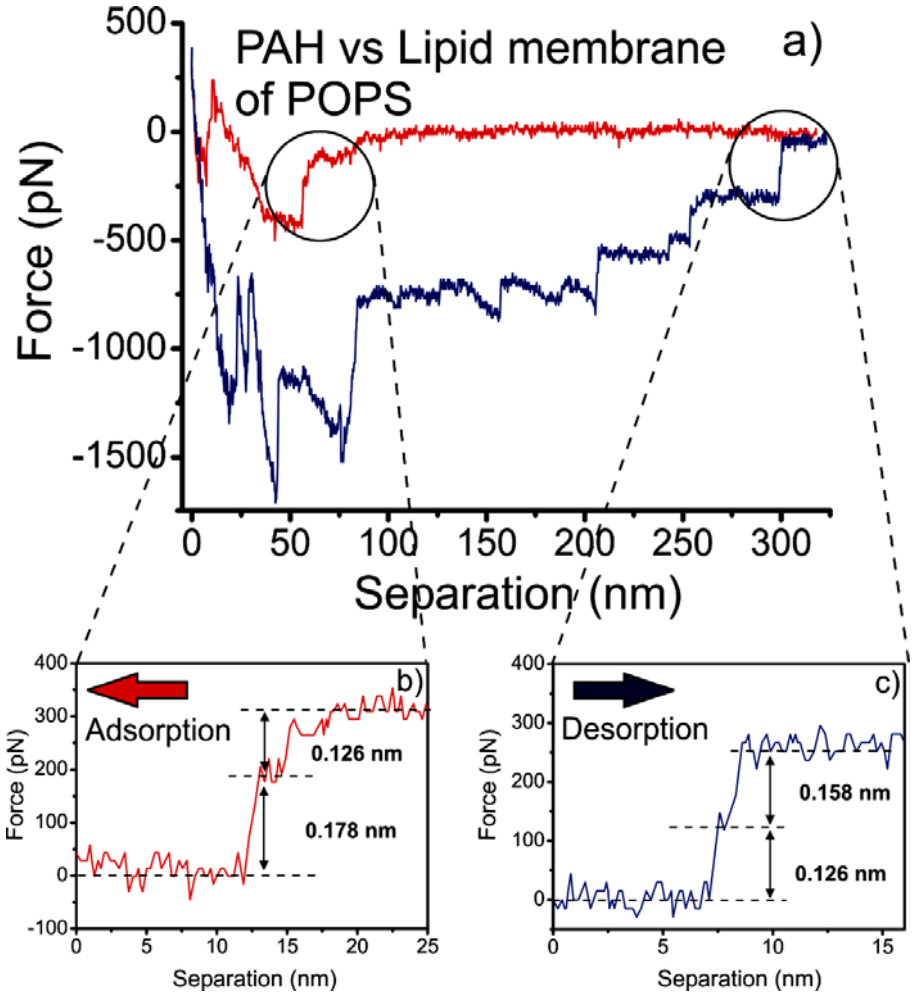

Figure 4.9 PAH coated tip vs a POPS coated surface. a) Full approach retraction cycle. b) Zoom on single adsorption events at the site of contact during approach. c) Two final desorption steps.

A loop with one loose part seems impossible in the case of a fluid interface because the gain in energy due to adsorption will immediately stretch any eventually loose part of a loop. The indicated distances refer to the increment of the chain length occurring at the respective desorption steps. These numbers are consistent with the monomer length taking into account the bond angle and the bending resistance of the polymer.

Another possible explanation is that the chain was intercalated between lipid layers. This, in principle, seems possible, because, especially, in the case of POPS

the lipid layer is not fully regular and may contain patches of multilayers or incompletely spread vesicles. In such a situation more than one binding site per monomer could interact with lipid layers. In the case of POPS this could be the phosphate group and the carboxyl group of the lipid headgroup.

PAH vs POPC.

The interaction of PAH with a lipid coated surface formed after incubation with POPC vesicles showed a different response in the approach-retraction curves compared with the case of POPS and its mixture with POPC. Typical cycles are shown in Fig. 4.10. There was neither an attractive pulling force upon approach nor a strong adhesive interaction during withdrawal. Although force plateaus were also obtained, the height of the plateaus and its frequency decreased considerably. The repulsive behavior upon approach together with the weaker desorption steps indicated a weaker interaction of PAH with this zwitterionic lipid. The repulsive behavior can be attributed to intramolecular electrostatic and steric repulsion of the PAH chain upon approach.

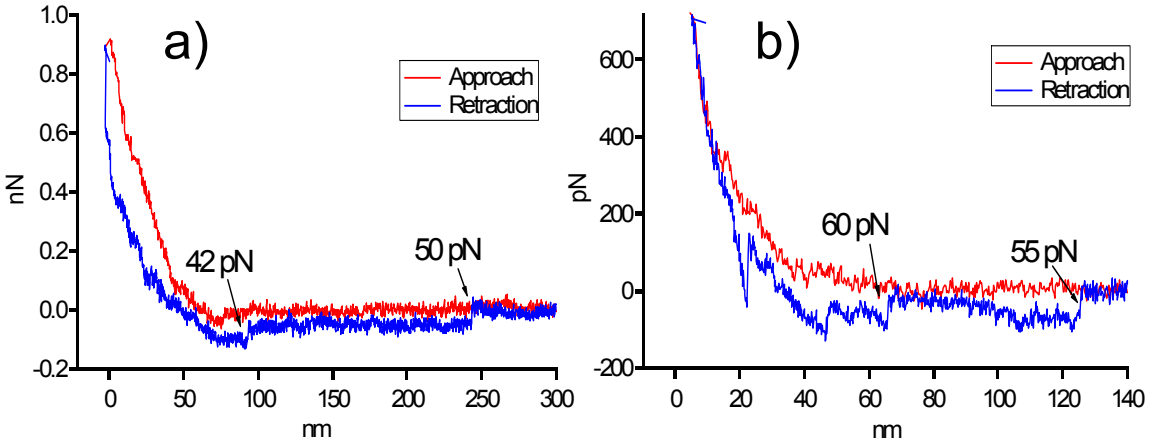

Figure 4.10 Representative approach-retraction cycle, Force vs Separation curves of PAH coated tip against a POPC coated surface.

The rather short lengths of the desorbing chains together with the observed repulsion indicate a limited movement of the adsorbed part of the PAH chain on the lipid layer. This can be explained by missing connectivity of the lipid layer. The adsorbed POPC vesicles do not spread on PAH because the attractive interaction between PAH and the POPC headgroups is insufficient.

4.3.3 Quantitative analysis of the adhesion and desorption behavior of PAH

The force corresponding to the last remaining plateau can be unambiguously related to desorption of a single PAH chain or to a loop. The same is true for the first plateau upon adsorption. It has to be kept in mind though that the longest chains are the last ones to desorb from the lipid layer upon retraction. Therefore there is a diminished probability of loops to be recorded upon desorption. The occurrence of loops is in principle possible, because the conjugation protocol does not exclude the formation of PAH loops on the tip. The forces corresponding to the last observed plateau upon desorption were collected for the various investigated surfaces. The same was done where applicable with the first plateaus recorded upon adsorption. The distributions of the recorded forces were plotted as histograms. Fig. 4.11 shows the respective force distribution for the case of desorption. As a rule, the obtained distributions for desorption forces displayed more than one peak. The obtained histograms were fitted with superpositions of Gaussian distributions based on least squares to obtain the mean force for every observed peak together with its widths and weight. The fitted parameters are summarized in Table 1. In some cases a shift factor was provided. The shift factor applies only for the case when the second peak was considered to represent loops. The numerical value of the shift factor provides an estimate of how much the loop desorption force was smaller than the sum of two single chain desorption forces.

Let us first consider desorption force distribution in the case of glass. The histogram consists of at least three distinct peaks. There may be a fourth peak at 170 pN. But there were too few events to ensure a proper fit. The situation appears quite complex There is no straightforward explanation for the observed distributions of desorption forces. For example, the peak centered on 145 pN can be attributed to loop desorption as its mean value is about twice as much as the first peak at around 69 pN. However, the intermediate peak centered on 109 pN does not fit into this simple scheme. It is very difficult to find a proper explanation. The PAH molecules are homogeneous. Desorption under an angle should not lead to the occurrence of an extra peak, since only the vertical component of the unbinding force influences on the deflection of the tip. The surface of the glass may not be flat in a local scale.

This would explain the broadening of the peaks but not the occurrence of more than two distinct peaks in the force distribution. At present one may only speculate about the nature of the peaks. One possibility is that PAH self-organizes upon adsorption onto the glass surfaces in specific patterns as a result of intramolecular electrostatics and steric interactions. This may lead to different conformations of the adsorbed chains.

A simple example would be that due to steric constraints and electrostatic repulsion not every monomer binds to the glass surface. The strong electrostatic interactions between neighboring groups would lead to persistence of adopted conformations on a local scale. The conformation of the last remaining chain may correspond to a local minimum of free energy and thus would observe a specific desorption force, although interaction with other chains are already switched off. In this framework of interpretation the first peak would correspond to an adsorbed PAH, which was more weakly bound. The second peak centered on 109 pN would then refer to a more strongly bound conformation and the third and the fourth peak would correspond to the respective loops.

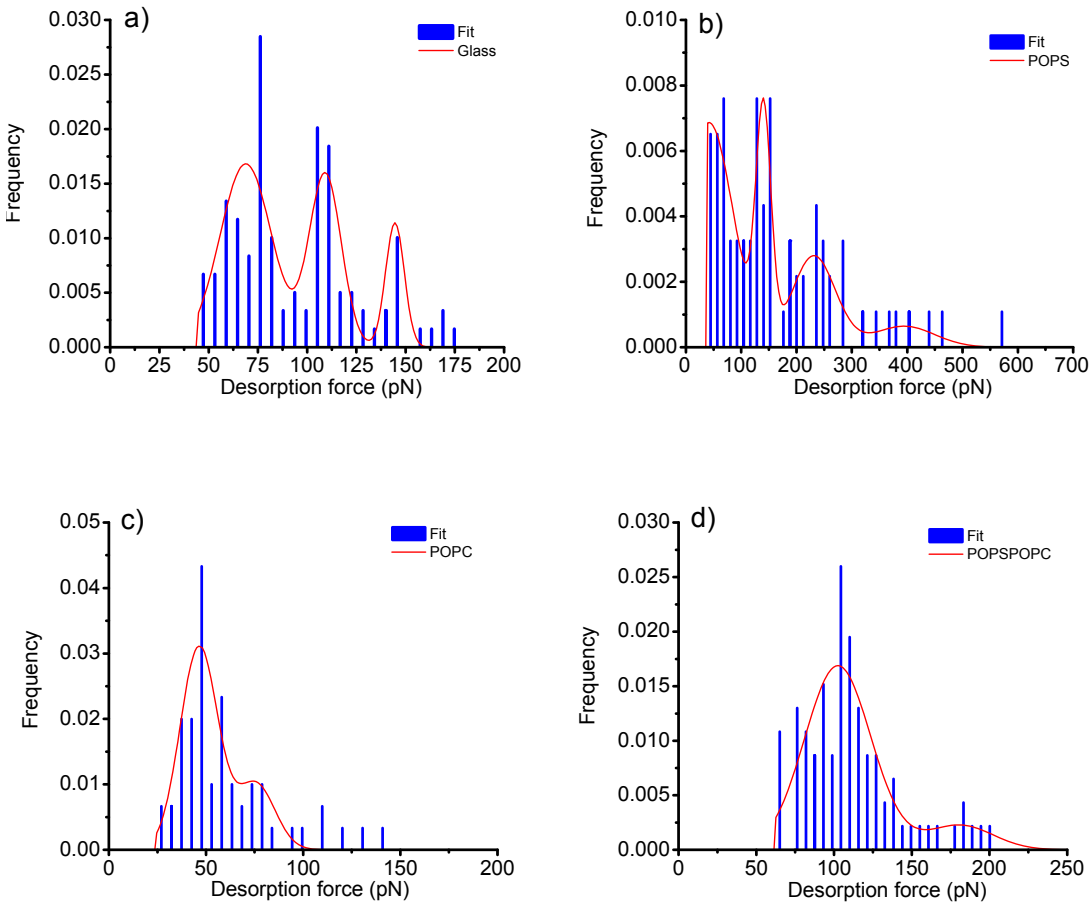

Figure 4.11 Last desorption force histograms from different investigated surfaces. The red curves show the obtained best fits with multiple Gaussian functions.

Adsorption and desorption of loops is schematically shown in Fig. 4.11. The desorption force of a loop may be smaller than the corresponding sum of the single chain desorption forces, because intramolecular electrostatic interactions between the two parallel pulled chains may contribute to desorption. Repulsion between the two chains should lead to bending moment and this transforms into a stretching force applied to the chain, which may weaken the interaction with the binding sites due to distance increase between the amino groups of PAH and the binding sites on the substrate.

The desorption force histogram for the POPS case is shown in Fig. 4.11b. It is also a rather complex distribution of desorption forces with at least four distinct peaks ranging from 42 pN to almost 400 pN. Since the POPS headgroup carries two negative charges and one positive charge one could expect a strong interaction with the amino groups of PAH. As already mentioned above the POPS layer adsorbed on polyelectrolyte multilayers is probably not a bilayer, but contains patches of lipids and non-completely spread vesicles. Therefore, various interaction scenarios of PAH with the POPS layer seem possible.

PAH may intercalate between POPS. This situation may account for the higher range of the observed desorption forces. The cluster at 42 pN is very difficult to explain. It is unlikely that such a small desorption force may occur between POPS and PAH. It may be an artifact and may be related to a lipid contaminated PAH chain. This may happen if PAH destroys patches of POPS upon adsorption which were not firmly attached to the polyelectrolyte support. In this situation the PAH chain may get decorated with POPS. Upon retraction we would thus not see the expected strong interaction between POPS and PAH.

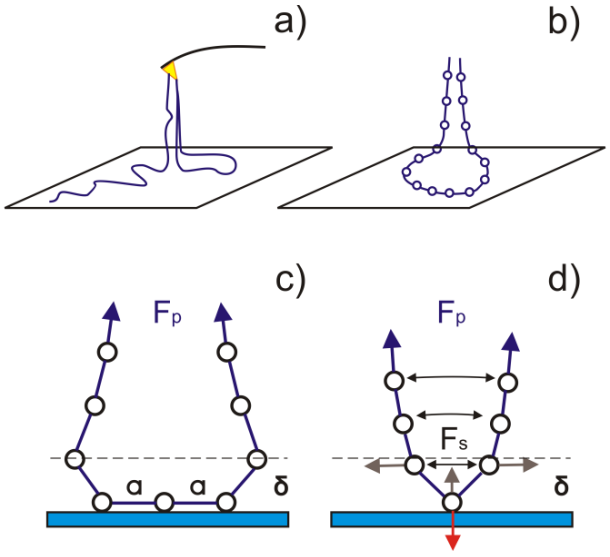

Figure 4.12. Scheme of loop desorption. a) Simultaneous desorption of single molecules and loops. b - d) subsequent stages of loop desorption.

Surface	Mean value [pN]	σ [pN]	weight	Shift factor
Glass	68.9	13.2	0.53	
	109.2	8.2	0.32	
	144.6	4.7	0.13	
POPS	42.2	43.6	0.4	
	140.7	13.4	0.23	
	231.7	39.2	0.27	
	395.0	55.1	0.08	
POPC	46.6	9.8	0.75	0.81
POPSPOPC	102.6	21.4	0.87	0.88

Table 1 Fitted distribution parameters for PAH desorption forces.

In the case of POPC we see one desorption force peak at about 47 pN. The second peak can be attributed to loops. In the case of the mixture of POPS with POPC we see one very well pronounced peak centered on 103 pN.

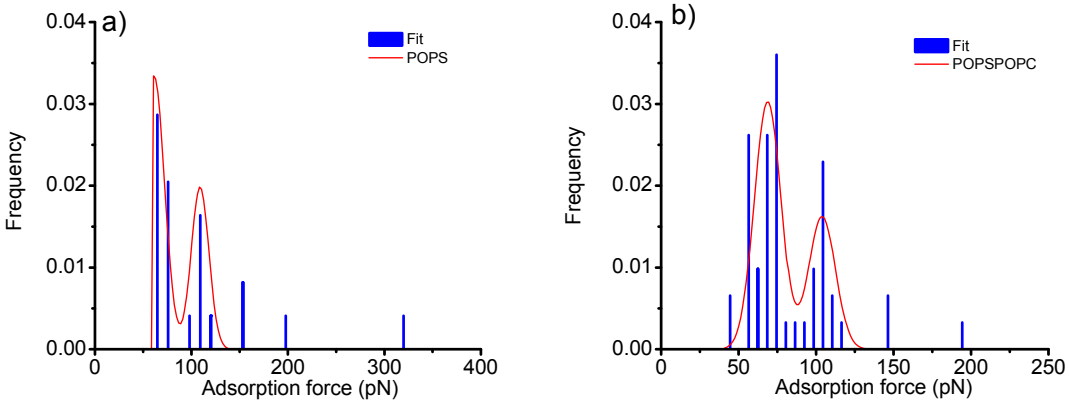

Figure 4.13 Histograms for the force values of single adsorption steps for a) POPS and b) the lipid mixture.

Surface	Mean value	σ	weight	Shift factor
POPS	61.6 109.3	10.9 9.1	0.54 0.45	
POPSPOPC	69.0	8.6	0.65	0.75

Table 2 Fitted distribution parameters for PAH adsorption forces.

The second peak is rather small and can be related to a small number of loops. In the case of the mixture the desorption behavior is consistent with the presence of a continuous and homogeneous fluid lipid membrane. There is one main desorption force peak and a very small contribution of loops as should be considering the low probability of catching loops as the last desorbing entity. Plateaus on adsorption were only obtained in the case of POPS and the mixture of POPS with POPC but never seen in approach curves toward glass surfaces.

Adsorption force histograms are shown in Fig. 4.13 b and c. The fitted parameters are provided in Tab. 4.2. For POPS and its mixture with POPC there are two peaks of adsorption forces which can be interpreted as single chain adsorption and loop adsorption, respectively. In the case of POPS the first peak is centered on 61 pN. This seems low compared with the recorded desorption forces. This is an interesting finding. It shows that the first binding event occurs only with one of the charged sites of the POPS headgroup. If the second site has a slightly lower rate of binding one would never see it in adsorption as it does not led to a decrease of the length of the free part of polymer chain.

During the process of adsorption, as shown before in Figure 4.5, the fluid nature of the membrane plays an important role in adsorption. It ensures that long chains become adsorbed, because the already adsorbed part of the chain is being transported off the side of adsorption. When a polyelectrolyte chain, which is attached at one end to the tip, adsorbs onto a horizontal lipid membrane it has to bend by π/2 near the point of attachment. The shape of the adsorbing chain is governed by the interplay of bending resistance and adsorption energy. The shape of the molecule is that of an elastic stick kept vertical at one end, while the other end is pressed toward a horizontal hard surface. The analytical solution for the shape is well known [152, 153]. The bending stiffness, C, is equal to $k_BT \cdot L$, where L is the persistence length. K_B is Boltzmann´s constant and T is the absolute temperature. There is an intrinsic length scale of the arcuated polymer chain, which is equal to $\sqrt{C/2 \cdot W}$, where W is the work of adhesion. If the pull height is large, the point of attachment of the chain with the surface is two times the intrinsic length off the vertical. This shape of the adsorbing polyelectrolyte chain ensures apart from rotational motion of the adsorbing chain unidirectional transport of the adsorbed chain off the site of adsorption, because of the bending energy contribution fluctuations of the chain position become asymmetric around the adsorption site.

4.3.4. Driving forces and biding sites in PAH adsorption/desorption from a lipid coated surface

Until now the general features of the adsorption-desorption process have been discussed without directly referring to the molecular nature of the binding interaction. This will be discussed now. We assume that the major contribution of binding can be attributed to short range forces, because long-range electrostatic forces become effectively screened in 0.1 M NaCl with a Debye length of about 1 nm [112]. The distances recorded during the force steps together with the magnitude of the measured forces, strongly suggest hydrogen bonding as the main molecular mechanism of interaction between PAH and glass as well as between

PAH and lipids. Additionally, electrostatic contribution beyond the range of hydrogen bonds will somewhat contribute to the total binding energy.

Let us first consider first the case of desorption of single PAH molecules from glass in 0.1 M NaCl. The structure of silicate glass surfaces and its capacity to form hydrogen bonds with water in aqueous solutions is well known [154]. The responsible mechanism of charge acquisition by the glass surface becomes charged by means of dissociation of the silanol groups at the interface.

Water molecules form bridges with the silanol groups by hydrogen bonding (see figure 4.14a. For the case of PAH adsorption, is very likely that the hydrogen bonds formed by the water molecules are replaced by hydrogen bonds established between the PAH primary amino groups and the silanols keeping this way the polyelectrolyte segment firmly attached to the surface. The driving force is the release of immobilized water molecules from the glass surface which is equivalent to an increase of entropy.

PAH carries amino groups every 0.22 nm along its backbone where each amino group is rotated 120^{o} from the next one. Then, as shown in the molecular model of figure 4.14b, there is an amino group every 0.67 nm pointing toward the same direction. This situation is illustrated Fig. 4.14c. It shows that after part of the polymer has become adsorbed it will inhibit further adsorption of the remaining segments due to electrostatic and steric repulsion. During retraction of the tip, the desorption force observes comparatively short force plateaus as shown in Fig. 4.14d. The energy involved in a single N-H---O hydrogen bond is about 3.2 k_BT (8 kJ/mol). The relationship between desorption energy per unit length and desorption force for a polyelectrolyte chain is given by

$$F_{des} = \frac{E_{bind}}{l_a} \tag{4.1}$$

where F_{des} is the last step from the desorption plateau, and l_a is the distance between neighboring amino groups.

Assuming that the first peak of the desorption force histogram corresponds to single chain interaction we find a value for the binding energy of about E_{bind} = 15.18 x 10^{-21} Joules, or in energy units of 3.7 k_BT, this is somewhat lower than the energy for a single hydrogen bond (k_BT = 4.11 x 10^{-21} J). This is expected because there is a trade off with energy of two hydrogen bond formed with water, which have to be broken. Both, from the amino group and from the glass surface one water molecule have to be released, before a new bond between the two can be formed. This argument underlies the importance of entropy increase caused by the release of

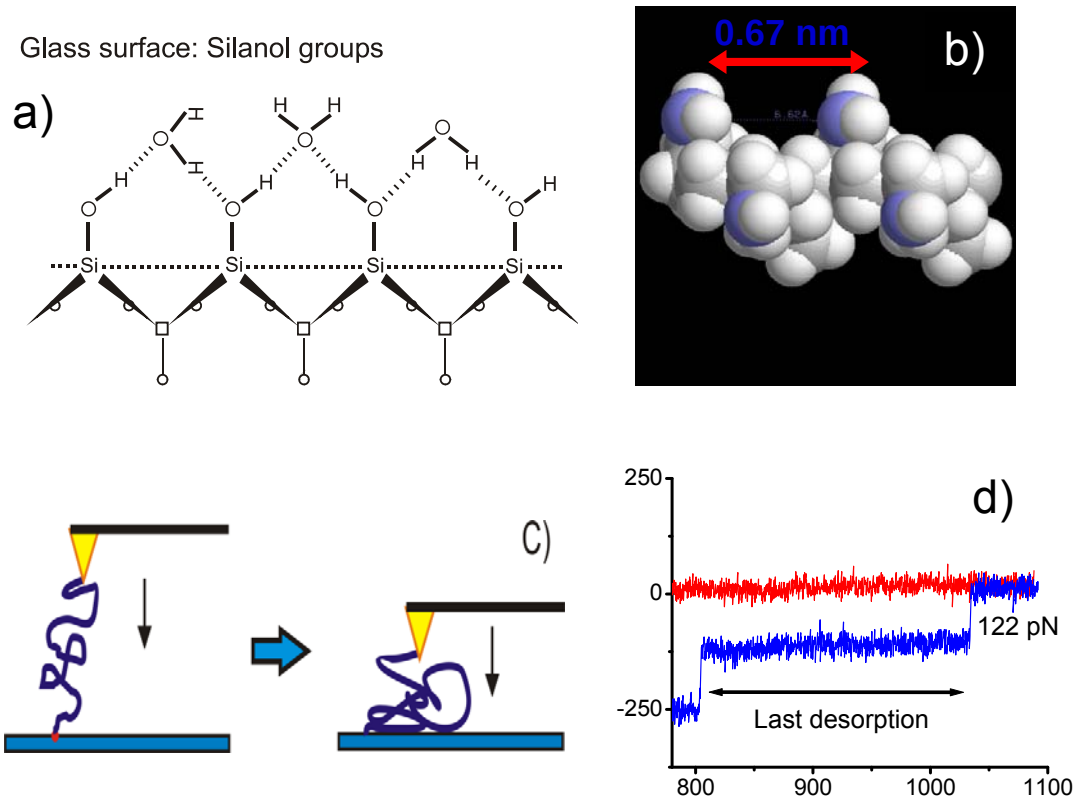

Figure 4.14 Molecular bond formation between PAH and silica surfaces.

bound water as the driving force for adsorption. The other two most frequent values yield 5.8 k_BT and 7.7 k_BT.

Desorption of single PAH molecules from lipid coated surfaces provided well defined differences in the measured force. We discuss first the cases for the two pure lipid species.

The interaction energy per segment for the two most frequent desorption force values found for POPS is 2.3 and 7.5 k_BT. The frequency and difference in magnitude these two values shown in the histograms of force desorption strongly indicate that two binding sites could be involved for POPS.

The other two less frequent values were 12.3 and 21.14 k_BT. These higher values for the unbinding energy probably represent multiple unbinding events during the process of desorption. In the case of POPC, there was a single peak in the desorption force. The estimated unbinding energy is 2.5 k_BT.

We observe that the lower limit for the unbinding energy is almost the same as for POPS. This could mean that in both cases a single bond has been broken. We also realize that this binding energy is lower than that obtained for single bond breaking on glass.

As shown in figure 4.15, the PAH amino groups can interact with two specific binding sites in the POPS head group: the phosphate group PO_2^- and the carboxyl

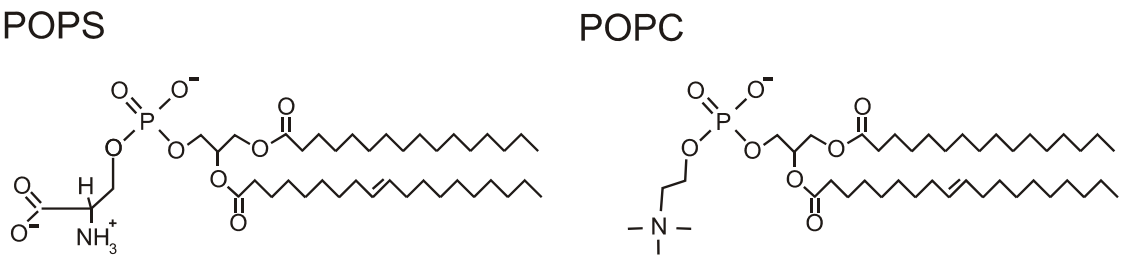

Figure 4.15 Structure formulas for POPS and POPC.

group COO^-. On the other hand for POPC, the only possibility for bond formation is with the phosphate group. The small strength of attractive interaction between PAH and POPC, agrees very well with earlier experimental results where it has been

found that the force between POPC vesicles and PAH coated surfaces is attractive enough to maintain the vesicles attached to the surface but not enough to induce rupture of the vesicles [53]. Furthermore, the presence of quaternary ammonium groups in POPC could introduce a repulsion term against the binding force between PAH and the lipid head group.

For the lipid mixture a desorption energy of 5.4 k_BT is obtained. POPC provides one potential binding site, whereas POPS provides two potential binding sites with PAH. If binding would be equally probably, one would expect to find more frequently unbinding events with energies of about 2.4 k_BT as in the case of POPC alone. This trend is not observed. In fact, the obtained value is closer to the desorption energies found for POPS. We think that this related to electrostatic attraction of POPS to PAH steering the amino groups to POPS. The POPC molecules in-between the PSS may play a role of a lubricant increasing the flexibility of lipid adjustment to the PAH chain.

Similarly, for the cases of adsorption, the obtained force values 62, 69 and 109 pN would correspond 3.3, 3.7 and 5.8 k_BT respectively. Interestingly, the energy values found for adsorption for POPS and the lipid mixtures, support the idea of a more favorable binding site determining the initial adsorption onto the lipid layer.

The physical properties of individual molecular bonds, has been previously investigated in detail [54-56]. In the Bell-Evans theory, bond lifetime depends on how fast the unbinding force is applied and the expected survival time provides the most likely breakage strength in the force for certain loading rate.

One may argue that the observed long plateaus obtained during retraction may be due to lipid tether pulling rather than due to polymer chain pulling and desorption. There are several arguments which we think support the idea of polymer desorption instead of tether formation.

a) The measured rupture forces are of the order of 100 pN, which corresponds to a rupture tension of about 1 mN/m assuming a tether of a diameter of about 20 nm.

This is a very small value for the rupture tension of a bilayer, and additionally the diameter of the tether is very small. More realistic sizes of tether would result in still smaller values of rupture tension.

b) We see several plateaus upon retraction. In terms of the tether hypothesis this should correspond to several tethers or to a complex multilayered tether. The first case is very unlikely, because of the limited size of the tip. The second case is unlikely, because a multilayered tether will be also very thick and the pulling force will be correspondingly high, because of the additional work required to form a multilayer from a bilayer.

c) Both the membrane support and the tip surface are made from the same material, PAH. Pulling tethers would thus require a stronger binding force of lipids to the tip than to the surface. This seems quite unlikely, because there is much more PAH on the surface than on the tip, and not all the PAH molecules on the tip transmit the force. Only the stretched ones would effectively hold the “tether”.

d) At least in the case of the mixed system POPS/POPC, we have a flat bilayer and it is difficult to imagine where the tethers would come from without creating a hole in the bilayer on the surface. As already mentioned before, the loading forces applied against the surface with the AFM tip did not exceed 400 pN, which is quite below the necessary forces to puncture a bilayer which are of the order of 1.5 - 6nN [151].

Finally, e) the plateaus upon approach seem to be inconsistent with the tether hypothesis. If there is a lipid droplet on the tip, then during close approach there should be an initial repulsive force just before contact, instead we obtain an inverted step-like pattern followed by a constant force plateau over distances of about 50 nm (See figure 4.5 and 4.9b). This pattern strongly suggests that polyelectrolyte is being adsorbed.

4.4 Conclusions

The adsorption and subsequent desorption behavior of individual molecules of Poly(allyl amine) hydrochloride onto/from lipid coated surfaces was investigated by means of single molecule force spectroscopy. A multilayered film formed by the consecutive assembly of oppositely charged polyelectrolytes and subsequently coated with lipids of Phosphatidylserine or Phosphatidylcholine or their equimolar mixture was used as a platform for adsorption and subsequent desorption of single PAH chains. Single chain adsorption and desorption events, were reflected as long plateaus in force – separation curves. These results were compared with the adsorption behavior on bare glass. It was observed that the fluidity of the membrane contributed to the reorganization of the adsorbing chain at the interface, providing more available binding sites as the chain was approached to the surface. Therefore, spreading of long PAH segments was demonstrated. The mechanism of adsorption resembles a rolling nanomachine where the adsorbing chain is maintained at a constant pulling force.

The short range of the measured interaction forces together with their magnitude, strongly indicates that hydrogen bonding is the main binding mechanism between the PAH amino groups and the charged moieties at the lipid head groups. It was found that while for the case of POPC the binding occurs only at the phosphate group, for the case of POPS, hydrogen bonding can occur at the phosphate groups as well as at the carboxyl group. Entropy increase during adsorption through release of bound water molecules and counterions contributes to the strength of binding, which was of the order of a few k_BT per monomer.

5. Polyelectrolyte brushes as potential responsive nanostructures

Novel nanotechnological devices should be able to perform defined functions in a controlled fashion. This requires the development of proper responsive smart materials. In this regard polyelectrolyte brushes may play a special role with attractive electronic, industrial and biomedical applications, because PE brushes respond with a collective change in the conformation of chain molecules as a function of applied external stimuli. In this way a brush can be considered as a mechanotransducer in the nanoscale. This responsive functional property, however, has to be maintained and be fully reversible for long periods of time; otherwise the function of the nanodevice will be lost. A better understanding of the responsive properties, the stability and the reversibility of PE brushes therefore requires studying the nanomechanical properties of polyelectrolyte brushes as a function of salt concentration. It is expected, that these investigations could facilitate the use of surface modification for the production of new coatings with unique attributes with regard to abrasion, lubrication, friction, or, for example, hydrophobicity.

The following experimental results are devoted to the characterization of the surface interactions of a Potassium 3 – Sulfopropyl Methacrylate (PSPM) brush and its responsive features. The brush response is probed with external loading forces and with varying salt concentrations.

5.1 Materials and Methods

Materials

Potassium 3 – Sulfopropylmethacrylate (SPMA), 2,2´-bipyridine (bpy), $Cu^{I}Cl$, $Cu^{II}Cl_2$, ethyl 2 – bromoisobutyrate (2 – EBiB), mercaptoundecane or blank thiol.

Obtained from Aldrich chemicals: ω – mercaptoundecyl bromoisobutyrate (thiol initiator) and 1- dodecyl - 3 – methylimidazolium bromide.

Methods

Brush Synthesis: "The grafting from" technique

The "grafting from" technique was applied to fabricate dense brushes by atom transfer radical polymerization (ATRP). The brushes are grown from thiol assembled initiating monolayers onto gold coated surfaces [155, 156]. The formation of Poly (Potassium 3 – sulfopropyl methacrylate) (PSPM) brushes was accomplished by using *Arrandee* gold coated pre-annealed glass substrates as surface platforms for growth. According to reference [59] the brushes are grown as follows. The substrates were immersed for 3 hours in a polymerization solution were the reaction of 1.24 g of SPMA, 0.75 mL of distilled water and 1.25 mL of DMF were mixed in a Schlenk flask and degassed with nitrogen. A stock solution of Cu-bpy was prepared by addition of 2 mL of degassed water to 39.6 mg of CuCl, 53.8 mg of $CuCl_2$ and 312 mg of bpy. From the stock solution of Cu-bpy, 19.5 mg of 2-EBiB and 0.5 mL of Cu-bpy were added to the SPMA solution to follow polymerization. After the polymerization reaction the substrates were washed repeatedly with ethanol and water.

AFM Measurements

All force measurements were made on a Molecular Force Probe 3D (Asylum Research CA, USA) in dry state or under liquid conditions and at room temperature. Silicon nitride Si_3N_4 AFM cantilevers (model MSCT-AUHW; Veeco Instruments) with a spring constants of 0.02 N/m and ultrasharp tips with radii < 20 nm were used to image and measure the force response of the brush through force-distance curves. The spring constants of the cantilevers were determined by means of the thermal noise method [72]. Imaging was first performed in dry state

with large scan areas (60 or 40 μm^2) to localize fringes and surface defects as height references for the subsequent characterization of the brush.

Thereafter regions of interests were selected and imaged in dry state in contact mode. Afterwards the sample was imaged in Millipore water, followed by NaCl solutions, respectively. Generally the order of incubation and imaging was Millipore water, 10 mM, 100 mM and finally 1000 mM NaCl. Imaging in liquids was performed as a rule in contact mode except for image5.4, which was recorded in tapping mode. Contact mode imaging was preferred, because in tapping mode it was difficult to quantify the imaging force, and stable imaging in tapping mode required larger forces compared with contact mode imaging. The applied normal loading forces exerted by the AFM tip onto the brush were varied changing the set point value of the piezo. The scan rate was between 2 - 10 µm/sec.

Indentation experiments on the brushes were performed with the ultrasharp Silicon Nitride tip as well as with a 8 µm Silica colloid from microparticles GmbH, Berlin. The Silica colloid was glued at the end of a tipless cantilever with UHU PlusEndfest 300 2-komponenten Epoxidharz. The spring constant did not noticeably change after attachment of the colloid.

5.2 Results

5.2.1 Imaging of highly charged PSPM brushes

The interface of a polyelectrolyte brush in good solvent conditions represents a diffuse dynamic interface. The thickness of the brush is an important property. It has been previously measured for various types of brushes [157-160]. The brush thickness is commonly used to characterize structural changes of the brush occurring as a function of ionic strength, pH and temperature. The pronounced sensitivity of the brush toward external stimuli, which is the basis of its responsiveness, may yield different estimations of its thickness depending on the

employed experimental technique. Exposure to increasing ionic strength conditions may trigger conformational molecular changes, which will result in a well pronounced reduction of the average thickness. Such a sudden thickness decrease is called collapse. During brush collapse water is release from the brush interior. The rigidity of the brush increases correspondingly. Therefore measurements of brush thickness are important for understanding the mechanical and structural response of a brush as a function of external conditions.

For polymer brushes continuous in the lateral dimension measuring their thickness by means of AFM is, however, not a straightforward task, because the “height “ of the substrate as a reference value is required. The “grafting from” technique normally yields entirely covered surfaces. The thickness of the brush is difficult to measure by means of AFM, because the bottom of the brush is not directly accessible to the tip. A solution to this problem would be to deliberately introduce reference surfaces, for example, by fabricating patterned brushes.

Such a patterning was obtained on the surface by synthesis brushes on stamped thiol initiators. Patterns were obtained, however, it was observed that repulsive force indicative for the presence of polymers were still present outside of the stamped regions. This observation suggested that initiator molecules could diffuse out of the stamped region, or that the width of the stamp was too narrow to overcome the repulsive effect of the surrounding brush layer.

Another attempt to produce a brush free region adjacent to a brush was made by immersing only a part of the available gold coated surface into the initiator solution. The region where the solution formed the meniscus on the surface was marked. Nonetheless, estimation of the brush thickness with this method was not possible either, because in this case the thickness of the brush decreased progressively along a comparatively large distance of about 50 μm over the region of immersion. The reference region was thus too far away from the undisturbed brush to ensure proper brush thickness measurements

Measuring the thickness of the PSPM brush became finally possible by means of intentionally removing parts of the brush layer through scratching. Relative height changes could also be quantified by taking advantage of defects in the surface that were sometimes present in the samples. A scratch generated by grasping the surface with a very fine needle, usually led to pronounced but irregular variations in depth along the scratched region. However, it was noticed that narrow parallel fringes accompanied scratched areas. Within these fringes of about 15 to 20 µm in width imaging was performed and the grainy features of the gold substrate were recognized. It was concluded that the resulting fringes were regions where the brush layer had been removed. Apparently, during the scratching process brush molecules in the vicinity of the scratch got entangled with the disruptive grasping mechanism of the needle and were removed. The scratch method, although unrefined, thus provided a means for a sufficiently accurate determination of the brush thickness, and also a reference surface for posterior measurements of force vs. distance curves.

Once a fringe based on the absence of a brush was identified, imaging of characteristic regions was performed with the *minimum loading force* (F_{ML}). The minimum loading force F_{ML} was defined as the smallest force, the AFM tip exerts onto the sample that still resulted in a stable positive cantilever deflection during

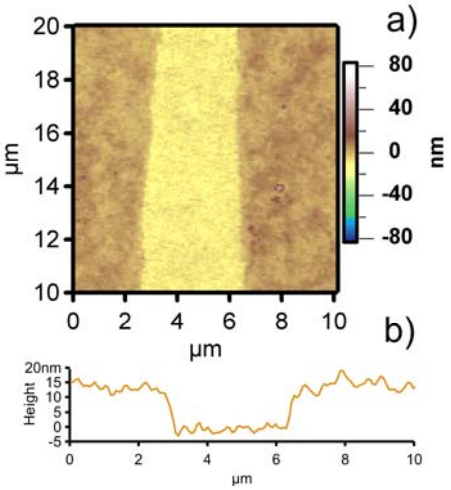

Figure 5.1 Contact mode image of PSPM brush in dry state.

imaging. Lower pushing forces than F_{ML} generated unstable states between tip and sample which finally led to disengagement of the tip from the surface and image distortion occurred. Imaging was first performed in dry state as shown in figure 5.1. A fringe, from which the brush was removed, can be seen. From the obtained

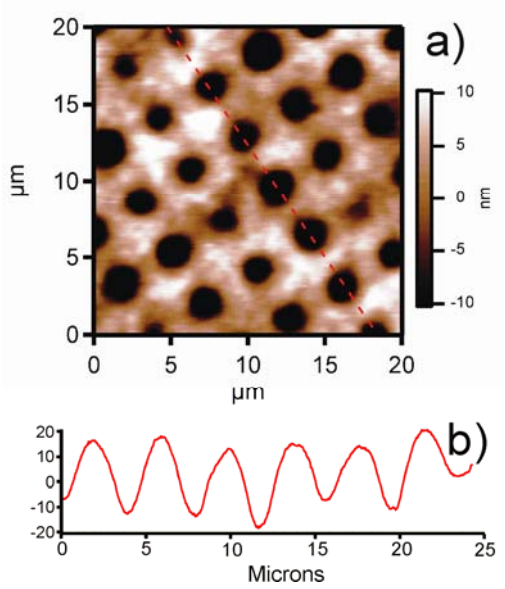

Figure 5.2 Contact mode image of patterned region solvated state in Millipore water. a) Surface topography. b) Cross sectional profile across red dashed line.

image the brush thickness (H_m) can be determined through a cross section profile as shown in figure 5.2. The brush thickness, H_m, is the distance from the average height of the gold substrate to the average height of the brush outside the fringe taken from several section profiles. In dry state the thickness of the brush was independent on the imaging loading force with an average value of 12.5 ± 1 nm.

The topography of a patterned brush is shown in figure 5.2. This image was obtained in Millipore water. The dark patches indicate the positions, where the initiator was initially absent. As mentioned before, although the pattern can be easily recognized, the true substrate surface was not accessible by the tip within the patches. This follows from the wavy height profile shown in Fig. 5.2b. Therefore, a height reference could not be established.

In Millipore water the brush is in a swollen state. The tethered polyelectrolyte chains may have different contour lengths. Together with the Brownian movement of the chains and their flexibility a diffuse interface with the bulk solution can be expected. Figure 5.3a and 5.3c show the topography and the profile of a homogeneous brush area obtained in Millipore water. Here, the lack of a reference zero line from the substrate makes the estimation of the brush thickness impossible. The high grafting density together with its softness and flexibility, does not allow discerning structural details on the surface. Figure 5.3b and 5.3d represent the same region of the brush and its profile, after exposure to 1 M NaCl solution. It can be seen that the surface shows a more structured and corrugated appearance. Fig. 5.3d provides the respective profile for the surface variations in height. The variations in height from the average value were 6.7 nm in Millipore water and 4.5 nm in 1 M NaCl.

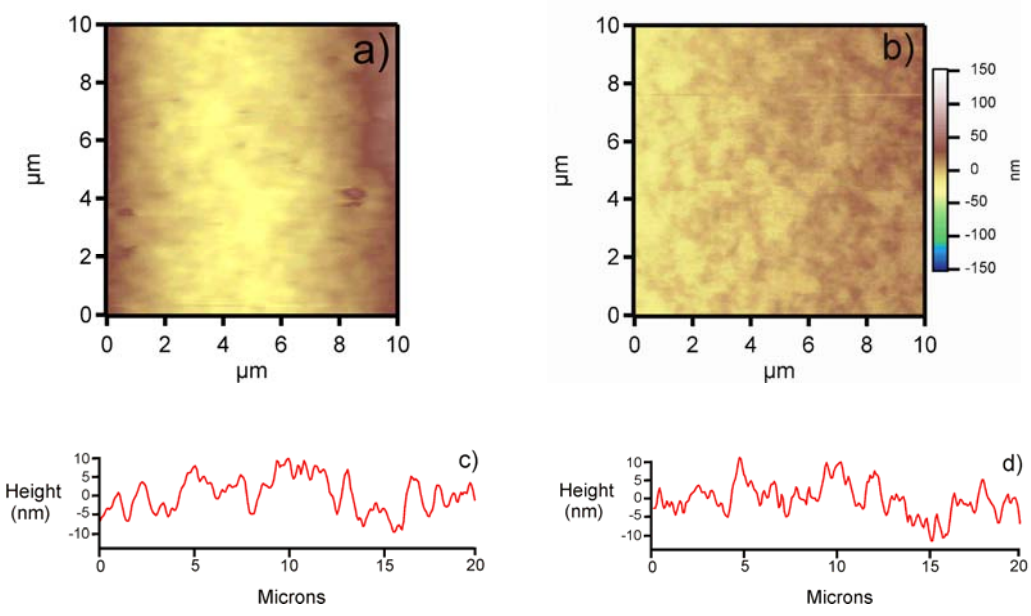

Figure 5.3 Topography of a PSPM brush. a) In Millipore water. b) Same region in 1 M NaCl. c) Section profile in Millipore water. d) Section profile in 1 M NaCl. The height scales shown in c and d, represent the height variations of the brush interface with respect to the average value of the cross section.

5.2.2 Loading force and dependence of the thickness of PSPM brush on salt concentration

To study the changes in brush thickness as a function of the loading force, either a region next to a fringe or a region containing a defect were selected. A defect of the surface in our understanding is a region, where the gold coating is not accessible by the thiol molecules. Therefore this particular area remained void of brush molecules. This can be unambiguously detected with AFM as the defect shows the typical features of a hard surface when probed with the AFM tip. Such a patch may have been formed as a result of a surface contamination. The contaminating substrate may have prevented gold deposition or the adsorption of thiols afterwards. Such contaminated patches appear as elevations with a specific relief. They may serve as convenient recognizable references for quantifying relative changes of the brush thickness in response to external stimuli.

Figure 5.4 displays an image of such a contamination together with the adjacent brush region. While imaging, the set point value was switched from F_{ML} to the highest possible loading force. It can be seen that the brush thickness changed drastically as a function of the loading force. Imaging with the minimum loading force revealed a brush, the thickness of which was comparable with that of the protruding contamination. However, the brush became notably flattened as a result of the sudden increase of the applied loading force as can be observed in comparison with the surface of the contamination. The decrease in measured thickness was more than 100 nm. This pronounced drop in brush thickness can be easily appreciated between regions A and B in comparison with the constant height of the solid contamination.

There was also a small brush free space next to the protruding brush. This area is indicated by an arrow in Fig. 5.4b displaying cross sections profiles. Assuming that the level of this area is close to the surface of the gold, one may estimate a brush thickness H_m of 170 nm when using the minimal loading force in tapping mode.

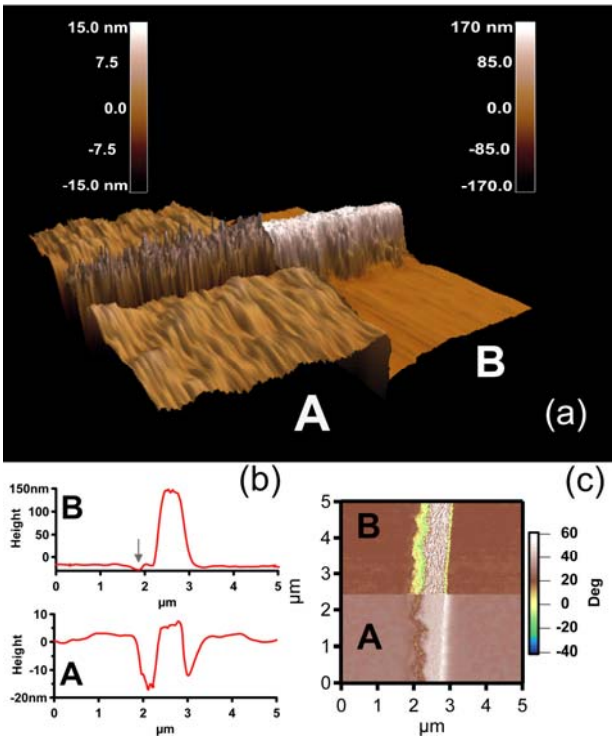

Figure 5.4 PSPM brush surface at different loading forces using tapping mode. a) AFM 3D image of PSPM brush with a defect as a reference half of the area was scanned at the minimum loading force (region A), while the remaining part was imaged with the maximum loading force (B). The transition from A to B represents a change in the set point value from 30 mV to 600 mV. The colored scales in each region offer a color coded perspective of the height of the structures. Note the different resolution in region A and B. b) Cross sectional profiles through the defect for each corresponding region. The arrow in B indicates a probably brush free gap. c) Phase image for the same region.

For the region B the measured thickness was slightly above the value for the brush in dry state, which in this case was about 15 nm.

The dependence of the measured brush thickness on loading force was investigated in more detail. Regions with fringes were selected and imaged in contact mode. Contact mode was used, because in this mode the loading force is well defined. One and the same region was repeatedly imaged at increasing loading forces, using the set point value given to the piezo-crystal as a control parameter for the normal compression applied by the tip to the surface. In such a

way it became possible to observe the change in brush thickness as a function of the loading force during imaging. After the region was repeatedly scanned for the chosen set of loading forces, the ionic strength of the solution was increased by addition of salt and the imaging process was repeated. The applied loading forces were F_{ML} (30 - 130 pN), 0.36, 1.43, 3.6 and 5.72 nN. The investigated environmental conditions were Millipore water, 10, 100, and 1000 mM NaCl solution, respectively.

A height image with the fringe in the middle as a reference is shown in figure 5.5, which was imaged in Millipore water. The scanned region is the same as the one shown in figure 5.1, which was obtained in dry state. The contrast between these two images is remarkable as can be appreciated in the color coded height scales. In water the brush swells and increases its thickness from 12.5 nm measured in the dry state to 140-150 nm when hydrated.

This corresponds to a twelfth-fold increase in measured thickness. The two bottom graphs in Fig. 5.5 display the changes in measured thickness as a function of the loading force in Millipore water and 100 mM NaCl, respectively. A well pronounced gradual decrease in the measured thickness is observed for increasing imaging loading forces.

In Millipore water the brush is more compressible than in salt solution. This can be inferred from the observed dependencies of the brush thicknesss on the loading forces [158]. Furthermore, in 100 mM NaCl the contour profiles show a higher roughness as those in Millipore water. In figure 5.6 the PSPM brush is imaged in Millipore water using the minimum loading force, F_{ML}, and thereafter the highest applied load of 5.7 nN.

For comparison the colour coded height scales are the same. It is evident that an increase of the imaging loading force strongly decreased the measured brush thickness.

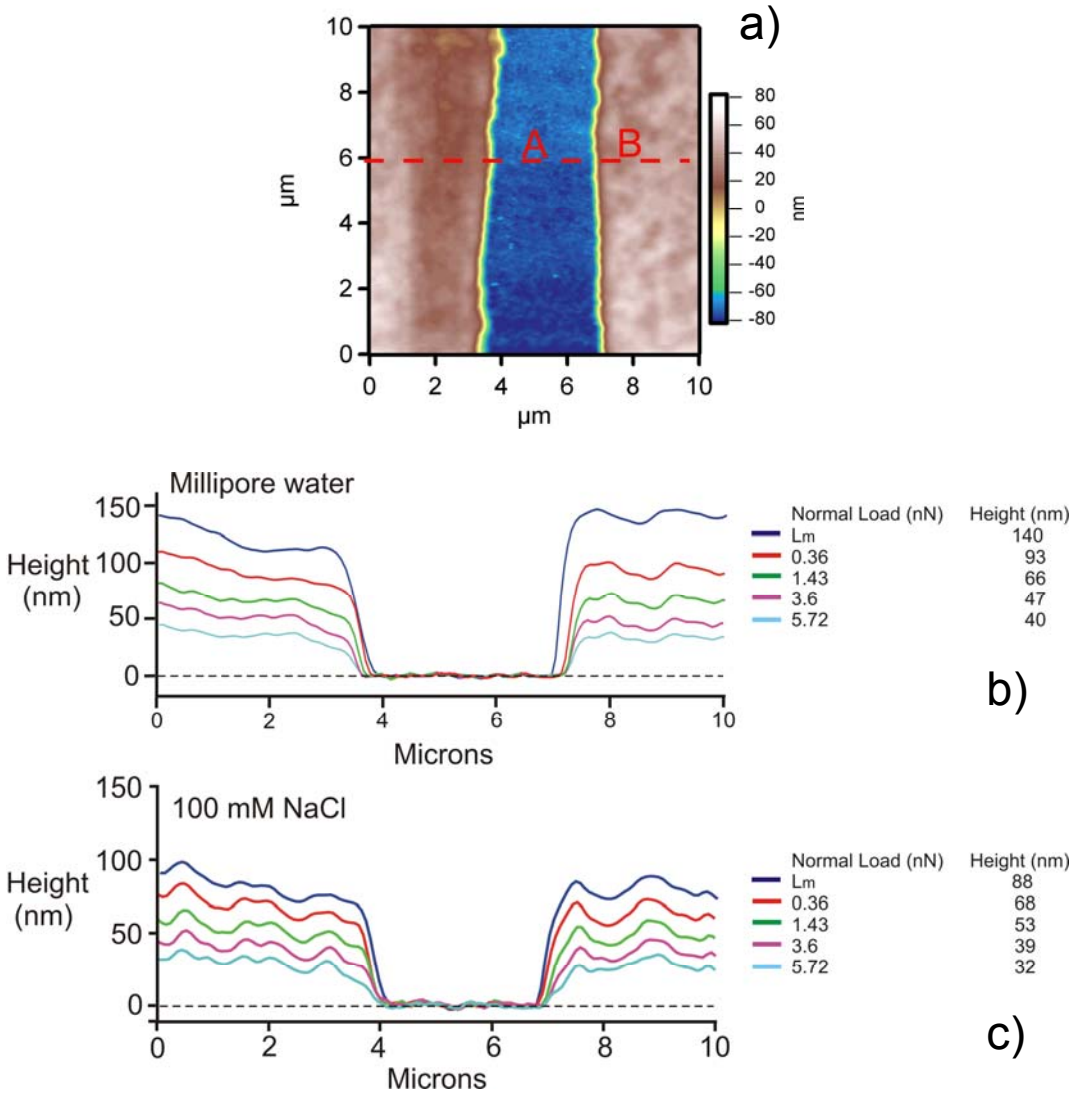

Figure 5.5 Imaging of a PSPM brush in contact mode at increasing loading forces. Top: Height image in Millipore water with F_{ML}. The fringe appears in the middle as a reference and the dashed red line indicates the cross section measurement. Bottom: Cross section profiles as a function of the imaging loading force in Millipore water and in 100 mM NaCl.

These results demonstrate that the brush itself is a quite sensitive material, where the measured thicknesses strongly depend on the imaging protocol itself. For this particular reason the measured brush thickness does not represent the “true” thickness of the brush, as it is impossible to image a brush without applying a force.

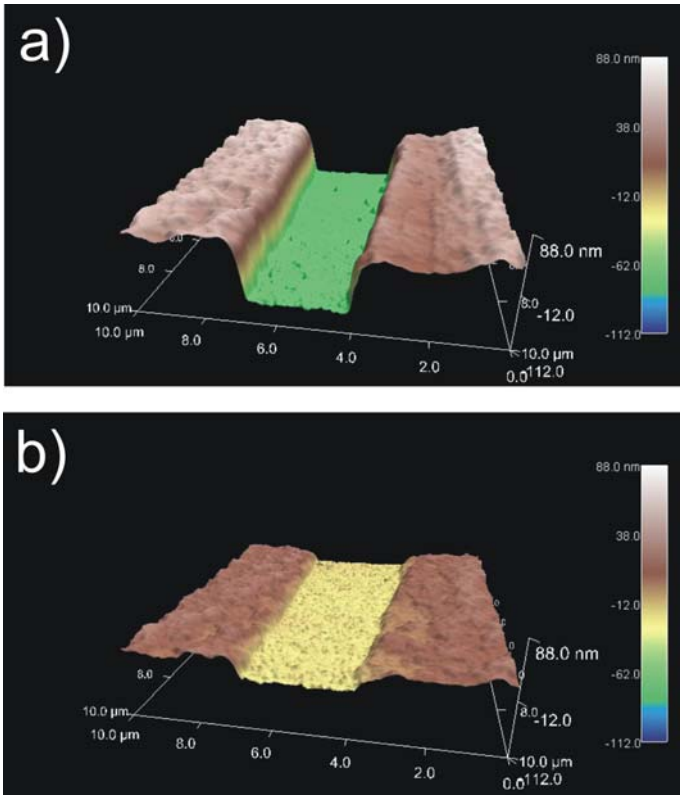

Figure 5.6 3D contact mode images of PSPM brush response to imaging loading forces with the AFM tip in Millipore water. Both regions are the same region presented in figure 5.2.4a) and are shown with the same z-scale for comparison. a) Using minimal loading force. b) Using 5.7 nN loading force.

The brush thickness may be defined as the thickness which would be obtained in the hypothetical case of zero imaging force. As will be shown further below, the size and shape of the utilized AFM probe is another important factor, affecting the determination of the brush thickness.

Figure 5.6 displays the dependence of the measured brush thickness on salt concentration. Image 5.7a was obtained in water with F_{ML}, while 5.7b was taken in 1 M NaCl compressing with the maximum load of 5.72 nN. It is obvious that for high salt concentrations the tip compresses the brush up to a point where the tip almost reaches the substrate as it approaches to a distance of about 14 nm which is rather close to the measured brush thickness in dry state of 12.5 nm. The cross section profiles in Fig. 5.7 show a well pronounced dependence of the measured

brush thickness on ionic strength. With increasing ionic strength the brush thickness decreases. Quite interestingly, as shown in figure 5.7c the swelling into the z-direction from dry state to hydrated condition is also accompanied by a lateral expansion of the brush.

During the scanning process, it was noticed that stable imaging in Millipore water required a typical minimal loading force F_{ML} of about 100 - 130 pN. For higher ionic strengths loading forces below 100 pN, or even slightly negative values of the latter were sufficient. This suggests that at high ionic strengths the interaction of the molecules with the tip becomes attractive.

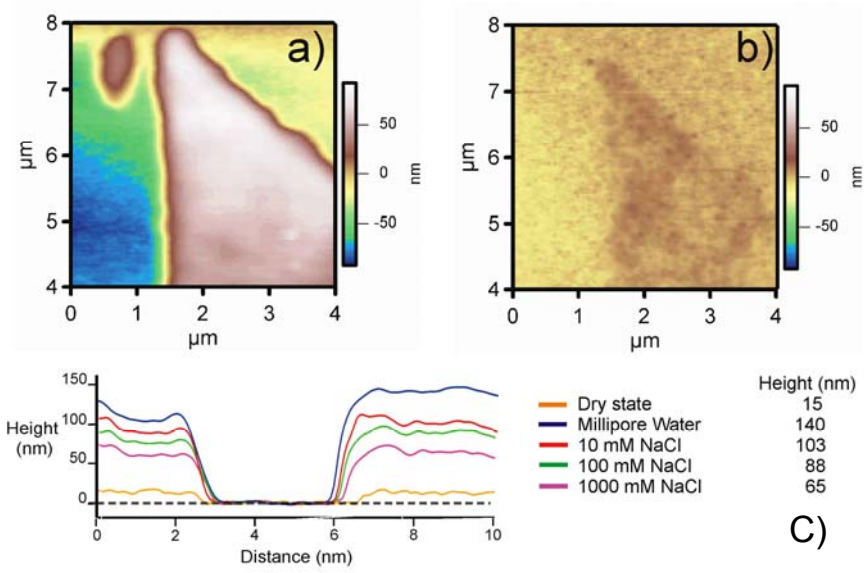

Figure 5.7 Compression of PSPM brush by AFM tip under different conditions. a) Image using the minimum loading force Millipore water. b) Same region after exposure to 1M NaCl and applying a maximal loading force of about 5.7 nN. c) Measured thickness using F_{ML} as a function of ionic strength. The cross section profile for the brush in dry state has been included for comparison.

The transformation of the brush into more dense layers upon increasing ionic strengths was a reversible process. 90 % of the original brush thickness was recovered after rinsing repeatedly in Millipore water. Incubation of about one hour

by immersion into Millipore water was required for full swelling to the initial thickness. It is interesting to note that the thickness decrease in 1 M NaCl was not as effective concerning brush thickness as applying the highest loading force.

AFM tip vs Colloid

The previous findings suggest, as expected, that PSPM brushes are comparatively loose structures, at least in their extended states. Otherwise the observed changes in thickness would not be possible. Furthermore, there may be a distribution of chain length, because this parameter cannot be fully controlled during polymerization. There may be a small number of rather long chains stretching out into the solution. Therefore, instead of a well-defined interface the boundary between the brush and the solution may be formed by region where the monomer density gradually decreases to zero. Furthermore, the thermal motion of chains in the outermost region of the brush has to be kept in mind as well. When imaging such an interface, a sharp AFM tip may partly interdigitate between the brush polymers [161]. Therefore, imaging the surface of the PSPM brush with differently AFM probes of different cross section may produce additional information on the brush extension and the structure of the outermost brush region [162]. We have accordingly used an 8 μm silica colloid glued to a tipless cantilever for imaging (and as presented below also for force - distance measurements).

Fig. 5.8 proves that the measured brush thickness depended on the probe size. When measured with the colloid the brush thickness was at least about 30 nm larger in Millipore water than when measured with a sharp tip. Control force – separation curves taken within the fringe with the AFM tip and the 8 μm colloid shows that the colloidal probe experiences a significant repulsion in 1 M NaCl. As shown in figure 5.8b, the control curve observes a long range repulsive behavior

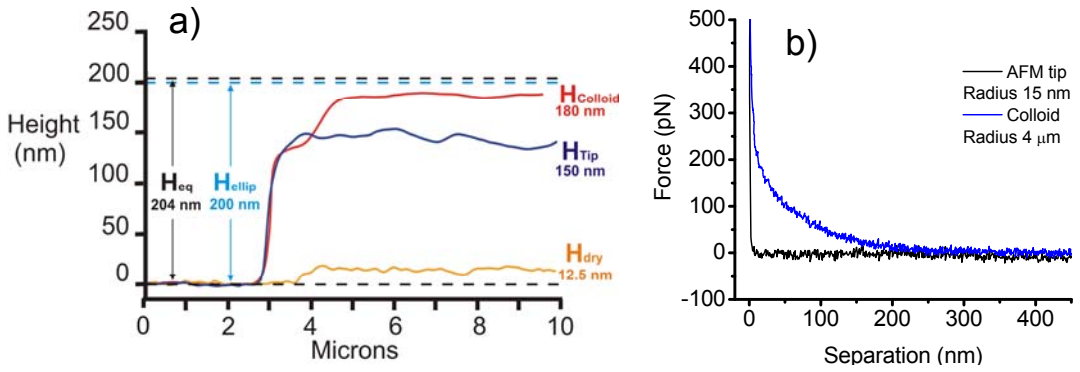

Figure 5.8 Left: Comparison of measured thickness of a PSPM brush in water with an AFM tip of tip radius ~15 nm and a colloid of 4 μm in radius using F_{ML}. The dashed horizontal lines show the calculated equilibrium brush thickness H_{eq} obtained from the H_{dry} (see below) and the brush thickness obtained from null ellipsometry measurements. Right: Force vs distance curves in the brush free area obtained with the tip and the colloid, respectively.

of about 220 nm before full compliance was attained. This repulsion has to be steric repulsion, as electrostatic forces should have a characteristic decay length below 1 nm in 1 M NaCl.

Therefore it remains uncertain if the colloid has contacted the substrate or whether some brush molecules remain compressed between the colloid and the substrate. It may be thus concluded that the thickness measured with the colloid may underestimate the real brush thickness. A probe with a larger cross section is more sensitive to steric interactions at larger distances caused by a small number of polymers present in the gap, as it causes compression of the polymers in-between instead of interdigitation of the tip between the brush molecules.

When a step like brush edge is imaged with a spherical probe there should be a well pronounced convolution. Straightforward geometric considerations taking into account a brush thickness of 200 nm and a radius of 4 μm show that instead of a sharp step a more gradual increase distributed over a lateral distance of about 1.2 μm should be observed. The rate in height increase would be steepest when the colloid starts to feel the step. The profile in Fig. 5.8a is consistent with the expected

convolution behavior, especially if taking into account that the edge of the brush is not a stiff structure but can be bent easily.

A larger imaging probe is more sensitive to interactions caused by a small number of longer molecules forming a loose outer corona. Some long chains may indeed have been synthesized during the ATRP process. It is likely that once engaged, the sharp AFM tip would be unable to “feel” the steric repulsive influence of these long chains if their mean distance is of the order of the tip radius or larger.

The measured thickness of the brush for a particular environmental condition is thus a balance between the grafting density σ of the brush, the contact area of the AFM probe, and the applied force by the piezo.

The response of the brush may also depend on the mode of interaction of the AFM tip with the brush. For instance, when imaging in contact mode shear forces become important, because the tip may subside into the brush. Tapping mode imaging may have a milder impact since the tip rapidly oscillates normal to the surface reducing thus the impact of shear forces. Shear forces are not relevant either when nanoindentation or force distance measurements are performed or a force – volume curve is obtained.

5.2.3 Discussion

Estimation of the brush thickness from dry state measurements

Let us now compare the measured brush thickness obtained from imaging with theoretical estimates based on molar volume considerations and grafting density. The surface density of monomers can be obtained as follows. Let us assume that the brush in dry state represents a dense structure. A PSPM monomer consists of 5O + 1S + 7C + 11H atoms and K^+ as the counterion. This results approximately in a monomer volume of V_{mon} = 0.064 nm^3. With a brush thickness of 12.5 nm in dry state we arrive at a monomers surface density of about 195 monomers/nm^2.

With the “grafting from” technique grafting densities within the range 0.7 - 0.8 chains/nm^2 have been reported [155]. A grafting density of 0.8 chains/nm² then results in 244 monomers per PSPM polymer on average. For a fully stretched brush we would then have a mean thickness 204.6 nm with a length per PSPM monomer of l_{mon} = 0.838 nm. This estimate of the mean brush thickness in a full stretched state coincides rather well with the brush thickness measured by ellipsometry in Millipore water, where a value of about 200 nm was obtained. Furthermore, in the fully stretched state the water content of the brush amounts to (204.6-12.5)*100/204.6 ≈ 94%.

Figure 5.9 summarizes the experimental data points for the measured brush thickness H_m plotted as a function of the applied loading force for increasing salt concentrations. The measured thickness of the brush decreased with increasing load in a strongly nonlinear manner. The dashed lines represent the brush thickness measured in dry state (12.5 nm) and the equilibrium thickness of the brush determined by null ellipsometry (200 nm), respectively. The observed nonlinear thickness response of the brush upon applied external forces during imaging is inconsistent with a brush model formed by elastic springs. For such a system a Hookean behavior would be expected where the induced deformation is proportional to the applied loading force. Furthermore, the deformation of the brush upon mechanical compression was reversible. The thickness response upon a sudden change of the loading force, occurred instantaneously compared with the imaging rate. These observations are consistent with a thermodynamical behavior in the sense, that. The thickness vs. loading force curves resembles volume – pressure isotherms of a gas rather than compression curves of an elastic material in the Hookean range. There seems to be, furthermore, a limiting minimal brush thickness provided by the finite volume of the brush polymers. This feature is similar to Van der Waals gas, which assumes a finite volume if the pressure tends to infinity. A property different from a gas is that at zero or even negative loading forces the thickness of the brush stays finite, which is obviously a consequence of the connectivity of the polymers and their covalent attachment to the substrate.

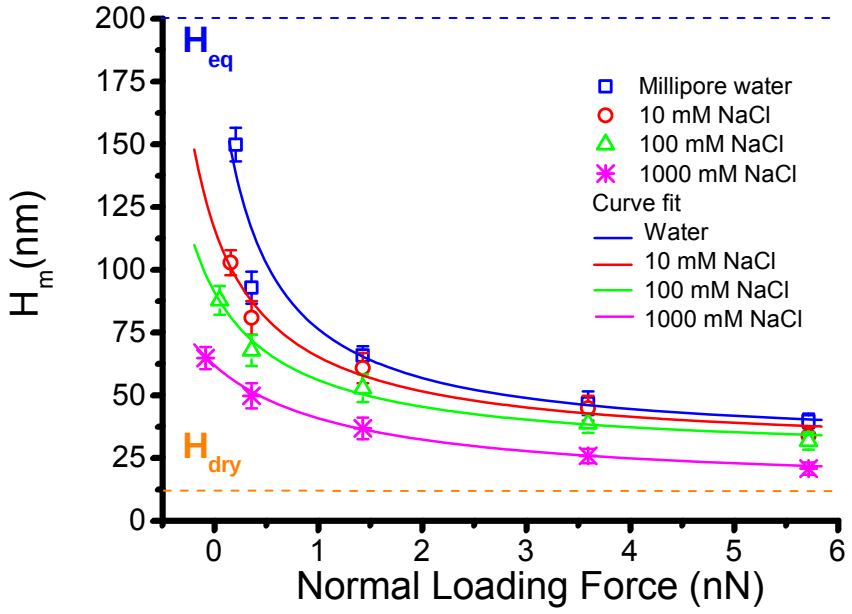

Figure 5.9 Plots of brush thickness as a function of the loading force during imaging with salt concentration as a parameter.

This lead to the idea to model the behavior of the highly charged polyelectrolyte brush with an equation of state for compressible fluids.

The equation of state of a compressible fluid is

$$(p+a)\cdot(V-V_0)=c\cdot T \qquad (1)$$

p, V, and T are pressure, volume and absolute temperature, respectively. a can be interpreted as the cohesive pressure, which in a first approximation does not depend on volume. V_0 represents the finite volume achieved at infinite pressure, and c is a constant proportional to the number of “molecules” in the system and their interaction energy. For the situation of a brush imaged with an AFM we may formally use the force instead of pressure and, correspondingly, the thickness of the brush instead of volume. In analogy to the Van der Waals gas a can be

$$(f+a)\cdot(h-h_0)=c'\cdot T \qquad (2)$$

interpreted as a cohesive force. There is though an alternative physical interpretation for the parameter a. It can be understood as a measure of the density gradient in a brush. This interpretation is quantitatively justified further below. h_0 is the brush thickness at infinite compression, and c´ is a constant characterizing the energy and number of the brush molecules interacting with the tip. Rearranging equation 2 and adding to the cohesive force the well-known worm-like chain (WLC) equation for chain extension, we arrive at the suggested equation of state:

k is Boltzmann's constant. nkt stands for the energy of brush molecules interacting

$$h(f,T) = \frac{n \cdot k \cdot T}{f + a + \frac{m \cdot k \cdot T}{4 \cdot P}\left(1 - \frac{h(f,T)}{L}\right)^{-2}} + h_0 \qquad (3)$$

with the tip. This term also includes an electrostatic contribution, because, for example, a decrease of the ionic strength would increase the energy of the brush molecules. P is the persistence length, and m is the number of polymers interacting with the tip. L is the contour length of the polymer. The explicit introduction of the WLC force into the cohesive force ensures that the brush thickness stays finite if the loading forces become zero or even negative. The WLC force becomes only significant if the brush state is close to fully stretched. This is the case if the brush thickness is close to the contour length L. In most cases the WLC term can be neglected.

The experimental data in Fig. 5.9 were fitted with Eq.3 according to the method of weighted least squares. Parameters were n, a, and h_0. The WLC term had no influence as the measured brush thicknesses were obviously sufficiently far from the fully stretched state. From the plot in Fig. 5.9 it can be appreciated that the obtained empirical equation (3) describes fairly well the data within the experimental errors. On the basis of the best fit one can calculate the equilibrium

Fitting Parameters	n	*a* ()	h_o (nm)	H_{eq} (nm)
Millipore water	$1.5x10^4$	0.39	29	193
10 mM NaCl	$1.5x10^4$	0.74	27	115
100 mM NaCl	$1.3x10^4$	0.87	25	90
1000 mM NaCl	$1.6x10^4$	1.34	12	61

Table 3 Fitting parameters for the proposed brush equation of state (3) according to the best fits shown in 5.9.

thickness H_{eq} corresponding to zero loading force. Table 3 provides the parameters obtained from fitting together with H_{eq}. The obtained parameters need to be interpreted considering the behavior of a highly charged brush in salt solution of different concentrations. First of all the parameter n is surprisingly almost independent on ionic strength. One would have expected that n, which is a measure of the energy of the brush molecules should increase with decreasing ionic strength. This is, however, not the case. Instead, we observe a well pronounce increase of the parameter a, with increasing ionic strength. On one hand, the parameter a may reflect the connectivity of the individual polymers and their attractive interaction among themselves reducing the repulsive interaction with the tip. There may be also an entropic contribution to a caused by the tendency of the brush polymers to assume a conformation with higher entropy. This would be consistent with a higher monomer density and a reduced brush thickness, correspondingly. Electrostatic repulsion between brush molecules acts into the opposite direction leading to a decrease of the cohesive force a, with decreasing ionic strength. The calculated values of a provided in Table 3 are in line with such an interpretation. On the other hand, a may describe the effect of the brush density being a function of the distance from the substrate. This will be

discussed more deeply in connection with the interpretation of force distance curves. In this context the derived dependence of a on the salt concentration can be simply attributed to imaging at different depth with the brush.

h_0 decreases systematically with increasing ionic strength becoming close to the thickness in the dry state at 1 M NaCl. Obviously, electrostatic repulsion contributes to h_0 at small length scales. This can be understood as the strong nonlinearly increasing electric field around charged monomers prevents close mutual approach and thus increases the apparent volume of the monomers. Only if the electrostatic interaction is switched off by a high concentration of counterions, can the brush be compressed to almost its dry state thickness. The transition between the states of the brush in 100 mM NaCl to 1 M NaCl can thus be considered as a collapse, while the changes from Millipore water to 100 mM NaCl appear as gradual changes.

A specific advantage of the proposed model is that it allows to derive the equilibrium thickness of the brush, H_{eq}, which is a parameter characterizing the brush independent on the employed loading forces. As should be, H_{eq} increases gradually with decreasing ionic strength.

This behavior will be compared below with the brush response measured in indentation experiments, when the brush is compressed toward the substrate by the approaching tip.

5.2.3 Indentation of PSPM brushes

The thickness, mechanical and electrical properties of polyelectrolyte brushes can be explored with indentation experiments [159]. In such experiments the AFM probe is moved with a given rate toward the brush and the deflection of the cantilever is recorded. Force versus separation curves are obtained from the measured deflections taking into account the spring constant of the cantilever. Fig. 5.10 illustrates the approach. Two different sizes of the indentor have been used.

In a) an ultra-sharp AFM tip with an apex radius of about 15 nm and in b) a silica colloid of 4 µm radiuses were employed to study the brush indentation behavior at different length scales corresponding to the molecular scale (a) and the brush as a whole (b) [163, 164].

If the diameter of the indentor is comparable with the spacing of the polyelectrolyte molecules, penetration of the indentor into the brush can be expected. This is illustrated in Fig. 5.10a. On the contrary, if the radius of the indentor is much larger than the intermolecular separation, the brush will be compressed homogeneously as shown in Fig. 5.10b.

An intrinsic experimental difficulty of indentation experiments is to measure the true distance of the tip from the substrate. As already outlined in the previous section, an area apparently void of brush molecules was used to obtain a reference value for the distance between the AFM tip and the substrate. With the sharp tip the characteristic surface structure of the substrate can be felt within areas void of brush molecules. Moreover, the characteristic features of a hard surface are observed. However, approach curves with the comparatively large colloid do not show the characteristic features of a hard surface as shown in Fig. 5.8.

It can be seen that repulsion starts approximately 200 nm before the steep rise in force. This point of steep rise in force was taken as the reference value for the level of the substrate. It cannot be excluded that a small number of polymers, which are not sensed by the tip, prevented the colloidal tip from direct contact with the substrate. Therefore, the force versus distance curves obtained with the colloidal probe can be only regarded as relative as far as the absolute distance from the substrate is concerned.

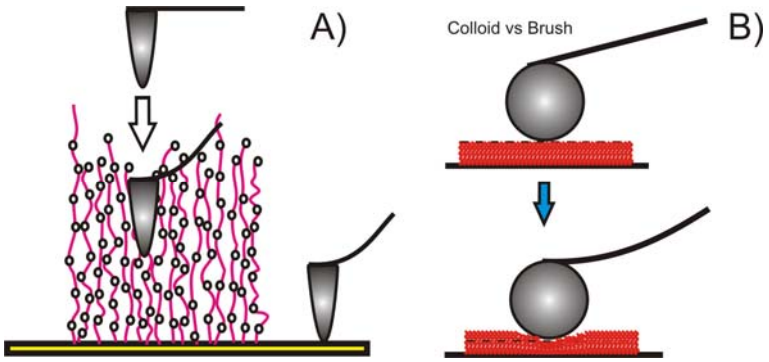

Figure 5.10 Schematic representations of the experimental approaches to probe the range of interactions on the PSPM brush by AFM indentations. a) With a sharp AFM tip of radius about 15 nm. b) Compression of the PSPM brush with a silica colloid (4μm in radius) attached to a tipless cantilever.

In the previous chapter the brush thickness obtained from imaging was described with an empirical model of a compressible liquid, see Eq. 2. For the sake of consistency the same approach will be followed for the analysis of force versus distance curves obtained by indentation experiments. This strategy is not only consistent with the presented analysis of the imaging data; it is also justified by the general nature of the indentation curves.

Figs. 5.11 a) and b) display the experimentally measured approach curves for the employed ionic strengths both for the ultra-sharp tip and the colloidal probe. Indentations were performed in the same region as used for imaging. The specific region is shown in figure 5.5. The retraction curves superimposed faithfully onto the approach curves upon withdraw without any signs of hysteresis or adhesion peaks even after repetitive indentations. Therefore the retraction curves are not provided.

All force curves show a similar behavior. The force versus separation curves, show a steep rise in repulsion at larger indentation depths, together with the tendency of slowly approaching zero at larger distances from the substrate.

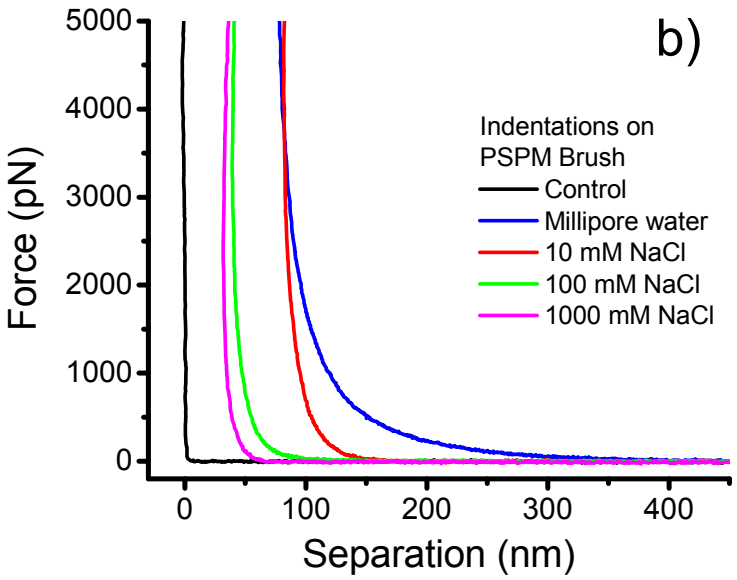

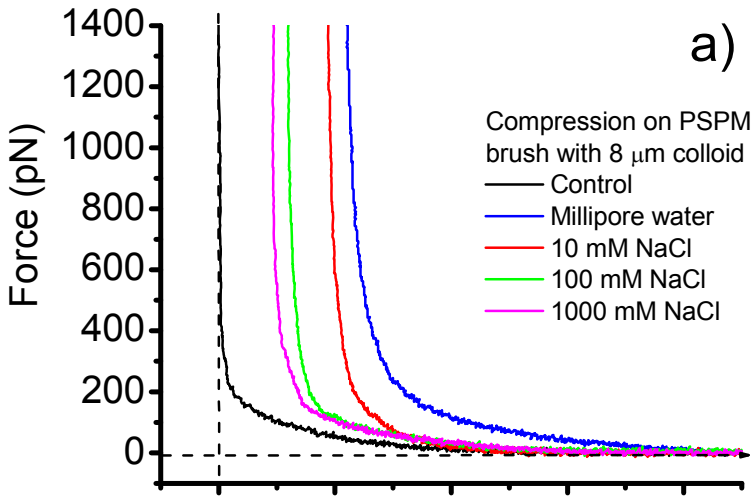

Figure 5.11 Force-separation curves measured with an AFM tip (a) or an 8 μm in diameter silica colloidal probe on PSPM brushes (b). The brush thicknesses at zero force derived from imaging are provided for comparison.

These two features are consistent with the proposed equation of state, see Eq. 2 in the previous chapter.

Obviously, the model of a compressible liquid though can only be applied when the tip is close to the brush or is even indenting the brush. As the AFM tip is approaching towards the surface, repulsion begins at distances well beyond the equilibrium thickness obtained in the imaging experiments. At these larger distances, the character of the interaction force must be different from the proposed model, because, for example, long-range electrostatic forces should decay exponentially. There may be also a diluted corona of brush polymers the density of which may change significantly with the approach distance. In this case the recorded interaction force will be in a first approximation proportional to the corona density and not represent compression of the brush. Such a feature and the expected exponential decay of electrostatic forces with distance cannot be, in principle, described with the simple model of a compressible liquid. Therefore, the small forces recorded at larger distances were described with an exponentially decaying function. We will come back to this further below.

Fig. 5.12 (sharp tip) and Fig. 5.13 (colloidal probe) display the experimental indentation curves on approach together with the best fits according to

$$f(h) = \frac{n \cdot k \cdot T}{h - h_0} - a \qquad (4)$$

In the case of the sharp tip data and the respective fits are displayed only for distances closer than or equal to the equilibrium height obtained from imaging. At larger distances the data decayed exponentially to zero. In the case of the colloidal probe a distance of 200 nm was chosen independent on the salt concentration to separate the region of brush compression from the exponential decay region.

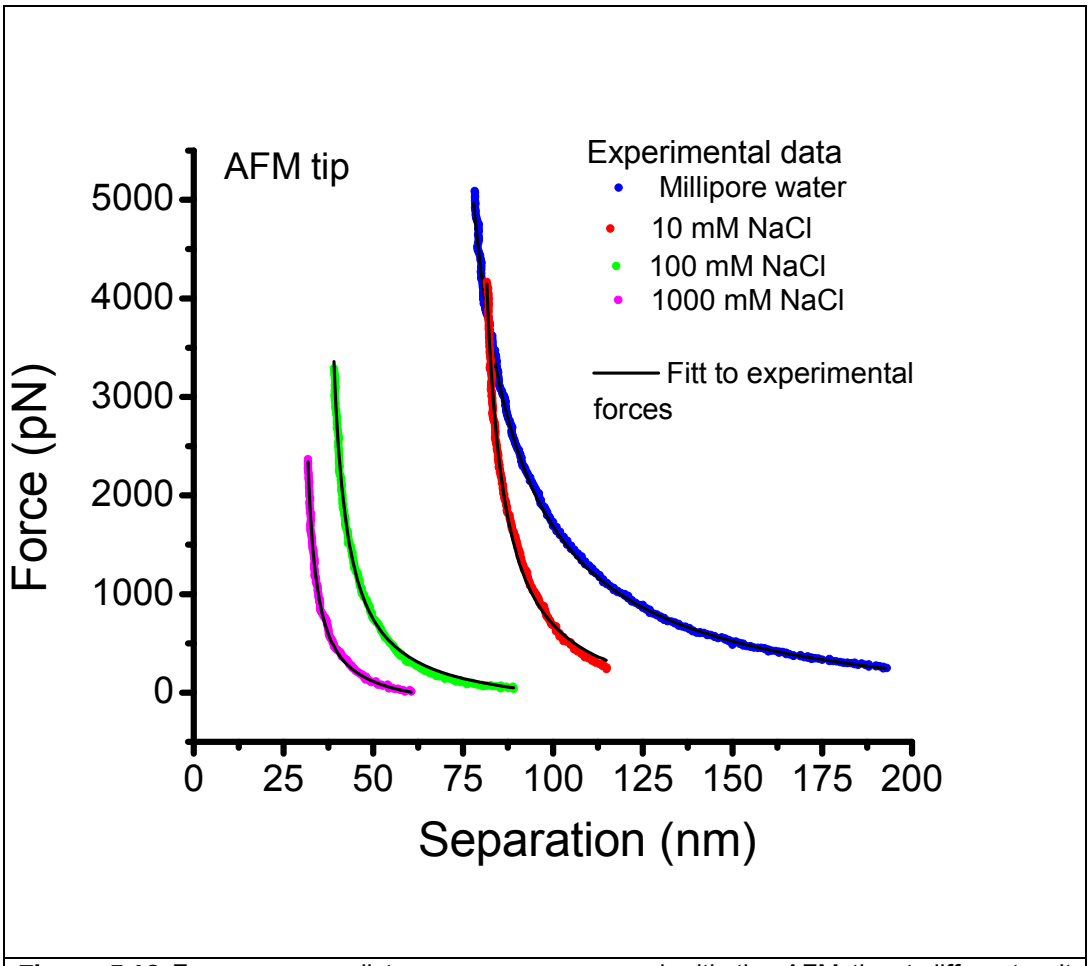

Figure 5.12 Forces versus distance curves measured with the AFM tip at different salt concentrations. The solid black lines represent the least square fits of the experimental data to Eq. 2. The curves were fitted starting from the equilibrium thickness H_{eq} obtained in the previous section.

The analysis shows that Eq. 2 describes all experimental curves with an astonishing precision. It is difficult to spot a region where the theoretical curves deviate from the experimental data within the range of the experimental noise. This result is remarkable as Eq. 4 is simple and contains only 3 independent parameters, the parameter n accounting for the energy of interaction, the parameter h_0, describing the depth of maximal compression and the parameter a,

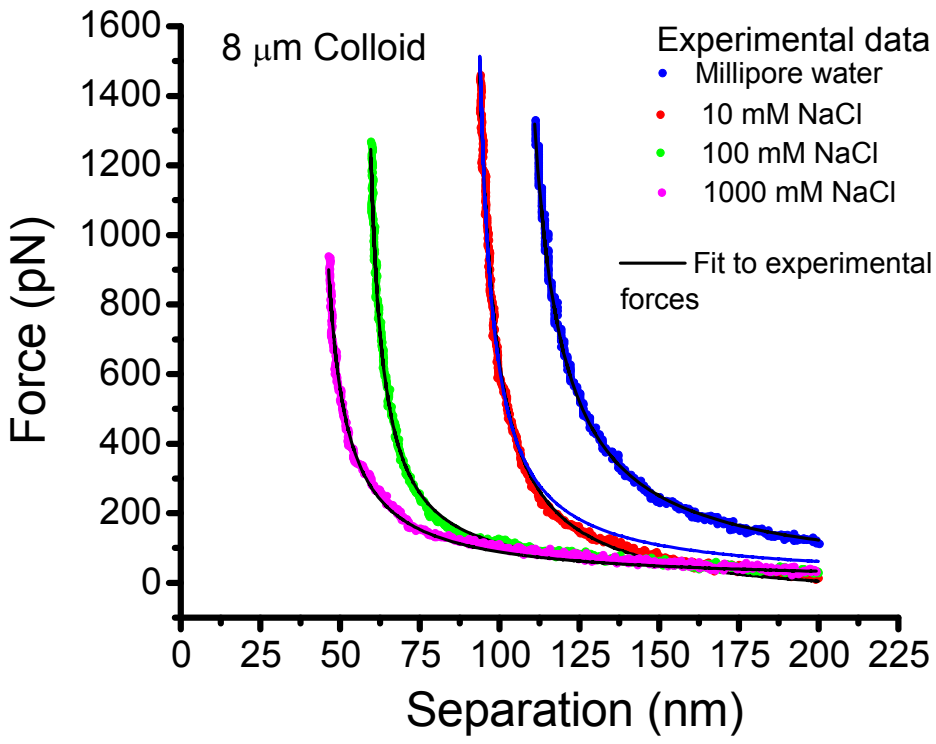

Figure 5.13 Forces versus distance curves measured with the colloidal probe at different salt concentrations. The solid black lines represent the least square fits of the experimental data to Eq. 2. The parameter a was set to zero. The blue curve represents the best fit for the case of 10 mM NaCl taking into account the parameter a.

which stands for a cohesive force or/and a distance dependent brush density in a linear approximation. In the case of the colloidal probe it was even not necessary to take the parameter a into account except for the case of 10 mM NaCl. That means for Millipore water, 100 mM NaCl and 1000 mM NaCl, respectively, the experimental data could be well described with the simplified equation

$$f(h) = \frac{n \cdot k \cdot T}{h - h_0} \qquad (5).$$

	Tip			Colloid		
C [mM]	a [nN]	h_0 [nm]	nkT 10^{-18}J	a [nN]	h_0 [nm]	nkT 10^{-18}J
0	0.31	64.8	12.0	-	101.9	70.8
10	0.25	76.7	7.8	0.07	88.7	22.1
100	0.22	35.1	5.0	-	55.5	14.5
1000	0.21	29.3	5.3	-	40.5	6.6

Table 4 Fitted parameters according to Eq. 4 for the case of indentation with a sharp tip and for indentation with a colloidal probe at 10 mM NaCl. Eq. 5 was used for the colloidal probe in Millipore water, 100, and 1000 mM NaCl, respectively.

Let us now analyze the indentation behavior in more detail. This can be conveniently done in a quantitative fashion on the basis of the fitted parameters. The parameters corresponding to the best least square fits are summarized in Table 4.

It is obvious that the tip and even more the colloid never reached the gold substrate as it follows from the calculated h_0 values. h_0 represents the brush thickness under infinite compression. As mentioned above in the case of the colloid h_0 can be considered only as a relative value, as the control measurements did not allow for an unambiguous determination of the level of the gold substrate. Nevertheless, the relative changes are quite useful for understanding the behavior of the polyelectrolyte brush under compression with a colloid, the dimensions of which exceeded the brush thickness considerably. In all cases, h_0 decreased with increasing salt concentration reaching less than 50 % of its value in Millipore water. This result can be interpreted as a consequence of the decreasing intrinsic repulsion between the charged groups of the polymer chain with increasing ionic

strength [165]. The electrostatic repulsion both within one chain and between groups located at different chains has a pronounced influence on the chain conformation and thus contributes to the maximum packing density which can be reached under high compression. In simpler words one could say that the electric field around the discrete charged groups is to some extent part of the molecular volume at least in the range of forces applicable with an AFM device. The parameter h_0 describing the (relative) thickness of the incompressible part of the polyelectrolyte brush has, in addition, a pronounced practical importance for the interpretation of brush indentation data. It can be considered as a reference value for quantifying the behavior of the compressible part of the brush. In this way uncertainties in the thickness measurements of brushes by means of AFM caused by methodological problems are reduced to an uncertainty of the thickness of the incompressible part of the brush.

The parameter n multiplied with kT can be considered as the energy intrinsically stored in the brush molecules interacting with the probe. It does not only contain the thermal energy but also the electrostatic energy. Decreasing the ionic strength should result in an increase of the energy per molecule, in other words decreasing ionic strength is in some sense equivalent to a temperature increase and vice versa. Table 4 shows indeed that nkT decreases with increasing ionic strength, and, furthermore increases with the size of the indentor. From this follows that the performed AFM indentation experiments directly sense the electrostatic behavior of the brush. An interesting aspect is that the dependence of nkT on ionic strength is much weaker for the tip than for the colloidal probe. This may indicate a different mode of interaction of the sharp tip with the brush compared with the interaction of the colloid.

Fig. 5.14 explores the dependence of nkT on ionic strength in more detail. It is known that in many cases electrostatic phenomena in electrolytes scale with the inverse of square root of the ionic strength or concentration if 1:1 electrolytes are concerned, $\sim c^{-0.5}$, which is proportional to the Debye length [166]. The double log

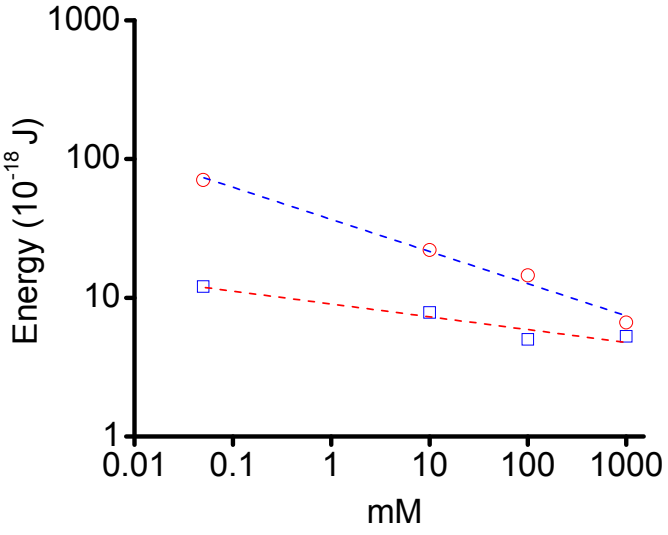

Figure 5.14 Log-Log plot for the energy as a function of the salt concentration.

plot of nkT against the concentration shows, however, that the dependence on ionic strength is weaker than follows from a Debye mechanism of electrostatic repulsion screening. In the case of the colloidal probe the empirical power law is $c^{-0.23}$. For the sharp tip we found $\sim c^{-0.09}$. One obvious reason for this weaker dependence is that the polyelectrolyte brush adjusts its structure according to the conditions of electrostatic repulsion. Upon decreasing ionic strengths the brush swells and thereby reduces its intrinsic electrostatic energy on the expense of decreasing entropy. This represents basically the response mechanism of polyelectrolyte brushes toward changes of the ionic strength of the environment. In the case of the sharp tip the exponent is significantly smaller than the exponent found for the colloidal probe.

This is an interesting finding, which can be also explained by the brush responsiveness itself. The comparatively narrow tip allows for a lateral readjustment of the brush polymers, which is not possible for the practically flat surface of the colloid if the curvature of the colloidal probe is compared with the brush thickness. Lateral adjustment means that the sharp tip penetrates the brush more than compressing it into the vertical direction.

In the section concerning imaging the parameter a, was interpreted as a cohesive force in analogy to the behavior of a Van der Waals liquid. There is an alternative and even simpler interpretation of this parameter a, which follows directly from Eq. 4. Let us assume that the density of the brush is not constant but a function of the distance from the surface. In this situation it can be expected that also the parameter n will be a function of the distance from the surface.

Expanding the function n(h) into a Taylor series at $h = h_0$ and neglecting terms of the order of 2 and higher it follows that

$$a = -\left.\frac{dn}{dh}\right|_{h=h_0} \cdot k \cdot T \qquad (6)$$

From this follows the alternative interpretation of a being parameter proportional to the density gradient of the brush as n beside its dependence on ionic strength should be also proportional to the density of the brush. From this follows that a should decrease with increasing salt concentration as it is indeed the case with the sharp tip. In general the parameter a is not a constant even within the framework of a first order Taylor approximation. This becomes obvious when the Taylor expansion is performed at distances larger than h_0. It has to be kept in mind however, that the force vs separation curves are sensitive to a only at larger separations, where the forces are small, because at separations closer to h_0 the first hyperbolic term in Eq. 4 becomes much larger than a. For the colloid, however, the simplified function (5) was sufficient to describe the experimental data. This can be understood as a consequence of the integrating character of an indentation measurement with a large colloidal probe. The colloid with its large radius is simultaneously indenting at all separations from the surface larger than the distance of the closest approach. This may be the reason that the parameter a was not necessary to describe the interaction of the colloid with the charged polyelectrolyte brush. This may be considered as evidence for relating the

empirical parameter a to the density change of the brush as a function of distance from the substrate rather than to a cohesive force.

The sharp AFM tip with an apex radius of about 15 nm and the 8 µm in diameter colloid represent rather different indentors concerning both size and shape. The size of the colloid is much larger than the thickness of the brush. The opposite holds for the sharp tip. Moreover, the shape of both indentors is different. The sharp tip represents a right circular cone with a spherical apex of about 15 nm in radius and an angle between the generatrix and the axis of 18°. Because of the large differences in shape and size the indentation data of the two different used indentors cannot be directly compared. The only possibility is to calculate from the experimental data the force per unit area acting on the indentor, f, according to Eq. 7:

$$F(z) = \oint_A (\vec{f} \cdot d\vec{A}) \qquad (7)$$

Here F is the measured force and A is the surface of the indentor experiencing interaction with the brush [160] . F(z) can be considered as a convolution of the function f(z´) with the surface of the indentor. Finding the unknown function f(z) is equivalent to solving the integral equation (7) which is essentially a deconvolution problem. It is clear from the structure of the problem (7) that the experimentally obtained F(z) dependence cannot be directly used to solve the problem (7), because F(z) needs to be sufficiently smooth, i. e. a continuously differentiable function of the distance z from the substrate. The experimental data have thus to be regularized. The fitted functions (4) and (5) can be used as proper regularizations of the experimental data as they describe the experiments very well, and, they are differentiable at any $h > h_0$. One problem, however, is that there is a cut off at $h = h_{eq}$ for the tip and at the selected h values for the case of the colloidal probe. The impact of the tail on the total force cannot be neglected as the area of the indentor grows with the depths of indentation which may partly compensate the decay of the force per unit area with increasing separation. We

therefore fitted the tail of F(h) with an exponential function of the type $F(z) = A \cdot \exp(-bz)$ with the additional constraint of being continuous with (4) and (5), respectively. Almost perfect fits were obtained in every case. These exponential functions were then used as regularized function for the tail region for subsequently solving numerically the problem (7). It has to be mentioned that the Derjaguin approximation is an analytical solution of the problem (7). It is not valid for a sharp tip, because it requires that the separation distance is much smaller than the length scale of the indentor. Even for the colloid the Derjaguin approximation would have limiting validity because the indentor radius is only about 10 times larger than the interaction distances.

C [mM]	Tip Decay length [nm]	Colloidal Probe Decay length [nm]
0	68.7	93.1
10	20.6	72.2
100	36.2	76.0
1000	-	83.3

Table 5 Decay lengths of fitted tails.

Table 5 shows the fitted decay length of the tail regions. It is evident that they are much larger than the corresponding Debye lengths. This disagreement reveals the nature of repulsion at larger distances. It can be concluded that the repulsion must be caused by a small number of polymer chains extending from the more dense part of the brush out into the bulk forming a corona in front of the actual brush. The observed decay length thus represents the decay of the density of the corona with distance from the substrate. The difference between the data obtained for the

colloidal probe compared with the tip reveals that the length scales are important. If the mean density between the corona forming polymers is less than the size of the indentor the corona cannot be sensed. This is probably the case for the 1 M NaCl solution when probed with the tip. In this particular case an exponential tail was practically absent. Under the same conditions the colloidal probe with its much larger surface “felt” the molecules within the corona.

Figure 5.15 displays the solution of the problem (7). Here the calculated forces per unit area are plotted against the distance from the incompressible part of the brush, $h-h_0$. This way of plotting removes uncertainties about the absolute distance from the substrate and, furthermore, reveals that the force per unit area f(z) scales as $\sim z^{-2}$. This follows from the identical slopes of all curves except the case of Millipore water when measured with the colloid. Here the comparatively large impact of the exponential tail modifies the power toward a negative exponent slightly greater than 2. The power law $\sim z^{-2}$ is of course expected as the function f(z) in principle has to be proportional to the derivative dF(z)/dz. F itself depends on z like z^{-1} according to (4) and (5). The scatter of the curves around maximum separation represents numerical artifacts and is caused by a discontinuity of the derivative of F(z) at the point of connection of the exponential tail with the hyperbolic functions (4) and (5).

The most striking message from Fig. 5.15 is that the calculated forces per unit area differ by about three orders of magnitude. It follows from the graph, that the sharp tip experiences apparently much higher forces per unit area than the colloidal probe at comparable distances. Since this is impossible, the conclusion is that approach distances for the two indentors differ considerably. From the graph follows that the difference is of the order of 100 nm, Shifting the curves for the colloidal probe by about 100 nm to the right one would obtain a continuation between the tip data and the colloidal probe data. This means that the recorded thicknesses at maximal compression are not the same for the brush and for the colloid. Two reasons may account for this difference. One obvious reason would be that the level of the substrate when determined with the colloidal probe was wrong

by about 100 nm when compared with the level measured with the sharp tip. The technical reason for this failure has been discussed above. Another point to be taken into consideration is that the tip may laterally displace the brush molecules upon indentation.

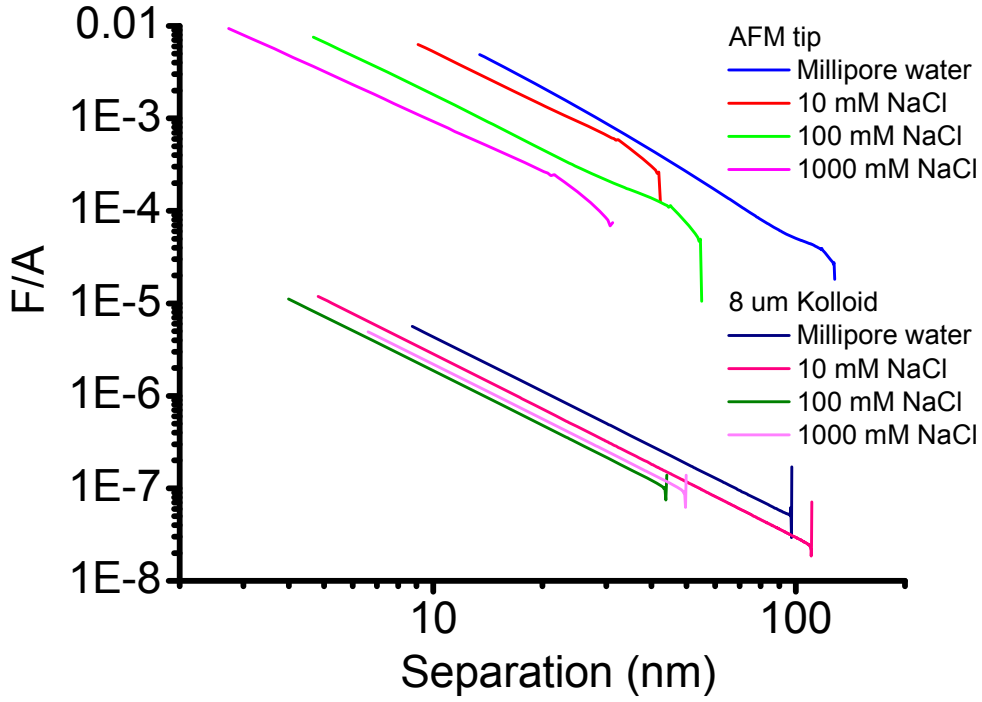

Fig. 5.15 Force per unit area as a function of relative separation ($h - h_0$) for the sharp tip and the colloidal probe.

This lateral freedom of movement of the brush polymers cannot take place when the indentor is a large colloid. Therefore the tip can, in principle, deeper penetrate into a brush because the resulting forces per unit area are smaller than for the colloid due to the possibility of lateral escape of the brush polymers. This would result in a different thickness of the incompressible area of the brush. Probably, both factors play a role in explaining the differences of the calculated forces per unit area as displayed in Fig. 5.15.

In summary, it follows that the sharp tip and the colloidal probe explore different parts of the polyelectrolyte brush. While with the tip the behavior of deeper regions can be explored the colloid senses largely the behavior of the looser corona in front of the denser part of the brush. In this way the applied two ways of exploring the nanomechanical properties of polyelectrolyte brushes are complimentary. For example, with a sharp tip one cannot, in principle, explore the behavior of the loose corona if the distance between the polymers is on average greater than the diameter of the indentor.

An important parameter of the brush is its compressibility. It is obviously a function of distance from the support since the brush does not show a Hookean behavior. The compressibility can be defined as

$$\kappa(h) = \frac{1}{h - h_0} \cdot \frac{dh}{df} = \frac{(h - h_0)^{\alpha}}{\alpha \cdot K} \qquad (8)$$

taking advantage of the explicit power law for the measured force per unit area, f. The parameters α and K are given in Table 6. The distances h should is measured in nm. The compressibility is calculated in nm²/nN.

.	Tip				Colloid			
C [mM]	0	10	100	1000	0	10	100	1000
K [nN]	2.6	0.4	0.14	0.056	0.0004	0.00027	0.00017	0.0002
α	1.97	1.88	1.9	1.78	1.97	1.98	1.96	1.97

Table 6 Parameters for compressibility calculation according to Eq. 8.

It follows from the data presented in Table 6, that the compressibility's corresponding to the measurements with the colloidal probe are much larger than those measured with the tip, $\kappa \sim K^{-1}$. This can be an expected because as mentioned above the colloid senses the comparatively loose corona of the brush. Furthermore, the compressibility decreases with increasing ionic strength, because the electrostatic repulsion decreases likewise.

5.3 Conclusions

The morphology and responsive properties of a Polyelectrolyte brush of Poly (Potassium 3 – sulfopropyl methacrylate) were investigated by imaging at increasing loading forces as well as a function of the salt concentration. It was shown that the Brush interface is very sensitive to external applied forces as its thickness decreased gradually as the loading force was increase during imaging. An equation of state of a compressible liquid was applied to describe the force versus distance curves obtained after the brush was compressed with a typical AFM tip and with an 8 μm silica colloid. Imaging and indentations with the ultrasharp AFM tip allowed to explore deeper regions of the brush while with the colloid only the repulsive behavior of the outer brush corona could be quantified. It was observed that the compression depended on ionic strength weaker than expected from Debye theory. This was attributed to collapse of the brush layer at increasing ionic strengths. The application of the model of a compressible liquid allowed defining an equilibrium brush thickness.

6. Virus-Like Particles as responsive biomaterials

6.1 Introduction

Viruses are truly interesting objects of study in the biological sciences. Their simplicity in composition together with the fact that some of them are the direct cause of severe diseases for animals and humans with mortal consequences makes them not only interesting but overall of paramount importance in the life sciences. Since their first visualization, viruses have cause special interest due their minute size, rich spectrum of structures and complex features displayed during their life cycle. The capacity and specificity for infection varies among viruses. Some viruses reproduce among quite different species, while others remain specific to a single one. Because viruses camouflage has been acquired through millions of years of evolution with its host, their specificity as well as their strategy of invasion has evolved together with the defense mechanisms of the cell. This allows them to successfully overcome all barriers imposed by the cell and take advantage of its macromolecular machinery in order to replicate since they lack own metabolic functions mandatory for life. Furthermore, viruses have shown to resist and survive through thousands if not millions of years coexisting with species where their survival is a balance between mutation rate and conservation of certain fundamental structural components.

Modern concept of a virus, structure and life cycle

From the biologist point of view viruses are obligate parasites which main goal is to infect and reproduce by making use of the synthesis machinery of the cell. However for a physicist, viruses are tiny molecular machines with outstanding material properties able to withstand harsh environmental conditions like mechanical damage, exposure to chemical hazards, change of phase transitions and with the capacity to perform well coordinated specific functions in space and

time. Some viruses can remain in a frozen state for long periods of time waiting in stealth the arrival of its host. On the other hand, they can entirely disappear by integrating their genome with that of the host and staying in a dormant state until a special event (i.e. due activation of a gene) bring them back to action. The latter together with their tremendous ability to spread among different species, make viruses remarkable information carriers among living beings in the planet.

In general a virus is made of two main structural components: a protective shell and its cargo. The protective shell is a protein cage which in some cases it is also enclosed within a lipid membrane or envelope decorated with spike proteins usually derived from the host. The delivery cargo is highly condensed DNA or RNA molecules and in some particular cases also proteins.

Nowadays within the scientific community, viruses are considered not only as infectious agents but rather as delivery vehicles able to encapsulate nucleic acids, enzymes and other low molecular weight molecules, with potential capacity to release their cargo with accuracy at specific sites in a living organism. Therefore through the years, the perspective about viruses is changing from purely harmful pathogens to miniaturized molecular containers with prominent capacities and lately as potential candidates to cure diseases.

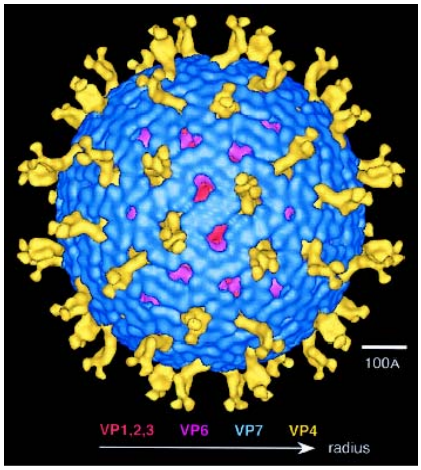

Figure 6.1 An example of a nonelveloped virus, the Rotavirus. Image taken from reference [167].

At first glance, a virus seems a rather simple entity with no more than two or three main constituents. In a virus particle a highly condensed nucleic acid is wrapped inside a protein coat or capsid, which in some occasions is further encased within a lipid envelope decorated with proteins that protrude out from the membrane. The contained genome can be DNA or RNA. While the capsid is assembled from multiple copies of a single or a few proteins, the protein decorated envelope is normally taken from the cell membrane when the particles budding of the cell. Also in a few cases enzymes or toxins are packed together with the genome for posterior use as part of the replication process. In a virus, structure and function is entwined within the shell of the viral particle. Whatever is the case of enveloped or non-enveloped virus, the surface of the particle provides the necessary tools required to gain access into the cell (See Figure 6.1) [168].

The fate of the viral particle and its survival during propagation strongly depends on the physical characteristics conferred by its protective coat. Viral capsids are formed by the spontaneous assembly of protein subunits into closed regular structures without external energy input. This is an interesting feature, because in numerous biological processes the generation of coordinated movement often requires the intervention of ATP hydrolysis for example. Protein self-assembly assumes specificity among single structural subunits. Therefore, after single proteins gather to form capsomers, these are subsequently ordered to encase the genome and finally to seal the entire shell. The concomitant process of capsid assembly and genome encapsulation is not yet fully understood [169, 170]. The final constructed capsid exhibits specific shapes with a restricted range of morphologies and well defined dimensions.

The use of new advanced microscopic techniques together with the development sophisticated image processing has increased our understanding of the detailed structure of viral capsids up to atomic resolution. An excellent review on the structure on viral capsids and modern techniques for capsid reconstruction has been given by T.S. Baker [171]. The self-organization of proteins can lead to the formation of rod-like structures like in the Tobacco Mosaic virus, spherical shapes

like the one displayed by the Dengue virus and another amorphous architectures like that of the HIV virus. Viruses that infect bacteria differ from others in structure in such a way that an ATP driven molecular motor is required to package their genome inside the capsid once this has been assembled. This viruses known as bacteriophages have been found to encase their nucleic acids under high pressures which arises from the self-repulsion of the condensed chains within the small volume available inside a capsid (For example, in λ phage a 17 μm long double stranded DNA is packed within a capsid with an internal diameter ~ 50 nm). In these pressurized containers the use of the additional packing nanomachine is mandatory, since the stored pressure inside the capsid is later used to expel the genome out during the infection of the cell [172]. A large number of viruses fall within those with a spherical geometry and shell size between 14 – 400 nanometers. It was initially observed that viral capsids with a large diameter showed a more faceted shape than the smaller which remained rounded.

The formation of viral capsids driven by self-assembly represents a marvel of molecular engineering and design. In a milestone study on the construction of regular viruses, Caspar and Klug developed a geometrical scheme that aided to justify the placement of the protein subunits within the capsomers along the capsid

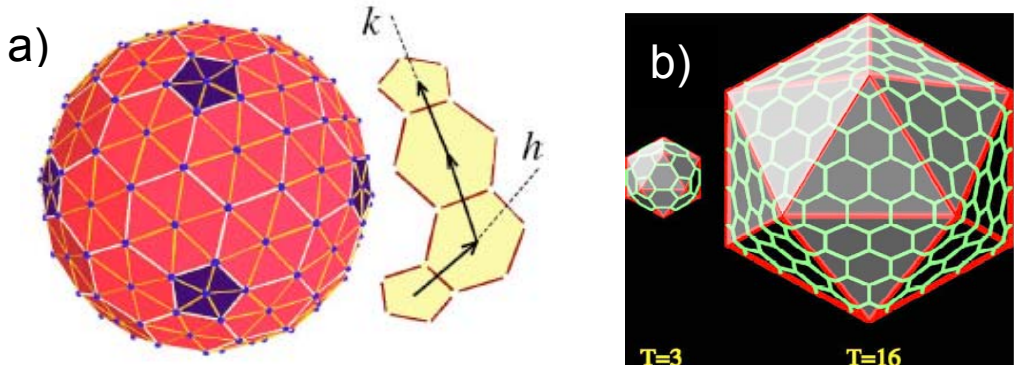

Figure 6.2 a) Schematic representation of the Caspar-Klug construction. b) Triangulation numbers applied to describe morphological characteristics of capsids like T = 3 for CCMV virus and T = 16 for Herpex Simplex virus. Images taken from references [143, 146] .

surface [173]. Within this idea, a closed shell with icosahedral symmetry can be constructed by inserting pentagons at particular positions of a planar hexagonal lattice. The insertion of pentagons, break the symmetry of the flat lattice and induce the curvature needed to close the structure. The pentagons are spaced out *h* steps along one lattice direction and *k* along the other when a rotation of 120° is made on the surface of the shell as shown in figure 6.2. Here *h* and *k* are non-negative integers and hence the triangulation number $T = h^2 + hk + k^2$ furnish the number of inequivalent sites in the resulting shell. The Caspar-Klug (CK) framework can be used to classify a wealth of spherical viruses with icosahedral symmetry which are made with 12 pentagons and $10(T - 1)$ hexagons. The total number of proteins subunits involved can be calculated through $12 * 5 + 10*(T - 1)*6 = 60T$. The basis stated in the CK framework is the foundation of contemporary structural virology with which most of viral capsids are currently classified and described. However a new theory developed by Twarock has been reported which span viral capsids with more complex structures than those described under the CK scheme [174].

It was initially observed that viral capsids with a large diameter showed a more faceted shape than the smaller which remained rounded. The last together with the obvious icosahedral symmetry presented by capsids like that of Adenovirus started to establish the connection between elastic and bending properties present in such protein assemblies [175].

Viral capsids result from the assembly of a few protein products or in some cases from the assembly of a single protein. Recently it has been shown that …is not a strict requirement for assembly, thus empty shells can be produced.

If the protein shell has been assembled without genome, then its mechanical properties are determined by the noncovalent interactions among capsomers and their respective intrinsic flexibility. By their own, some capsids have shown the capacity to expand or contract according to the environmental conditions [176, 177].

Hence the viral capsid has a direct influence not only to protect and transport the genome but also to deceive the defense mechanism of the cell and to accurately release its cargo during the entry into the cell. The different pathways a virus have to follow in order to reach a potential host is broad, and this is because the fate of the infective particle once outside the cell is dictated by the physical and chemical characteristics of the viral particle. For instance Influenza and Rubella virus are bounded to remain under a liquid environment during the search of a new host, they are not allowed to dry or to get exposed to drastic changes of pH conditions, if not they would be structurally damaged and their infective capacity could be compromised. For this reason, usually these types of viruses are naturally transmitted through ejected liquid droplets in saliva, body fluid exchange or mechanical tissue injures where body parts are exposed to blood transmission. This delicate nature is principally gained by the presence of the phospholipid envelope and its embedded glycoproteins. On the other hand, viruses such as Rotavirus and Noroviruses do not possess a lipid envelope and are not restricted to stay in liquid state to keep their infective properties in optimal conditions. These viruses can adhere to solid surfaces and be dried out, be immersed in contaminated waters or be frozen for longer periods of time. Also they tolerate a wider range of pH conditions without any serious functional harm.

The course of a virus which has already managed to infiltrate inside a host organism is governed by Brownian motion. The random motion of the viral particle will come to an end when the particle confronts the target cell and attaches to its surface. The latter often occurs when viral particles are attracted due electrostatic unspecific interactions with the oppositely charged cell membrane. Nevertheless specific binding can occur which is usually mediated by a molecular receptor displayed on the surface of the cell. There are many known entry strategies used by viruses for cell invasion. Some of them induce fusion between their lipid envelope and the cell endosome to escape from degradation by activation of fusion proteins once they have gone through the endocytotic pathway (see figure 6.3).

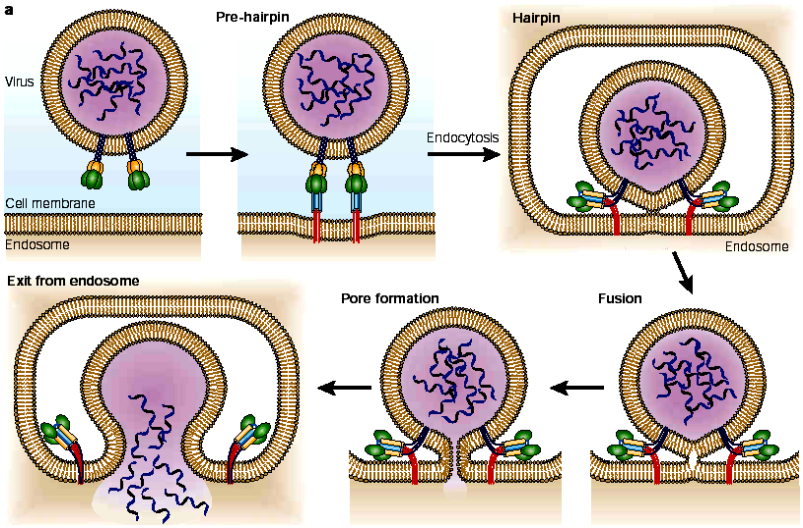

Figure 6.3 Mechanism of viral membrane fusion mediated by fusion proteins. Image taken from reference [178].

On the other hand, other will fuse at the cell membrane following receptor binding with a specific cellular receptor. Others viruses which lack envelope, induce lysis at the outer cell membrane to briefly disrupt the continuity of the lipid barrier.

Virus - Like Particles and uses of Viruses in Nanotechnology.

In protein self-assembly, the subunits involved in the final attained structure maintain their stability by balance of their conformational flexibility with the intermolecular interactions taking place among them. The physical rules behind self-assembly are yet not entirely understood, but progress have been made on the theoretical side and its experimental counterpart [179]. The remarkable assembly capacity of the capsid proteins taking place during formation of new viruses is not restricted to occur in vivo. The production of empty viral capsids in vitro from proteins in solution has been demonstrated [180, 181]. Protein self-assembly seems to be tuned by the balance between ionic strength regulated by salt concentration and the variation of pH values, as well as the temperature at which the proteins assemble. Applying modern genetic engineering techniques where

restricted expression of the required viral constituents is allowed, virus-like particles (VLPs) of enveloped viruses can also be obtained. These VLPs are produced inside cells and carry the phospholipid membrane with the corresponding fusion proteins on its surface. The VLPs possess the same architecture as its original pathogenic parental particles, but since their lack genetic material they are incapable to reproduce in cells.

These features make VLPs safe molecular tool boxes to explore for instance the host immune response, since they successfully mimic the surface interactions within the host as it has been shown to induce potent immunogenic responses [182]. The formation of well-defined spherical capsids resembling the exact dimensions as the pathogenic viral particles is not the only possible outcome from the assembly process but also other less frequent architectures can also occur. For example, it has been shown that spontaneous protein self-assembly of the Cowpea chlorotic mottle virus can yield long rod-like structures as other amorphous assemblies [181, 183]. Besides the obvious medical relevance that the use of VLPs could bring from a biological point of view, there are still the interesting biophysical properties that these macromolecular protein assemblies could render from experimental studies. For example their intrinsic physicochemical characteristics like they surface charge, swelling behavior, packing capacities and resonant and material properties upon external stimulus could pave the way for the design of new novel materials with fascinating future applications.

Because loading of empty capsids with foreign molecules with determined size and charge is possible through manipulation of their physicochemical environment, VLPs also offer attractive applications for drug delivery against cancer and gene therapy [184]. Moreover, through chemical functionalization approaches, the surface of VLPs can be modified to attach molecules of interest like antigens or metal nanoparticles to further increase their targeting capacities or detection properties (See figure 6.4). New coming amazing and unexpected applications of viruses as building blocks for materials and nanodevices have just began to give

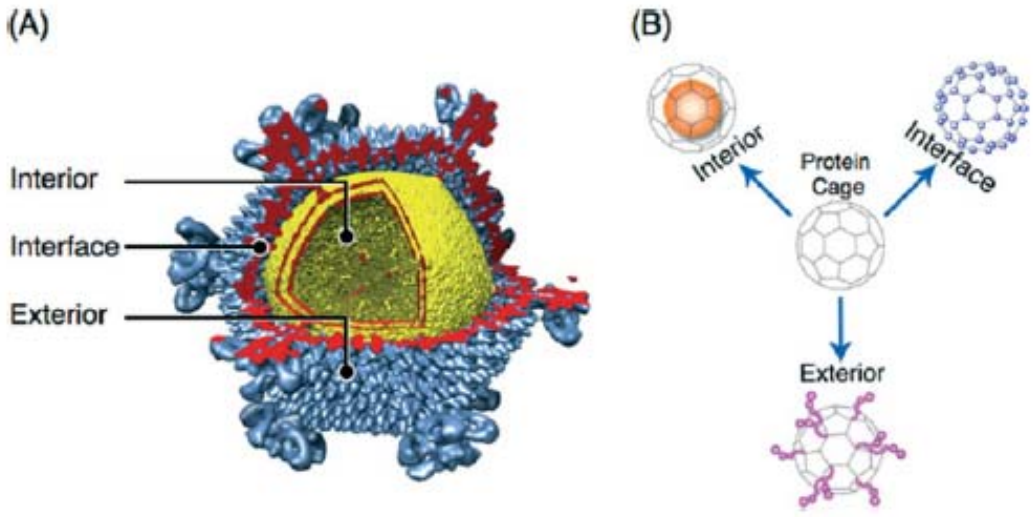

Figure 6.4 Viral nanocages exploited for nanotechnological applications. A) Distinct available structural units in a viral shell. B) Potential uses for a protein nanocage in nanotechnology. Image taken from reference [185].

first solid steps simultaneously with their use in the revolutionary emerging field of nanomedicine.

Norovirus. Structure, infection process and medical relevance.

Norovirus is an important human pathogen known to be the main cause of the epidemic outbreaks for acute nonbacterial gastroenteritis arising in hospitals, military settlements, school centers and communities in general where the hygiene conditions of water and food supplies have been compromised. Noroviruses belong to the Caliciviridae family under the genera Norovirus, with Norwalk virus being the most representative and best studied specimen. Norovirus is a non-enveloped single-stranded positive-sense RNA virus with a small icosahedral capsid with triangulation number T = 3, which has been morphologically, immunologically and biochemically characterized in the last two decades because of its persistence in the human population [186-190]. The structure of Norovirus has been revealed with cryomicroscopy and computer imaging processing techniques to a resolution of 22Å [191]. Briefly later, a nearly atomic resolution of 3.4 Å was achieved by X-ray crystallography of the prototype Norwalk virus capsid

[192]. This is shown in figure 6.5a). The Norovirus capsid is formed from multiple copies of the single protein VP1. The full capsid assembles from 180 proteins which are organized into 90 arch-like dimers with a final capsid-wall thickness of about 9 nm. The VP1 protein is subdivided into and S domain and a P domain. Thus the capsid consists of two principal domains connected by a flexible hinge, an inner smooth shell or S domain and an outwardly protruding 4.5 nm thick or P domain. While it has been demonstrated that no P domain is necessary for the assembly of round and smooth particles, the P domains confers the whole capsid better stability and the necessary molecular recognition properties [189]. A sequential assembly pathway has

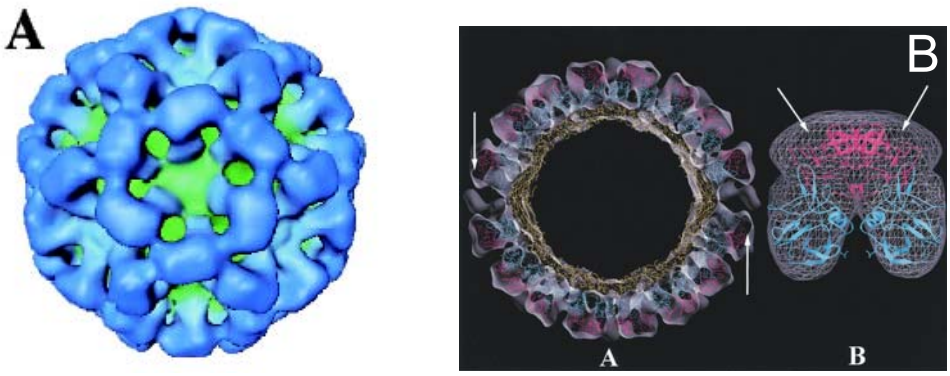

Figure 6.5 Morphology and structure of Norovirus. a) A sub nanometer resolution reconstruction of Norwalk virus (a prototype NV). b) Cross section of a Norovirus-like particle shell and respective corona protein. Images taken from reference [193].

been suggested by Prasad et al. [191]. The protruding P domain is further divided into the subdomains P1 and P2, where it has been shown that the P1 domain is responsible for the insertion within dimeric contacts of the S shell increasing this way the stability of the capsid, while the P2 contains an hypervariable region in the amino acid sequence which is thought to play an important role in receptor binding interactions with the immune system of the host. The entire capsid construction can be considered as a thin shell reinforced by incrusted proteins displaying a robust appearance with a corona-decorated surface (see figure 6.5b). The Norovirus capsid structure is distinguished by the presence of the 90 arch-like

capsomers placed at the two-fold axes of the icosahedral lattice and deep prominent depressions at all icosahedral five and three-fold axes. The three dimensional structure of Norovirus clearly exhibits a T = 3 icosahedral symmetry according to the CK classification. However, in vitro assembly have shown that smaller empty shells can also be obtained with T = 1 symmetries [194].

Despite the plethora of information related with the details of NV molecular structure, there is an important need of data concerning the virus entry mechanism into the cell. Previously, the research on its entry pathway was delayed due lack of a suitable animal model system, since NV is a noncultivatable human virus. The uptake of human NV by cells is almost entirely unknown, however it has been found that VLPs of human Norovirus requires specific attachment at the cell surface of intestinal cells with an still unknown receptor [188].

Since their discovery in 1968 after an outbreak in Norwalk Ohio, the Norwalk virus has served as prototype for the study of these fastidious pathogens whose host range does not restrict only to humans but covers other animal species like pigs, sea lions, cattle, dogs, cats and mink. NV infection is associated with a broad spectrum of diseases and organ failures like vesicular lesion, digestive tract infection, and systemic diseases. In humans NV infection causes acute gastroenteritis and accounts for more than 95% of epidemic viral gastroenteritis in adults. Primary symptoms of NV infection are intense diarrhea, prolonged vomit, nausea, low-grade fever and abdominal cramping.

Norovirus pathogenesis persists within the human population since the viruses possess three important characteristics which make it an efficient survivor. First, the viral particle is stable to drastic environmental conditions, since it resist drying, freezing, heating to 60 °C, changes in pH from 3.0 to 7.0, immersion in vinegar, alcohol, high sugar concentrations, aseptic hand solutions and disinfection with chlorine. From the former is clear to realize the threat of imminent outbreaks on places where devastation or a natural catastrophe had occur because the NV uses contaminated food, untreated waters and no disinfected supplies as reservoirs.

Second, the virus is highly contagious and is mostly transmitted by direct contact or through the fecal-oral route. It has been shown that minimal dose is required (<100 particles) to produce effective infection. Third, the high rate of mutation of NV, and especially the hyper variable region in the P2 domain of the capsid epitope confers the virus the ability to evade the immune system surveillance [195].

Rubella virus. Structure, infection process and medical relevance.

Rubella virus (RV) remains as the sole member of the separate genus Rubivirus under the Togaviridae family of animal viruses. Rubella is a round or ovoid enveloped positive- strand RNA virus with a diameter of about 60 nm. Scanning electron microscopy has revealed an electron-dense spherical core surrounded by an electron-lucent region between the core and the lipid envelope as shown in figure 6.6a [196, 197]. The viral particles contain three structural proteins: the C or RNA-binding protein responsible to enclose the nucleic acid during capsid assembly, and the two functional surface glycoproteins E1 and E2 required for ulterior viral membrane fusion. The host-derived membrane glycoproteins form heterodimers E1-E2 on the virion surface which project out the envelope as long as 5 to 8 nm spikes (schematic represented in figure 6.6b) [198]. Wrapped inside the envelope, a capsid of about 30-35 nm has been identified by scanning electron microscopy.

Because RV share several characteristics with the Alphaviruses family, being Semliki Forest virus and Sindbis virus the best well studied examples, it has been speculated that RV capsid could display a protein arrangement with T = 3 icosahedral symmetry [199]. Nevertheless, since Rubella virus is not considered anymore as a serious threat to the human population and due technical difficulties to avoid particle aggregation and apparent capsid instability in capsid isolates, the ultrastructure of RV is not fully known. It has been demonstrated that the fusiogenic properties of the RV particle resides on the E1 glycoprotein [200].

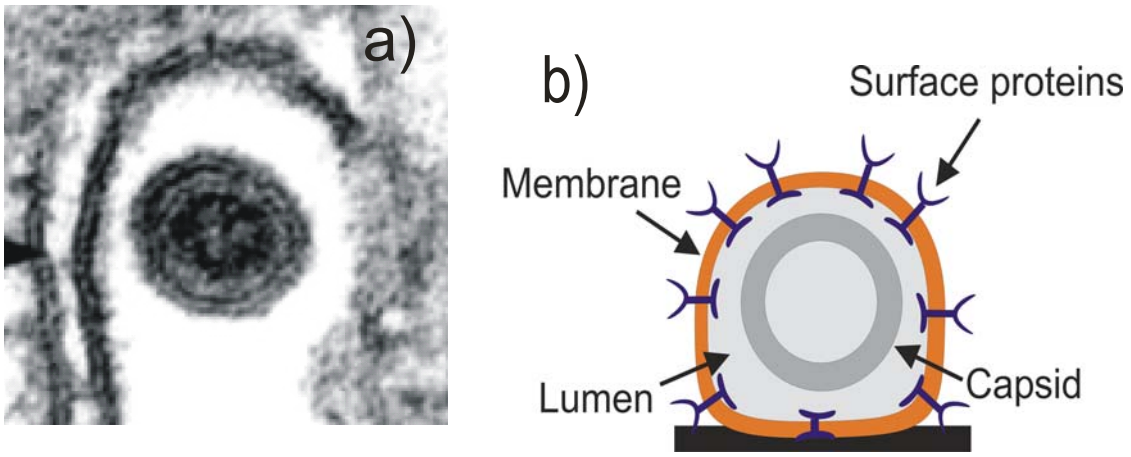

Figure 6.6 a) Scanning electron microscopy of Rubella virus. Image taken from reference [196]. B) Schematic representation of the main components in a Rubella-Like Particle.

The physicochemical characteristics of the viscous matrix enclosed between the capsid and the viral envelope are still unknown. Penetration of RV into cells in vitro has been investigated mainly in Vero and BHK-21 cell lines [201, 202]. In spite of the lack of information on the cell surface receptor, recent experiments have suggested that the latter could not be fully required for virus efficient infection, but instead certain phospholipid species would be enough to promote viral attachment and further particle entry. Early studies by Katow indicated that RV enters the cells by the endocytic pathway in which viral particles are engulfed and imported by a lipid vesicle which fuses later with the endosome at pH values of 6.0 or lower [203]. Exposure to acidic conditions within the late endosome activates the fusogenic properties of the glycoprotein E1. Under these conditions the distal extreme of the E1 spike glycoprotein is known to expose a hydrophobic domain that inserts through the endosome bilayer to initiate fusion. Viral membrane fusion is the process by which a change in a molecular conformation is triggered by low pH or other molecular interactions in the proteins at the surface of the virion to open a pore to connect viral membrane with cell membrane [204]. For most viruses entering by the endocytic pathway, once the gate between both membranes has been opened, the capsid is released into the cytoplasm for further disassembly. The entry mechanism of RV is not entirely known, but recently it has been

proposed that capsid disassembly could take place parallel with membrane fusion during exposure to acidic conditions [205]. A detailed compilation on the molecular biology of RV has been given by Teryl K. Frey [199]. The assembly of RV capsid is unique among togaviruses. The virus assembly proceeds in association with intracellular membranes of the Golgi complex instead of assembly in the cytoplasm, the common pathway followed by alphaviruses. Furthermore, it has been reported that the capsid proteins require external assistance by chaperon proteins during assembly to arrange around the genome [199]. Contrary to other related viruses, Rubella virus formation does not require a prior capsid-spike protein interaction for successful particle assembly. Instead the capsid is concomitantly or posteriorly assembled inside cisternae vesicles of the Golgi membranes.

Rubella is the causative agent of a disease commonly known as Rubella or German measles. Humans represent the only known natural host of the virus. The virus is transmitted airborne, and usually the upper respiratory tract and the nasopharyngeal lymphoid tissue serve as preferred sites for replication. Symptoms associated with infection with rubella virus are generally benign, the most frequent sign being a mild skin rash lasting for only short periods of time. Due its high teratogenicity, the most serious consequence of RV infection is the Congenital Rubella Syndrome (CRS), caused when infection take place in women within the first trimester of pregnancy [198]. The CRS induce birth defects in the fetus involving cataracts, deafness, mental retardation and heart malformations. An effective vaccine against RV is available since 1969 and was followed by an intense vaccination campaign in different countries to eradicate the virus.

6.2 Materials and methods

6.2.1 Production of Virus-Like Particles: The Baculo virus expression system

One of the most powerful, safe and effective techniques available for the production of recombinant proteins is the Baculo Virus Expression Vector System

(BEVS). The BEVS is a genetic engineering technique based on the insertion of foreign genes with the subsequent expression of recombinant proteins. A recent review in the development of the BEVS have been provided by Hitchman et. al [206].

6.2.2 Norovirus-like and Rubella-like particles production

Norovirus-like particle production. Norovirus baculovirus recombinants were generated by cloning the entire ORF1, ORF2, and 3'-UTR into BaculoDirect™ C-Term Linear DNA (Invitrogen) according to the method described by Mourez T. et al. [207]. Briefly, a 2.6 kb long fragment of a Norovirus genogroup II.7 positive sample of an infected patient were amplified by RT/nested PCR. The amplification product was cloned into Gateway® pENTRE 1A entry vector (Invitrogen), and the recombination reaction was performed using Gateway® LR Clonase™ II enzyme mix according to the manufacturer's instructions. After transfection of Sf9 insect cells, a high titter viral stock was prepared. For expression of norovirus-like particles, High Five™ insect cells in suspension culture were infected at a multiplicity of infection (MOI) between 5 and 10 using the high titer viral stock. The VLPs were harvested 7 days post infection from the culture medium and purified by isopycnic CsCl gradient centrifugation as described by White et al [194]. Protein concentrations were determined by measuring the absorbance at 280 nm, using bovine serum albumin as a reference.

Rubella-like particle production. Rubella VLPs were isolated according to the method of Hobman et al. [208]. Briefly, permanently transformed CHO cells were grown on triple flasks (Nunc) at 37.8 °C in a 5 % CO_2 atmosphere. The RLPs were released into the supernatant of the transfected cells. The supernatant was concentrated using an Amicon hollow fibre equipment (H1-100) and subsequently

an Amicon stirring cell. RLPs were separated by means of a Sepharose 4B-Cl chromatography column. The protein content was determined using the bicinchonic acid assay from Sigma.

6.3 AFM measurements

AFM. A Molecular Force Probe 3D instrument (Asylum Research, Santa Barbara, CA, USA) combined with an inverted optical microscope (Olympus IX 71, 40×) was used for imaging and force measurements. V-shaped silicon nitride cantilevers (MSCT-AUHW Veeco Instruments) with an average spring constant of 0.01-0.02 N/m and a pyramidal tip with a radius of < 20 nm were chosen to reduce shear forces on the particles during imaging. The thermal noise method was employed to determine the spring constant of the cantilever before each experiment [72].

Norovirus-like particle sample preparation. A STE buffer was used for all the experiments (100mM NaCl, 10mM TrisCl and 1mM EDTA for pH = 8.0). The employed pH values 2.0, 4.0, 5.5, 7.5, 8.5, and 10 were adjusted by addition of HCL or NaOH, respectively. Mica (25 mm x 25 mm Plano GmbH Wetzlar) was chosen as substrate because is atomically flat and requires mild preparation. Regular adhesive tape was used to separate apart adjacent sides of a mica slide to produce a clean surface. Then, the cleaved mica slides were glued to microscope glass slides with adhesive tape before use.

No chemical functionalization method for the attachment of Norovirus capsids was required. A 5-10 µL droplet of the VLP stock, 1.4 mg protein/mL, was directly deposited onto the mica surface and incubated for 20 minutes with 50 µL STE buffer solution pH 4. After 20 min it was repeatedly rinsed with the same buffer to remove any unattached particles. The sample was never allowed to dry and was always maintained under STE buffer solution at the desired pH value. When measurements were conducted at another pH value, the VLPs were first incubated and imaged at pH = 4.0, and only then the sample was repeatedly rinsed and

incubated with the buffer of the desired pH value. It was observed that Norovirus VLPs attached stronger to the mica surface when deposition was performed at acidic pH values.

Rubella-like particle sample preparation.

No chemical functionalization method for the attachment of Rubella-like particles was required, however it was clearly noticed that their adhesion strength to the substrate decreased considerably in comparison with Norovirus-like particles. During imaging, Rubella-like particles were very sensitive to detachment by shear forces and therefore minimal loading forces together with reduced scan rates were used.

A 10–20 µL droplet of the RLPs stock (4 µg/µL) was directly deposited onto RCA-treated glass slides [150]. After 30 min it was repeatedly rinsed with neutral citrate phosphate buffer to remove unattached particles. The sample was never allowed to dry and was always maintained under citrate phosphate buffer solution at pH 7.2 at the beginning and later on at the desired pH value.

To investigate the transition in mechanical properties of Rubella VLPs from neutral pH to acidic pH, a sample of Rubella VLPs were first imaged and tested by nanoindentations in pH = 7.2 and then the sample was exposed to pH = 4.5 to perform further imaging and nanoindentations.

Imaging and Force measurements. Force both VLP samples, normal forces in the range of 10-30 pN were applied for imaging areas of about 5-3 micrometers at scanning rates of 0.6 Hz (30 µm/s). This way, particle damage by the tip was minimized. When still smaller forces were used, the loss of contact between tip and sample prevented successful imaging. Thus, the VLPs were frequently imaged at the minimal loading force F_m. It was observed that, Norovirus VLPs could tolerate higher loading forces during imaging than Rubella VLPs. Their difference in

resistance was later reflected in their contrasting mechanical properties as shown further below in sections 5.3 and 5.4. The measurement of the diameter of VLPs from imaging was obtained from the cross sectional profiles as the width at half maximum height.

For the indentation measurements, a maximum loading force of 6 nN was used for Norovirus VLPs. On the other hand a maximum loading force of 2nN was used for Rubella VLPs. An approach tip velocity of 300 nm/sec was applied in both cases of VLPs per indentation. The position of the tip with respect to the sample surface, called separation, was calculated from the piezo position and the cantilever deflection. A force-separation curve is thus obtained by subtracting the deflection of the cantilever from the piezo position.

Capsids spring constant calculations. The compression of the VLP by the tip can be represented as two springs connected in series represented by the capsid and the flexible cantilever. The slope of the force distance curve contains the combined force response of the cantilever and the capsid, respectively. It provides an effective spring constant, K_{Eff}. The latter was calculated from the linear region of the force distance curves by fitting a linear function (Igor Pro 5.03 Wavemetrics) to a selected region. Following contact, a force of 600 pN was chosen as the upper limit for the fitting range for the case of Norovirus VLPs while a force of 200 pN was selected for the case of Rubella VLPs. The intrinsic capsid spring constant is therefore related to that of the cantilever by $K_{Cap} = K_{Cant} \cdot K_{Eff} / K_{Cant} - K_{Eff}$.

6.4 Results and discussion: Mechanical properties of Norovirus capsids

6.4.1 Particle size and morphology

AFM experiments require the VLPs to be stably attached to the mica support. It turned out that no special protocol was necessary to immobilize the VLPs to the mica surface. The adhesion forces were sufficiently strong to prevent displacement during imaging or indentation. Images were firstly obtained in wide scan fields of 3-5 µm applying tapping or contact mode, and afterwards the scan region was reduced to 1-2 µm (See Figure 6.7). It was found that contact mode was superior over tapping mode concerning the achieved resolution. The viral capsids appear as spherical particles adsorbed to the flat mica support. Figure 6.8A and C show 2D and 3D AFM images of VLPs observed at pH = 2.0. Figure 5.8B) provides a height profile along the thin line in Fig. 6.8A. For pH = 2.0 the median values for the measured heights and diameters taken on 50 VLPs were H_m = 28.4 nm and w = 120.3 nm, respectively. The shape of the particles did not noticeably change as a function of pH in the range of pH 2-10. However, the number of particles recorded

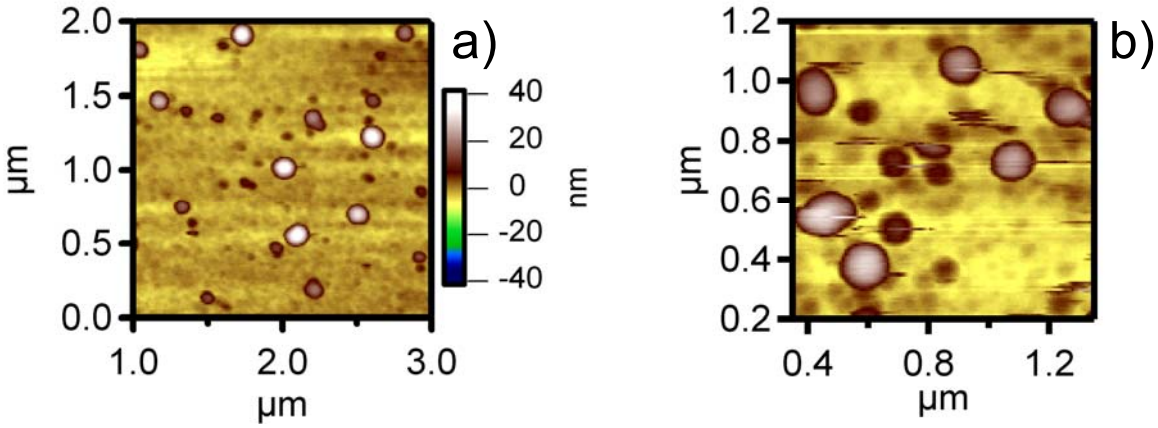

Figure 6.7 2D Atomic force microscopy images of Norovirus-like particles onto mica.

at pH 8 and 10 was slightly less than observed at acidic and neutral pH. This may be caused by a decreased stability of the VLPs at basic pH. They could have been removed from the mica support by the rinsing step before the VLPs got analysed at

pH 8 and 10. This decreased stability to shear forces under alkaline conditions is supported by the observation that the VLPs at pH 10 can be easily scratched and do not withstand repetitive imaging. Details on the pH dependence of the particle size are provided further below. In contact mode atomic force microscopy touches the sample during scanning, inducing this way a small compression on soft samples. In addition, the tip exerts shear forces on the particle while imaging. This has to be taken into account when the dimensions of the particles obtained from AFM images are compared with those obtained with other techniques. Furthermore, adhesion to the mica support can induce an additional reduction in height because partial spreading of the VLPs may occur. Another important factor is that due to convolution of the tip small objects appear much wider as they

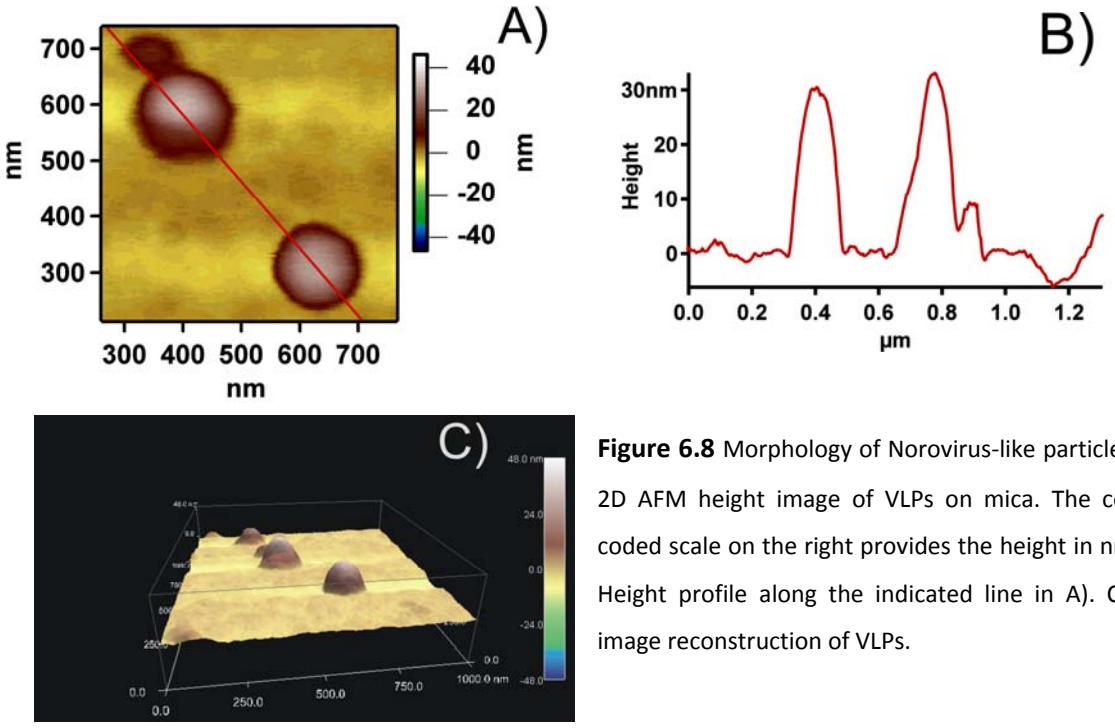

Figure 6.8 Morphology of Norovirus-like particles. A) 2D AFM height image of VLPs on mica. The colour coded scale on the right provides the height in nm. B) Height profile along the indicated line in A). C) 3D image reconstruction of VLPs.

actually are. Regardless of the just discussed limitations in the accuracy and limitations of AFM measurements the obtained particle height nevertheless represents a useful parameter, which, however, as a rule is smaller than the real height. It was found that there were populations of particles differing in height as

can be observed in figure 6.7a. Most of the particles had a height of the order of 30 nm. Smaller particles of about 20 and less frequent larger particles of about 90 nm, were also observed. These particles may represent different triangulation numbers, i.e. T = 1 for the smaller particles. The disassembly and self-assembly of VLPs into other sized particles and structures has already been reported [180, 181]. For instance, J. White et al found that Norovirus VLPs can re-assemble into smaller particles of about 23 nm in diameter (T = 1) [194]. They showed that antigenic and biochemical properties of these particles were conserved. However, the infectivity of viruses with aberrant triangulation numbers may be lost. The assembly of capsomers into capsids with larger T numbers has been also reported [209].

6.4.2 Force measurements and capsid stability as a function of pH

To obtain the mechanical strength of Norovirus VLPs, cyclic indentation – retraction experiments were conducted. To this aim single NLPs were indented up to a load of 6 nN immediately followed by a retraction of the tip. Details on the rate of indentation and the duration of a complete loop are provided in the previous section. Before probing a particular particle a control approach-retraction experiment was run next to the particle at the solid mica support. This experiment was taken as the reference. Afterwards the tip was positioned centrally above a particular VLP which was identified by preceding imaging. In force vs. separation curves a vertical line is expected when the tip is pressed against a hard surface.

This is the case for curve 6.9a) referring to the control experiment. After gradually increasing repulsion at very short range the force curve raises steeply approaching a vertical line. When the VLPs were probed at pH values ranging from 2 to 8.5 the

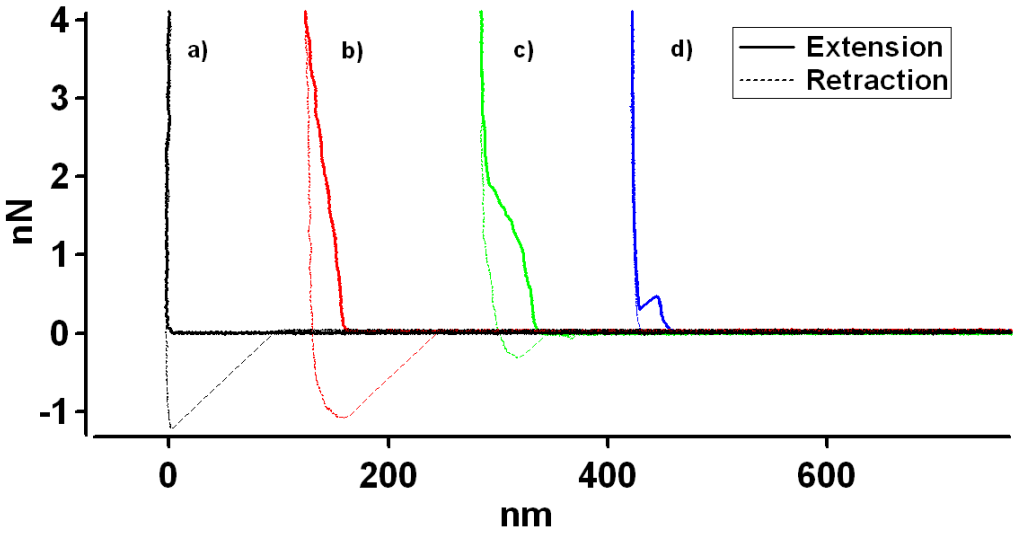

Figure 6.9. Force separation curves with typical features obtained at different pH on Norovirus VLPs. For every curve, the extension (bold) and the retraction (dashed) parts of one full cycle are shown. a) Control curve on mica. b) Linear response upon compression. c) Gradually increasing compliance with increasing load. d) Sharp drop in force.

typically observed force – separation curves could be classified into three different indentation scenarios, represented by the curves b, c, and d in Fig. 6.9.

In approximately 65% of all curves we found a linear response of the VLPs up to a load of a few nN, curve b) in Fig. 6.9. In 17 % of all analysed cases the compliance increased at higher loads after an initial linear force response, curve c) in Fig. 6.9. The initial slope was, however, of the same order as in case b). 18 % of the analysed force – separation curves showed a sharper drop in force as in case d) in Fig. 6.9. The initial slope was in a range similar to case b). It is quite remarkable that the linear response persisted even for very large deformations of the order of the dimensions of the particles themselves ranging in most cases over the entire accessible range of compression. For example, in Fig. 6.9b), compression stops at a force of about 4 nN. We believe that in this case the capsid has been completely flattened at least in the region directly underneath the tip. Considering the small tip radius of about 10 nm a force of 4 nN creates a pressure of more than 100 bars. The maximal load of 6 nN corresponds to maximal pressures close to 200 bars.

Because of this large value of the applied pressure it is conceivable that partial displacements or failures of the capsid may occur. This is, what we believe, the reason why the curves c) and d) deviate from the linear slope or show sudden drops in force under compression. It was recently shown that viral capsids with a triangulation number of T < 7 cannot undergo buckling as a result of geometrical constraints. Since the VLPs belong to T = 3 class of capsids the observed decreased compliance at higher loads or the sudden drops in force have to be caused by either conformational changes of the capsomers, maybe partial denaturation, or by breaking capsomer - capsomer interactions [210]. An inspection of the retraction curves (dashed lines in Fig. 6.9) revealed almost always a single well-defined detachment point around the same distance as the point of first contact in the approach curve. The detachment typically required a

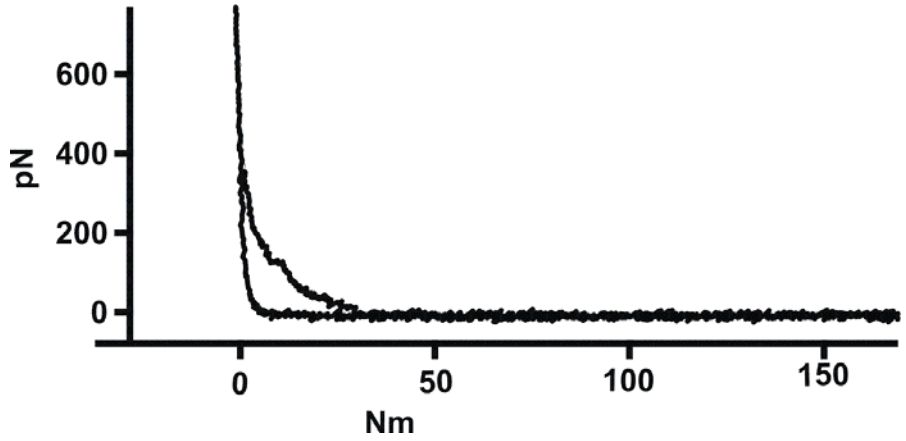

Figure 6.10 Compression of NLP at pH = 10. It can be observed that the particle provides a weaker response to compression by the tip.

tensile force of the order of 10^2 pN to 1 nN. The approach – retraction cycle is associated with a large hysteresis. Immediately after the retraction started, the forces dropped to negative values indicating that there was some adhesion of the tip to the capsid surface, and, that the rate of relaxation of the capsid to its original shape was smaller than the rate of retraction of the tip. At pH 10, however, the indentation behaviour was remarkably different. While a force in the range between 1.5 to 5 nN was required to entirely compress NLPs in the pH range between 2 and

8.5, forces below 500 pN were sufficient to reach the hard surface at pH 10. This pronounced decrease of the particle rigidity was accompanied by a decrease of the slope indicating a significant increase of the compliance of the VLPs at pH 10 (See figure 6.10). It has to be kept in mind that the deformation of the capsid and the displacement of the capsomers are both large compared with their dimensions. For this reason, strictly speaking, the framework of continuum mechanics can only be applied with caution. Therefore, although the response in curve 6.9b) is linear over the entire range, elasticity in the sense of Hooke's law behaviour may not be the only explanation. It may also be that upon approach the work performed by the external forces is gradually converted into conformational changes of the capsomers or into the breakage of intermolecular bonds rather than being stored as elastic energy in terms of stress. When the external force is relaxed the inbuilt self-assembly features of the capsomers will gradually restore the original shape. This view is conceptually different from the behaviour of elastic bodies where after

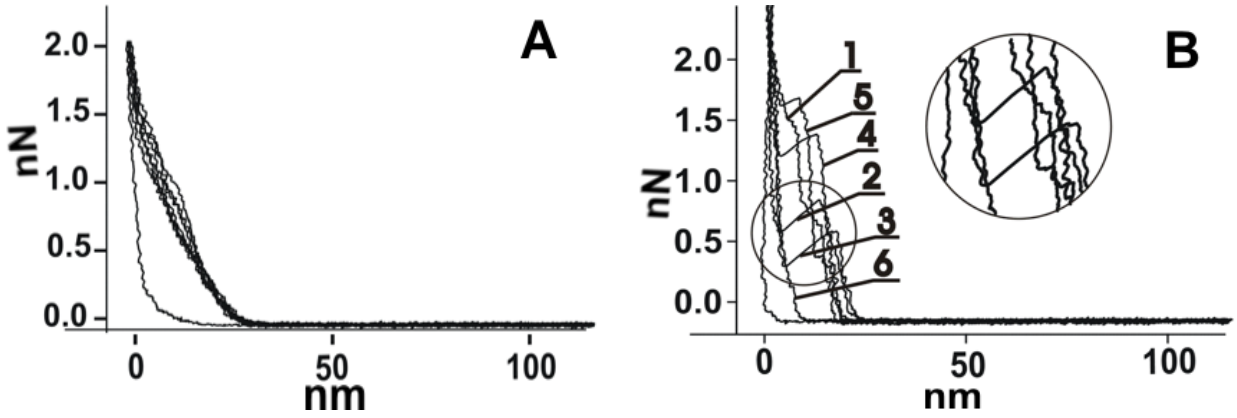

Figure 6.11 Consecutive force separation curves taken on a single VLP. Only approach curves are shown: A) Full reversibility. B) Progressing failure. Numbers indicate consecutive force curves.

the external load has been removed the relaxation of the intrinsic stress restores the original shape. The reversible behaviour of the Norovirus VLPs within the pH range of 2-8.5 was demonstrated by repetitive indentations. 80 % of probed VLPs

showed a reproducible linear force response as shown in Figure 6.11A) over up to 8 consecutive indentation - retraction cycles. Fig. 6.11B) illustrates the typical behaviour when a failure occurred. After some repetitive loading – unloading loops sudden drops in the force appeared as indicated in the zoom in Figure 6.11B).

Even when a drop in force occurred, which is equivalent to a sudden jump-in of the tip into the VLP, this did not necessarily affect the initial slope of the subsequent force curves. This can be clearly appreciated in Fig. 6.11B) where multiple fracture events emerge for repetitive compressions; nevertheless the slopes seem to be unaffected. From the materials point of view this result is interesting because a major mechanical failure did not interfere with recovery of the capsid after the load has been removed. This obvious self-healing is brought about by the inherent self-assembly features of the capsid. As a rule, an irreversible failure (trace 6 in fig. 6.11B) of the capsid occurred for the majority of VLPs after more than 10 consecutive indentations had been performed. As mentioned above it is difficult to obtain true data for the width as well as for the shape of the NLPs from imaging. Convolution leads to an overestimation of the width and makes measurements of the particle shape below the equator impossible. Therefore, we focused on measurements of the height of the NLPs as a measure for changes of the particle topology as a function of pH.

The height of the VLPs can be obtained in two different ways. One possibility is to get the height from imaging (H_m) as demonstrated in Fig. 6.8a) and b). Another estimation of the size of the particle can be obtained from the height in contact (H_c), which is the distance between the point of contact of the tip with the particle and the vertical line at final compression. Both ways of measuring particle height have their own advantages and disadvantages. H_m is smaller than the real height because imaging requires some force to be applied which may lead to indentation of soft particles. H_c, on the other hand, does not include the vertical extension of particle material eventually located underneath the tip at final compression. This provides the respective distribution of H_c. A histogram of the spring constant taken

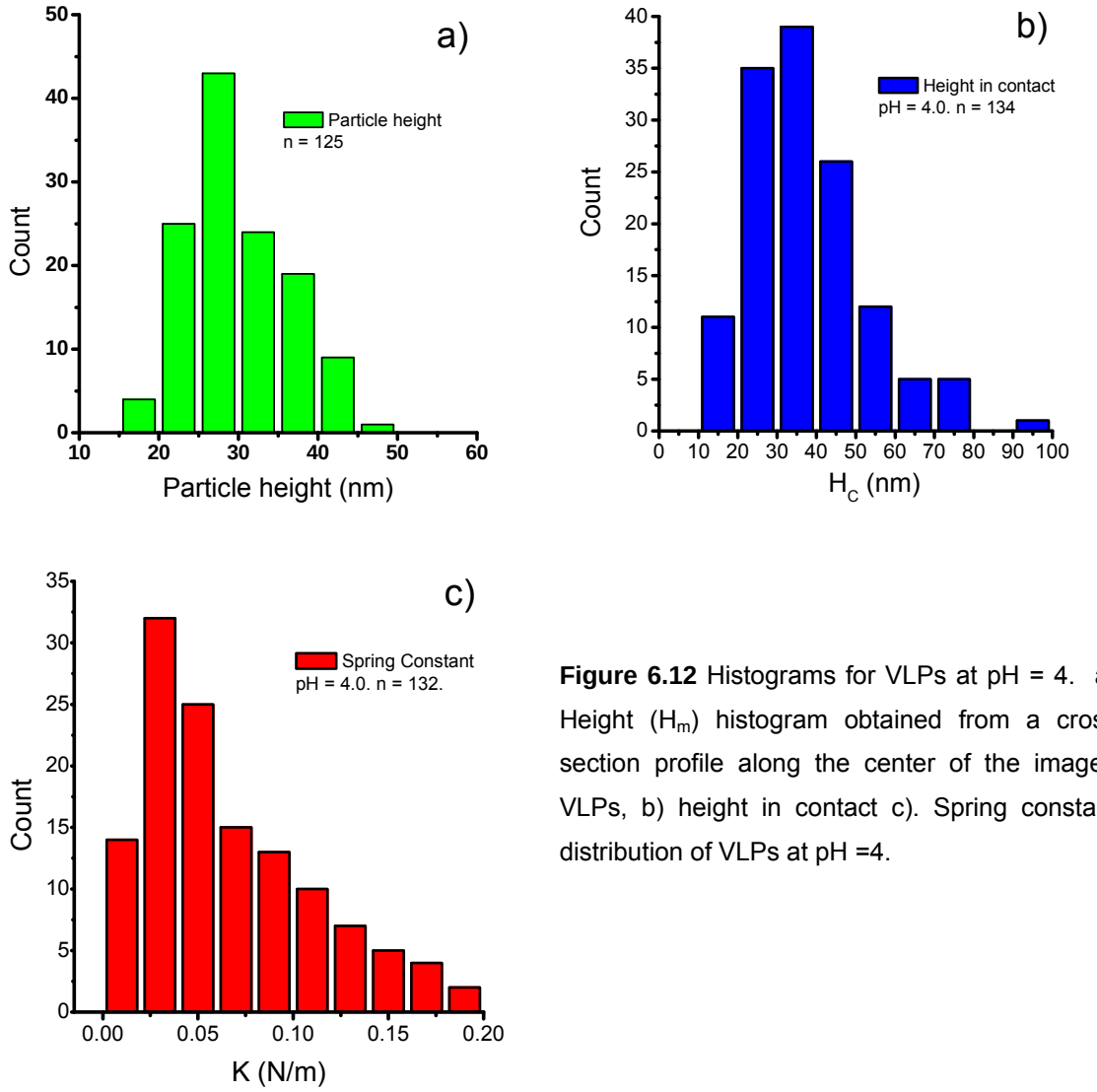

Figure 6.12 Histograms for VLPs at pH = 4. a) Height (H_m) histogram obtained from a cross section profile along the center of the imaged VLPs, b) height in contact c). Spring constant distribution of VLPs at pH =4.

has to be taken into account when discussing height data. Fig. 6.12a) shows a typical histogram for the height (H_m) obtained from imaging at pH 4. Fig. 6.12b) at pH 4 is provided in Fig. 6.12c). All these histograms deviate from Gaussian distributions. They display extended tails toward higher values. For non-symmetric distributions the arithmetic mean may not be the best value to characterize the average of the distributed parameters, since the tail may have too much weight. We therefore have chosen the median as a measure of the mean of the respective distributions. Table 1 displays the medians for H_c, H_m, VLP width, and spring

pH	H_c (nm)	H_m (nm)	W (nm)	K (N/m)
2.0	28.0	28.4	120.2	0.05
4.0	34.8	36.5	132.0	0.06
5.5	29.6	31.9	120.6	0.06
7.5	42.6	31.5	114.1	0.05
8.5	36.9	33.1	122.0	0.03
10.0	47.2	36.8	130.5	0.01

Table 7 Obtained median values for height in contact, measured height, width and spring constant for Norovirus VLPs at different range of pH values.

constants. The latter were calculated from the slope in the linear region of the force – separation curve for at least 50 particles. All parameters have been recorded as a function of pH. The capsid heights fall in a range consistent with the capsid diameter of 38 nm, which has been found by X-ray diffraction studies [192]. There is a tendency of both H_c, and H_m to increase with increasing pH. For both ways of measuring particle heights, the lowest values were recorded at pH 2, while the largest values were measured at pH 10. The increase of the particle size with pH is shown in Fig. 6.13a). It displays the measured height in contact as a function of pH. The dashed line provides the linear regression illustrating the trend of the size increase with pH quantitatively.

This increase in dimension with increasing pH may be a result of gradual conformational changes of the capsomers with pH leading to an isotropic expansion of the capsid. It has, however, to be taken into account that the interaction with the support may induce spreading and, thus, may lead to a reduction of the measured capsid diameters. Interaction with the support itself depends on the molecular properties and charge of both the mica support and the capsid, and may thus be dependent on pH in a different way than the capsid expansion. This may explain the observed scatter of the measured height as a

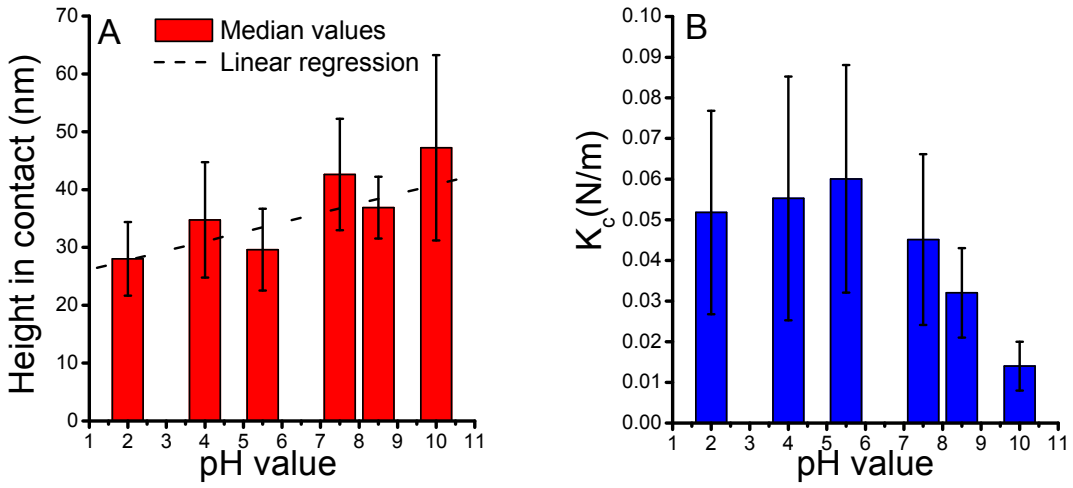

Figure 6.13 a) H_c as a function of pH. The dashed line shows the linear regression of H_c versus pH. b) Spring constant as a function of pH. The error bars represent the median absolute deviation (MAD), which is a measure of the width of the distribution.

function of pH. The average value for the spring constant did not change within the error of the measurements between pH 2 – 7. However, at more basic pH values beyond 7 the spring constant decreased considerably. The spring constant at pH 10 was about 5-fold smaller than the maximum of 0.06 N/m at pH 5.5. The decrease of the spring constants at basic pH values indicates a weakening of the capsid stability. This result is in coincidence with other findings that Norovirus capsids may disassemble at basic pH [210].

It has been found that the basic protein VP2 plays a significant role in stabilizing the NLPs [189]. At basic pH deprotonation of VP2 may led to a decrease of the capsid stability. According to Prasad et al., the interaction of the P domains is involved in forming the dimeric contacts, whereas the interaction of the S domains is essential for forming the icosahedral contacts. This has led to the conclusion that basic amino acid residues may play a significant role in stabilizing capsomer – capsomer interaction [211]. It is, however, remarkable that even at pH 10 norovirus capsids could still be found adhered to the mica supports, although they were rather weak and broke down irreversibly after one indentation had been performed.

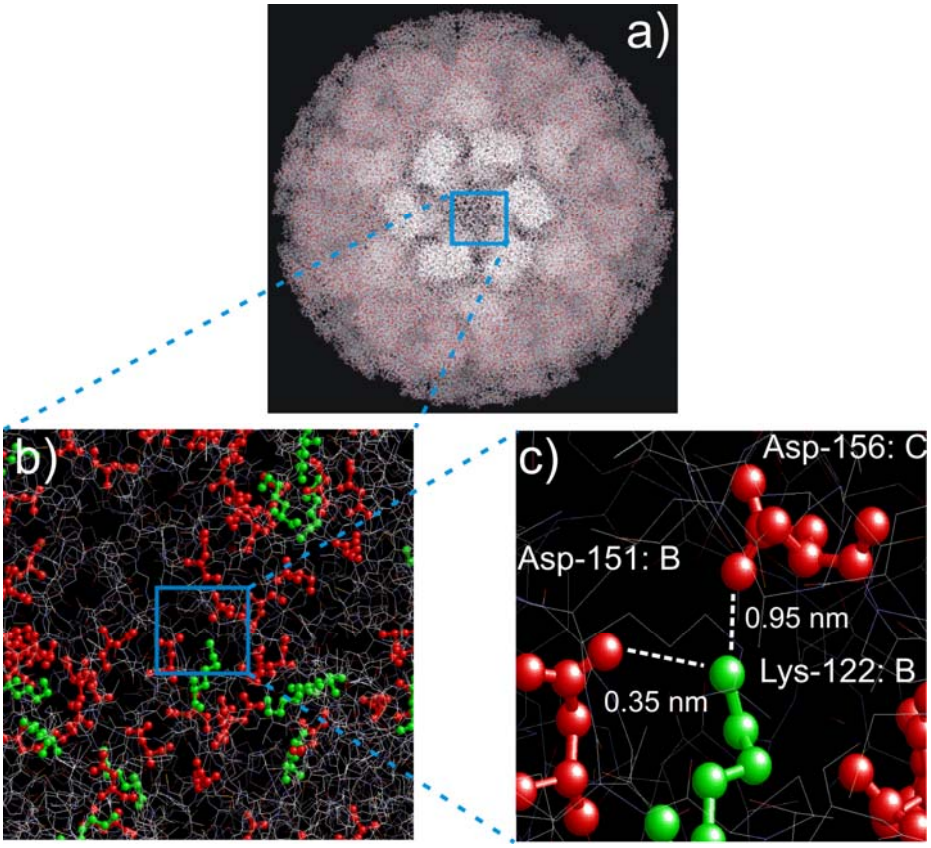

Figure 6.14 Deprotonation of Lysine triggered by increasing the pH might promote repulsion between negative charged adjacent aspartic acid which could induce capsid softening.

It would be interesting to identify sites responsible for capsid stability sensitive to pH in the range pH 8-10. Lysine is a likely candidate since its pK_a falls, just, into this region. The interaction with negatively charged amino acid residues such as aspartic or glutamic acid maybe switched on and off depending on the external pH. Analysing the crystallographic structure of Norovirus VLPs as provided by the virus database at http://viperdb.scripps.edu revealed that in the contact region between the S domains of the B and C chains lysine-122 of the B chain is rather close to aspartic acid-151 of the same chain and to aspartic acid-156 of the C chain (See Figure 6.14). The distances between the charged groups are 0.35 and 0.95 nm, respectively. The distance between the carboxyl groups of the two aspartic acids was 1.07 nm. Deprotonating the lysine by increasing the pH might thus induce

repulsion of the negative charges of the aspartic acids leading to conformational changes and, maybe, to destabilization of the capsid, thus offering an explanation for the observed softening of the capsid. There is also an aspartic acid-lysine interaction site in the P2 domain. The amino group of lysine-391 is only 3.6 nm away from the carboxyl group of aspartic acid-388. This site maybe important for the possible pH dependence of dimer formation, since deprotonating the lysine at high pH may change the conformation. It may also influence the conformation of the protrusions at basic pH. Interestingly, VLPs indented after exposure to pH 2.0 and back to neutral conditions did not show any significant mechanical instability.

6.4.3 Mechanical properties of Norovirus capsids

So far, the mechanical properties of only little more than a handful of empty viral capsids have been investigated. Young moduli E have been calculated from the mechanical response of the capsid upon indentation applying the theory of thin elastic shell [132].

According to thin shell theory the applied force, F, is linear with the indentation, ξ.

$$F = \alpha \frac{ED^2}{R} \xi \tag{1}$$

D is the capsid wall thickness. R is the capsid radius, and α is a proportionality factor that we assume to be equal to 0.8 as follows from a related study of mechanics of viral capsids [212]. With D = 9 nm, and R = 19 nm we obtain a Young modulus, E, of 30 MPa for Norovirus VLPs at pH 4. This value falls into the range of soft rubber-like materials, which are characterized by Young moduli below 100 MPa.

Another important parameter for thin elastic shells is the dimensionless Föppl von Kármán number (FvK). It characterizes the ratio between stretching and bending energies, and is defined as:

$$\gamma = \frac{Y_{2D} R^2}{K_B} \tag{2}$$

Where Y_{2D} is the 2-Dimensional Young modulus and K_B is the bending modulus [213]. Since both the 2D Young modulus and the bending modulus can be related to the universal Young modulus the FvK number, γ, finally depends only on geometric parameters of the capsid [212]:

$$\gamma = 12\left(1-\nu^2\right)\frac{R^2}{D^2} \tag{3}$$

Assuming a Poisson ratio of v = 0.35, a capsid wall thickness of D = 9 nm and a capsid radius of R = 19 nm we obtain an FvK number of γ = 77. Lidmar et al, have shown that the shape of a closed shell is determined by the FvK number in such a way that below a critical value of γ = 154 called the buckling threshold the shape of the shell should be nearly spherical, while above this value the sphericity is lost and the shell should acquire a more faceted shape [175]. The value here obtained is below the buckling threshold and therefore Norovirus VLPs should have a spherical shape, which is consistent with the images.

6.4.4 Influence of the material properties of VLPs on NV life-cycle

The selected range of pH values in our experiments covers the physiological range of pH values experienced by the Norovirus along its pathway leading to infection. The virus taken up at neutral pH has to resist the following extremely acidic conditions in the stomach. In the slightly alkaline environment of the ileum it has to bind to a receptor, to enter the cell, and to release the viral RNA. It is quite

→

remarkable, that the mechanical stability of the capsid shell as a function of pH correlates with this natural course of pH changes experienced during the infection cycle. From our experimental results regarding the measured height in contact and the capsid stiffness, it appears that a possible inherent responsiveness of the capsid shell is associated with the changes in pH. The observed softening of the capsid together with an increase in its size, when going from pH 7.0 $\longrightarrow$ 10.0 suggests that capsid suffers and expansion. The former, contrary to the observed reduction of height in contact when changing from pH 7.0 $\longrightarrow$ 2.0.

Although AFM is not the appropriate experimental technique to determine structural transitions of the capsid upon changes of pH, we can only speculate that the Norovirus capsid experience a swelling mechanism, similar to those in other better studied viral systems like CCMV or Semliki forest virus. More experiments on the reversibility of the capsid responsiveness are further required.

An associated pH-dependent capsid structural transition could represent a prerequisite for the effective disassembly of the capsid just before release of the genome within the cell. At this point is worth to mention, that during infection, the presence of the encapsulated RNA would impose an additional internal osmotic pressure against the internal capsid walls which could possible increase the stability of the virus.

In these studies the mechanical resistance of the capsid did not change up to neutral pH, but decreased at basic pH values. This decrease in rigidity of the capsid under basic conditions may have a relation to uptake and/or the subsequent release of the RNA. This may be an accidental coincidence, but nevertheless, this is, to the best of our knowledge, the first time, when the mechanical properties of viral capsids have been related to their infective properties. We believe that this observation deserves further studies.

A better understanding of the principles of capsid stabilization and destabilization may contribute to the development of new and more specific treatments as well as to the use of Norovirus viral capsids in nanotechnological applications [214].

6.4.5 More than one size in Norovirus capsid assembly

A consequence of the lack of genome during capsid assembly is that protein assemblies with a different number of subunits than those present in the infectious virus can be formed. In this study, VLPs with a T = 1 capsid structure were also observed as shown in figure 6.15. However, the most abundant capsid structure was still T = 3. The average height by AFM imaging for these smaller VLPs was 21.6 ± 0.1nm for n = 94 particles. This smaller variant of Norovirus VLP has been morphological characterized by transmission electron microscopy [194]. From these experimental studies it is predicted that these 23 nm VLPs should possess 60 protein subunits, instead of the 180 found in the regular infective particle.

In addition some larger spherical protein assemblies as those shown in figure 6.16 were found (see figure 6.16). This was unexpected, as to our knowledge, there is no reported study on the formation of Norovirus capsid protein shells larger than T = 3. Their size ranged 60 - 160 nm. Morphological features on their surface could not be distinguished. Our hypothesis is that those structures represent assemblies with a CK number of T = 7 or even larger.

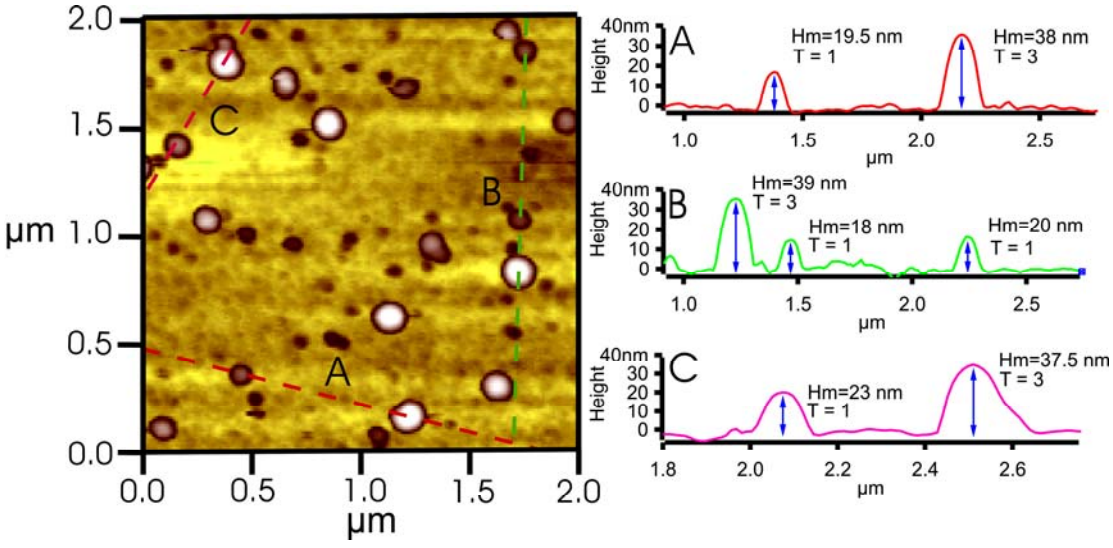

Figure 6.15 Height image of coexisting Norovirus-like particles with T = 1 and T = 3 capsid number. The capsids appear as hemispherical caps without discernible substructure.

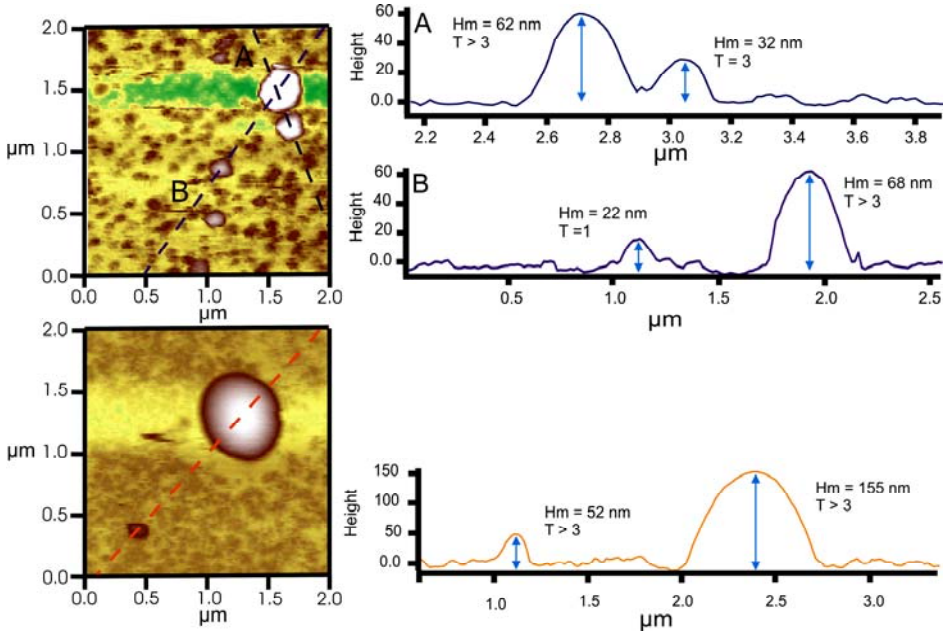

Figure 6.16 2D Height images of Norovirus VLPs with cross section profiles of different sizes which could represent alternative T =1 and T ≥ 7 capsid structures. Particles with T = 1, T = 3 and the less frequent T ≥ 7 morphology, which can apparently also be obtained in vitro after production of capsid protein through the BEVS.

Figure 6.17 shows force-separation curves from representative T = 3 and T= 1 capsids and protein shells with a postulated T ≥ 7 capsid number.

Figure 6.17a) shows the already expected linear dependence discussed in the previous section from T = 3 capsids. For the case of T = 1 capsids (figure 6.17b) a non-linear behaviour is observed within the range of compression. An obvious difference in the force response with respect to T = 3 capsids can be noticed. Ideally, as characterized by TEM measurements, a T = 1 VLP would have a size of 23 nm but the same thickness t ≈ 9 nm as for the T = 3 VLP. The ratio AFM tip vs shell thickness R/t is considerably reduced and therefore the theory of thin shells cannot be further applied. In this case, the system under consideration resembles more the compression of a spherical protein complex, since the void in the interior is only 5 nm in diameter.

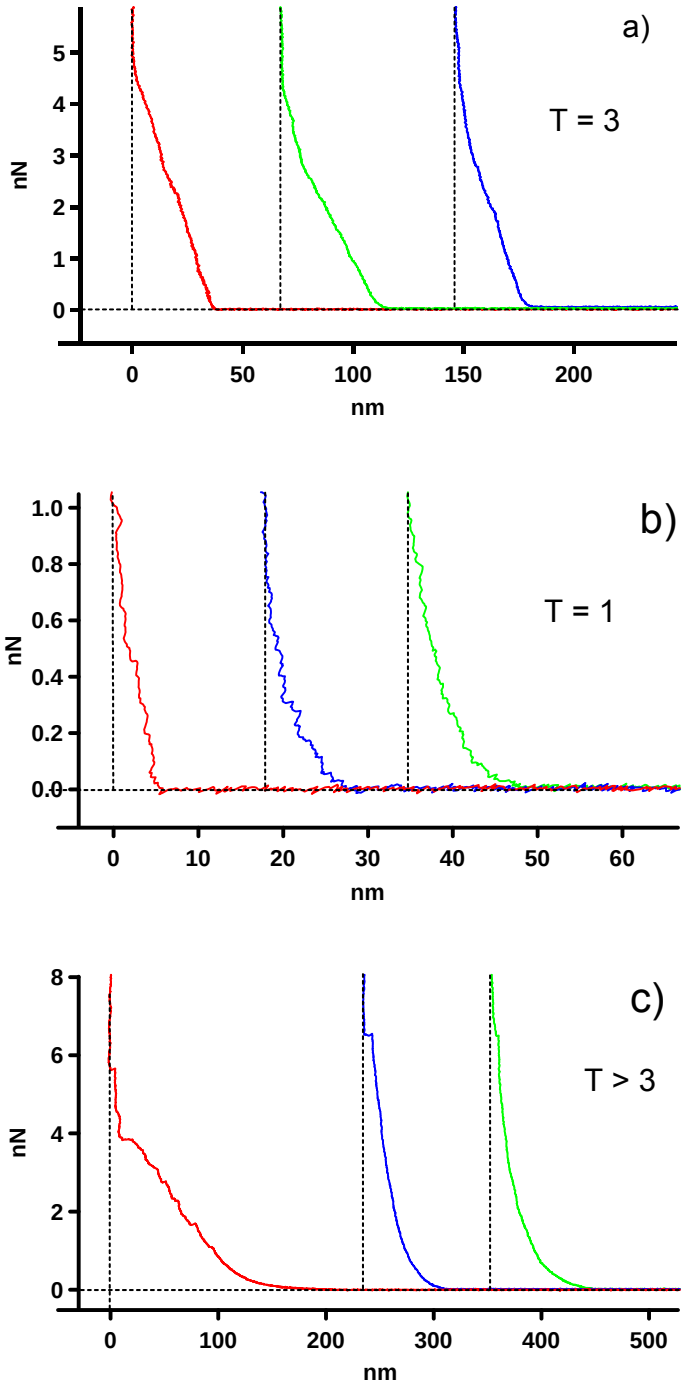

Figure 6.17 Representative F-Sep curves for Norovirus VLPs with T = 3, T = 1 and T ≥ 7 capsid numbers. A) A fully linear response is obtained for T = 3. b) For T = 1 a slightly nonlinear response is observed. c) For T ≥ 7 a nonlinear force response is observed. For sake of clarity only approach curves are included.

Nanoindetation on the large shells provided a non-linear force response as well, but in this case the shell response to the applied load was very shallow after the point of contact. Also, from the plots, drops in the force for high loading forces indicate that structural damage occurred.

These could thus be T ≥ 7 capsids according to the Caspar & Klug classification.

In a previous section, the theory of thin shells was applied to extract the material properties of T = 3 capsids. Here, however, in order to obtain a coarse estimation for the Young´s moduli for T = 1 capsids, we model the capsid as an homogeneous spherical protein complex [215]. Under this scheme, the VLP is regarded as a spherical protein sponge which is squeezed by a hard spherical indentor of the same size. This consideration is possible because the size of the AFM tip and T = 1 VLPs are about the same order of magnitude. In such a way, according with the Hertz model the degree of deformation as a function of the applied load is given by

$$\xi^3 = \frac{9}{16}\frac{\left(1-\nu^2\right)}{RE^2}\cdot F^2 \tag{5.1}$$

where ξ is the deformation, v = 1/3 the Poisson ratio, E the Young's Moduli, R = 15 nm the AFM tip radius and F the applied load. In figure 6.18a, force vs deformation plots are shown for representative cases within the same range of compression of 1nN. As shown, a linear behaviour with different slopes is obtained for the T = 3 and T ≥ 7 shells, while for T = 1, a nonlinear indentation is observed. A linear fit has been included to the data points for the T = 3 and T ≥ 7 cases. However, as can be observed in the whole set of data for T ≥ 7 in figure 6.18b, the behaviour becomes nonlinear for larger loads.

For the T = 1, a fit to the Hertz model has been applied to the shown data with equation 5.1. The dependence of equation 5.1 appears to describe well the obtained data. We obtain a value of 112 MPa for Young´s moduli for the T = 1 Norovirus capsid. This is an slightly higher value with respect to the average value

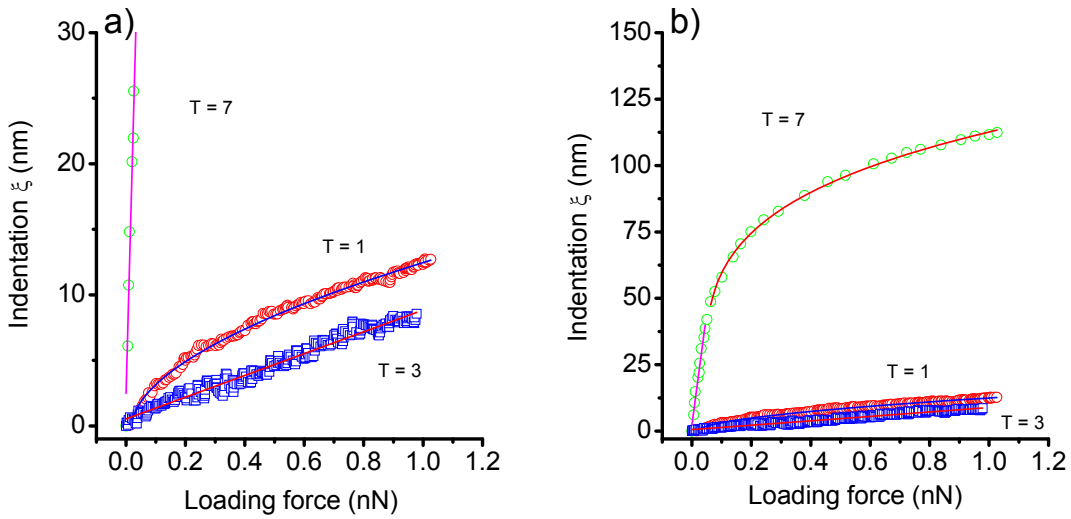

Figure 6.18 Indentation curves as a function of the applied load. a) For T = 1, T =3 and T ≥ 7 assemblies. b) Whole set of data points for T ≥ 7.

of 30 MPa that was obtained for the T = 3 capsid. We believe this discrepancy relies on the variation of the size of the AFM tip. Based on their force response, we consider the next three arguments to conclude on the nature of these large protein assemblies.

a) On mechanical grounds, the initial force response is not representative of a sphere formed from homogeneously distributed proteins, since ξ grows linearly up to indentation depths of about 50 nm, then changes gradually showing an increasing resistance for higher loads.

b) Repetitive indentations on the T = 3 VLPs (see previous section) showed that the shells are highly elastic. If the bending modulus is the same in the larger assemblies than in the T = 3 capsids deformations over a large range can be expected as observed in figure 6.17c).

c) Finally, from Caspar & Klug, there is no restriction in the possible assembly of T = 7 or larger protein shells.

What we consider here as T ≥ 7 assemblies were less frequently observed and therefore we consider that their process of formation is less favourable to occur. Is possible that spherical protein shells of this size or larger, become structural instable [209]. Perhaps the balance between the in-plane elasticity and the bending modulus across the surface of the shell is not conserved and according to the position of the capsomers, the surface could buckle leading into a faceted morphology or even fail by full collapse [175]. However this assumption is only speculative and we suggest that further experimental studies to determine their internal structure are needed.

6.4.6 Conclusions

The major finding of this study is that the norovirus capsid stability is a function of the pH. At basic pH values the capsid became gradually softer along with an increase in size. These changes of the mechanical properties of the capsid shells can be attributed to an underlying weakening of the capsomer – capsomer interaction and to related conformational changes of the capsomers. It is quite conceivable that the basic VP2 protein plays a major role in this regard. At basic pH VP2 would decrease its positive charge, which may cause the stability decrease. It is highly tempting to relate this weakening of the capsid with increasing pH to the biological function of the capsid itself. The capsid should withstand the highly acidic pH in the stomach but become infective under the weakly basic conditions of the environment within the ileum. This induction of infectiousness at basic pH may be related to conformational changes of the capsomers, which have been picked up by our indentation experiments as an increase in capsid compliance. It cannot be excluded either that the observed capsid weakening has a direct relationship to virus entry and RNA release. In any case this correlation between the mechanical properties and the biological function are highly interesting and demand further studies. Beside this possible relation to the norovirus infection mechanism, which is at present largely unknown, our

studies shed some light on the unique properties of virus capsids. These are essentially nanocontainers with an inbuilt repair mechanism provided by their inherent capacity of self-assembly.

It was shown that the capsids were able to withstand large consecutive deformations exerted by the AFM tip as has been lately probed for other viral systems [134]. Protein self-assembly, resulted in the formation of other protein structures with spherical symmetry. Empty shells with triangulation numbers T =1 and what possibly with a T > 3 less frequently observed were also present. Proper mechanical characterization of these non-infectious protein containers requires future experiments.

These findings contribute to the understanding of viral capsids as nanomaterials and may facilitate their potential use in nanotechnology.

6.5 Results and discussion: Rubella-Like Particles

6.5.1 Particle Size and Morphology

Images of the Rubella-like particles were first acquired on glass slides at pH = 7.4 to verify the presence and the topology of the VLPs. Figure 6.19 shows a height image of Rubella VLPs taken in contact mode where several particles can be observed. The Rubella-like particles were not so stable during imaging to remain firmly attached to the glass substrate as Norovirus VLPs, but instead some of them detached or got disrupted by the AFM tip. This occurred even when imaging with very small loading forces was performed. Shear forces had a pronounced effect on many imaged Rubella VLPs. The presence of a membrane envelope could be possibly responsible for such susceptibility to external deformations. At this point, is worth to mention that tapping mode was also applied, but the image quality was not superior to contact mode.

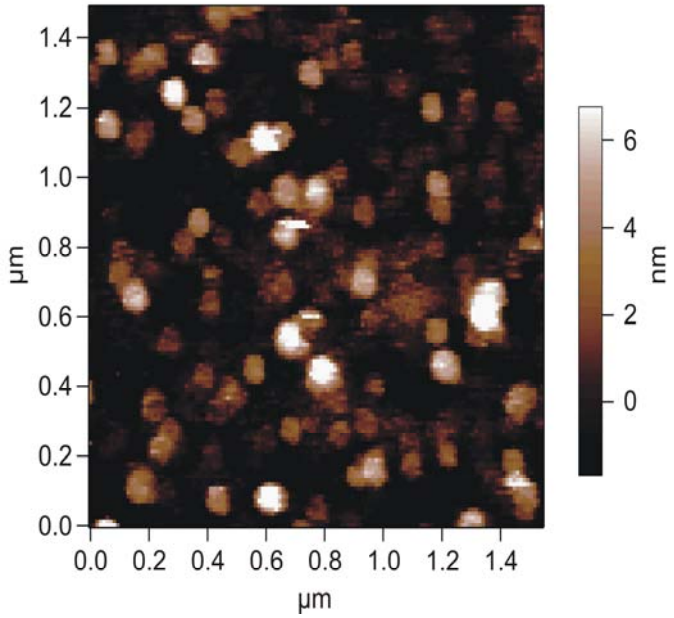

Figure 6.19 Height image of Rubella-like particles onto a glass substrate in citrate phosphate buffer pH = 7.4 with contact mode.

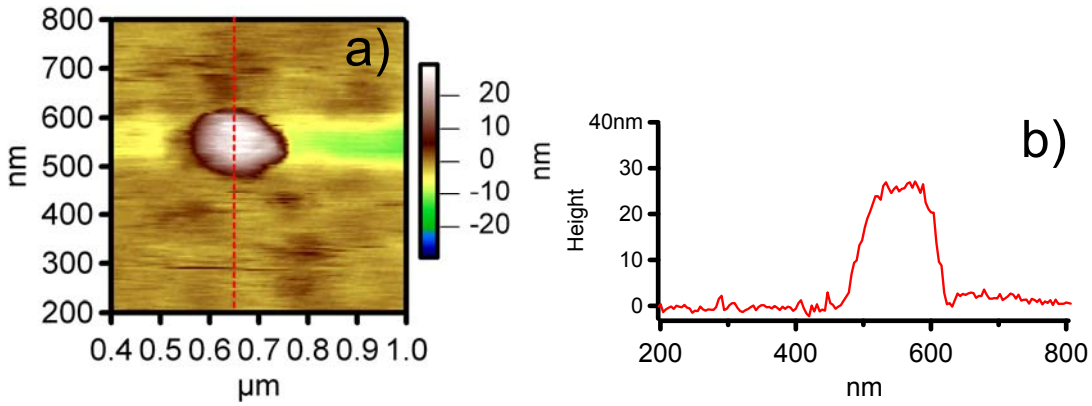

Figure 6.20 Image of a single Rubella VLP onto glass. a) 2D height image. b) Cross section profile.

The average height and diameter taken from 50 different RLPs were 23.5 ± 0.7 and 165.2 ± 4.3 nm, respectively. The diameter was taken from the profile as the width at half maximum height. These considerable differences between height and width are not consistent with an approximately spherical particle that one would expect to observe. There are three possible reasons for this finding. i) Adhesion of the VLPs to the glass may have flattened them. ii) Scanning by the conical tip will overestimate the diameter of the imaged object. iii) In order to obtain an image by AFM, one has to apply a force to the sample. Thus, VLPs will be always flattened during imaging as the result of the applied normal forces during imaging. We assumed force-induced flattening is the major cause for the observed small height. Furthermore flattening may also have occurred due to adhesion of the VLP to the substrate. Because of the ratio in radius size between AFM tip (~15 nm) to VLP (~ 35 nm), convolution is expected to occur. This would increase the width of the particles, but not their measured height. Therefore, even when imaging with the minimum loading force F_M which induced normal forces of about 15 -30 pN, the VLPs were considerably deformed.

In figure 6.20 a high resolution image of a VLP can be appreciated with its cross section profile. Morphological features of the envelope at the surface of the VLP

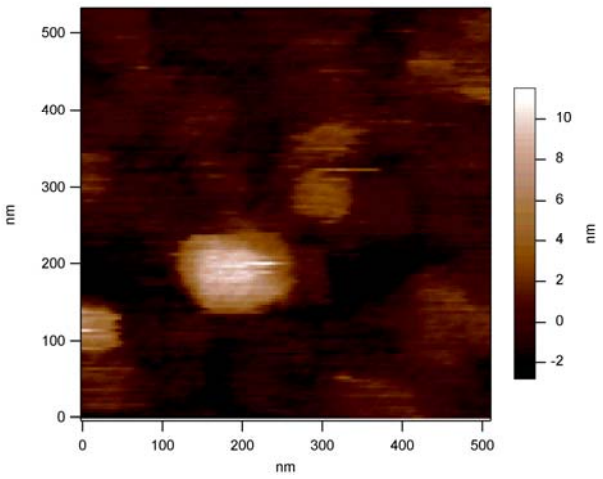

Figure 6.21 Height image of a broken capsid of a Rubella-like particle.

cannot be distinguished. In this image the VLP is flattened to about 30 nm, which is about half of the original particle size. This indicates that the mechanical properties of the Rubella VLPs shortly influence on imaging. A similar situation has been observed with liposomes where it was found that their recorded height value strongly depended on the applied force during imaging [216]. Contrarily, reduction of the loading force below ≈ 15 pN led to a loss of contact between the tip and the VLP.

To date the capsid of Rubella has not been characterized by other high resolution experimental techniques and the organization of the proteins subunits is still unclear.

Although rare, we also obtained images of internal structural components of the Rubella VLPs, like its capsid. This normally occurred, following envelope disruption with the AFM tip during imaging. Figure 6.21 shows a broken Rubella capsid surrounded by some debris. It can be observed that individual capsomers at the surface display an hexagonal protein arrangement, similar to those observed in other Alphaviruses like Semliki forest virus and Sindbis virus [217]. Molecular resolution by AFM imaging was achieved. The capsomers had a size of about 5-12 nm and could be clearly resolved. The pattern at the surface of the capsid matches

the protein organization of a T = 3 structure in the Caspar & Klug picture. The orientation of the capsid seems to be in a threefold axis of symmetry (see figure 6.3b).

6.5.2 Force measurements in neutral and acidic pH

The former procedure was followed in order to investigate the reversibility of possible structural transitions that the VLP undergoes during acidification which could be reflected in changes of their mechanical properties. This might be later related to the process of infection of Rubella virus. The mechanical response of Rubella-like particles was probed by means of nanoindentations at neutral pH 7.4, after exposure to pH 5.0 and, finally after transfer back to neutral pH.

Two different force protocols were applied. First, the elasticity of the VLPs was probed by very small loading forces < 100 pN applied along the vertical axis through nanoindentations. Subsequently, the mechanical strength of the VLPs was probed by application of loads up to 2 nN, to account for the maximal structural strength that the VLP could withstand.

Figure 6.22 displays a typical force-separation curve obtained when Rubella VLPs were indented. In the main graph, only the approach curves in case of small (light blue) and large indentations (dark blue) of a single VLP are shown, presented together with a control curve (black curve) taken next to the particle. About 5 distinct regions along the curve can be distinguished. As long as the AFM tip did not come into contact with the sample, thermal fluctuations of the environment induce vertical deflections on the cantilever in the order of 8 pN on average (region 1). A 10 pN force was taken as the criterion of contact of the tip with the VLP. After contact had been established, an initial linear region in the force curve was observed (region 2). If sufficiently small loading forces were applied the elastic behaviour within region 2 was reproducible (light blue). The distance travelled by the AFM tip within this reversible region of compression was usually 10 -12 nm.

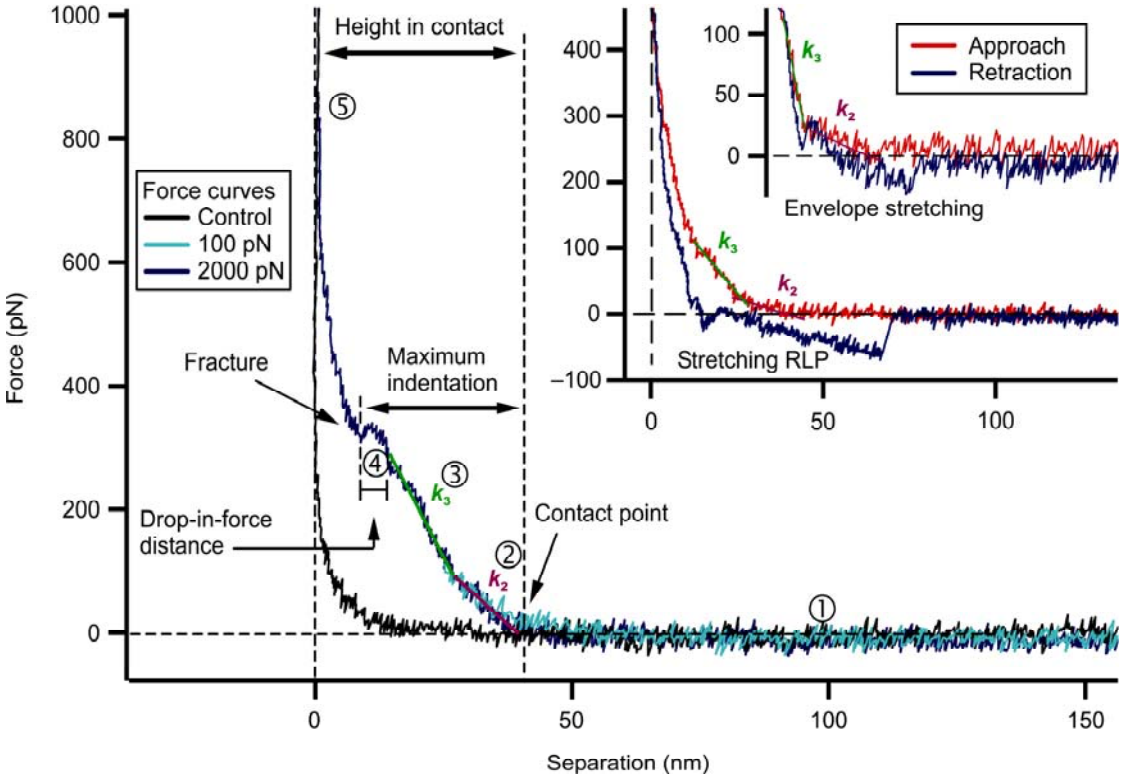

Figure 6.22 Typical force-separation curves for small and large indentations on RLPs. A) Approach curves with different final loads together with control. The numbers denote different characteristics described in the text. B) Approach-retraction curve for small loading forces. C) Approach-retraction curve for 2 nN indentation. In B and C, stretching of the RLP during retraction is observed.

For loads of roughly 100–300 pN, a second linear region with a steeper slope, was observed (region 3). This second slope k_3 was observed in all measurements even though in a few cases the first slope k_2 was not observed. We attribute the presence of a first slope to the force response taken initially after contact by the lipid envelope of the VLP, while the second slope is related to the simultaneous compression of the envelope and capsid. In some occasions the force response of these different structural components overlapped making it difficult to discern the limits of their contribution to the force response, and resulting in a nonlinear force response. However, the origin of these two slopes is discussed below. Further increase of the load usually produced a non-linear response and in some cases lead to a drop in the force (region 4).

Eventually, the curve that trapped the VLP reached an infinite slope (region 5) where the tip cannot further compress. As previously described in section 6.3, a linear fit was applied to those regions in the force curve where a linear force response was observed. In figure 6.22 the respective regions are depicted as k_2 and k_3. The insets of Fig. 6.22 show corresponding details of the approach (red) and retraction (blue) curves. In the approach curves the moderate increase in force response occurs in a linear fashion for slight compression loads. An interesting pattern emerged in the retraction curves where two pull-offs during retraction have been detected. They were separated by a linear region with a slope similar to k_2 of the approach curve. This linear behaviour continued noticeably beyond the contact point, indicating that the Rubella VLP or parts of it remained attached to the tip and was stretched as the tip withdraws.

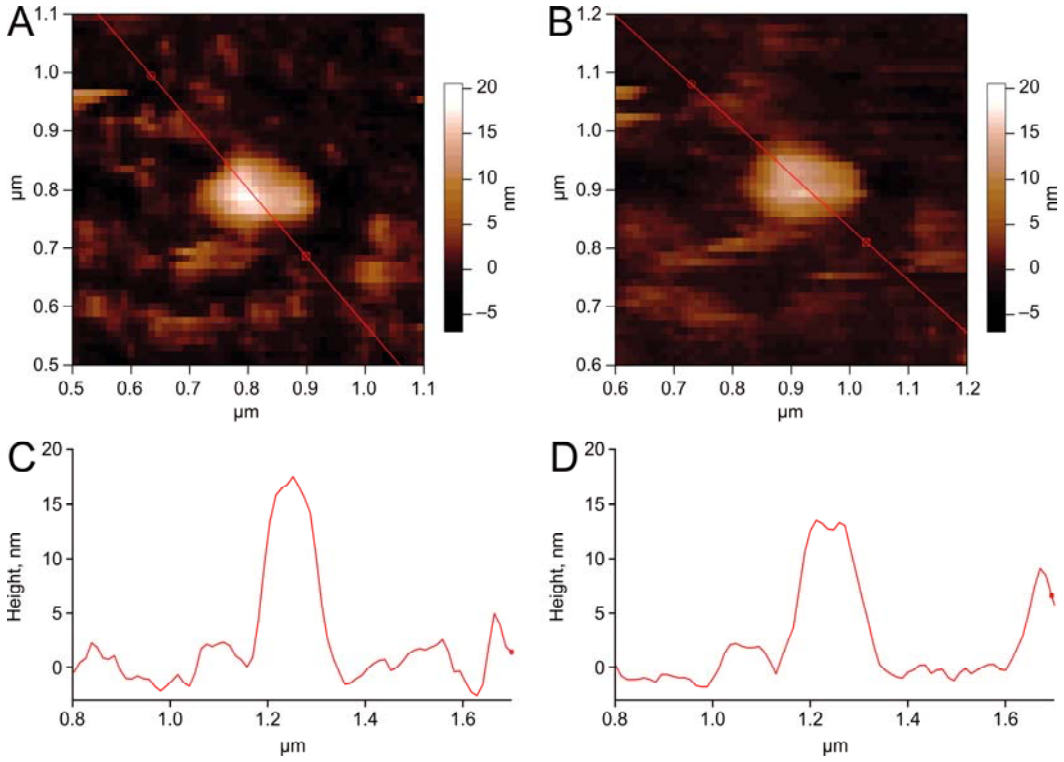

Figure 6.23 Images and profiles before and after indentation on a single VLP. A) Image of a selected Rubella VLP in contact mode before indentation. B) Image of the same VLP after a 2 nN indentation was performed. C) Cross section profile before and D) after indentation.

In a few occasions it was possible to image the VLP before and after performing the indentation as shown in figure 6.23. From this image and its profile shown in C and D, is obvious the nanoindentation was performed in the centre of the particle. A clear inverted shape or concavity appears in the surface of the VLP, indicating that the particle has been permanently damaged and did not fully recover.

In neutral pH, about 60 % of the obtained force curves, showed this two slopes following contact with the tip. In about 30% of the investigated VLPs, the second linear force response was followed by a sudden drop in the force, indicating that a failure occurred. In most cases, after this drop in the force, the curve lost its linear behaviour and its slope changed drastically becoming similar to the response of a hard surface.

Repetitive indentations on Rubella VLPs with a 2 nN loading force lead to an immediate loss of the initial forces response. The shape of the force curves after a second compression normally showed a dramatic reduction in the slope, indicating that the VLP have suffered internal structural damage. This demonstrated that Rubella VLPs did not present a reversible elastic behaviour at high loading forces.

In several occasions, tethers appeared during withdrawal of the tip. In such cases, further indentations on the same VLP showed exceptional features consistent with contamination of the tip.

Figure 6.24 show representative force-separation curves for the case of neutral pH = 7.4 in a) and acidic pH = 5.0 in b). Three major differences can be noticed. First, contrary to the curves taken in neutral pH, the curves taken in acidic pH showed only a single slope after the initial point of contact. Second, the slopes are steeper in low pH, meaning that the VLPs became stiffer upon compression, and larger forces were required for deformation. Third, the maximal loading force required to cause irreversible structural damage increased from a range of 300 - 350 pN for

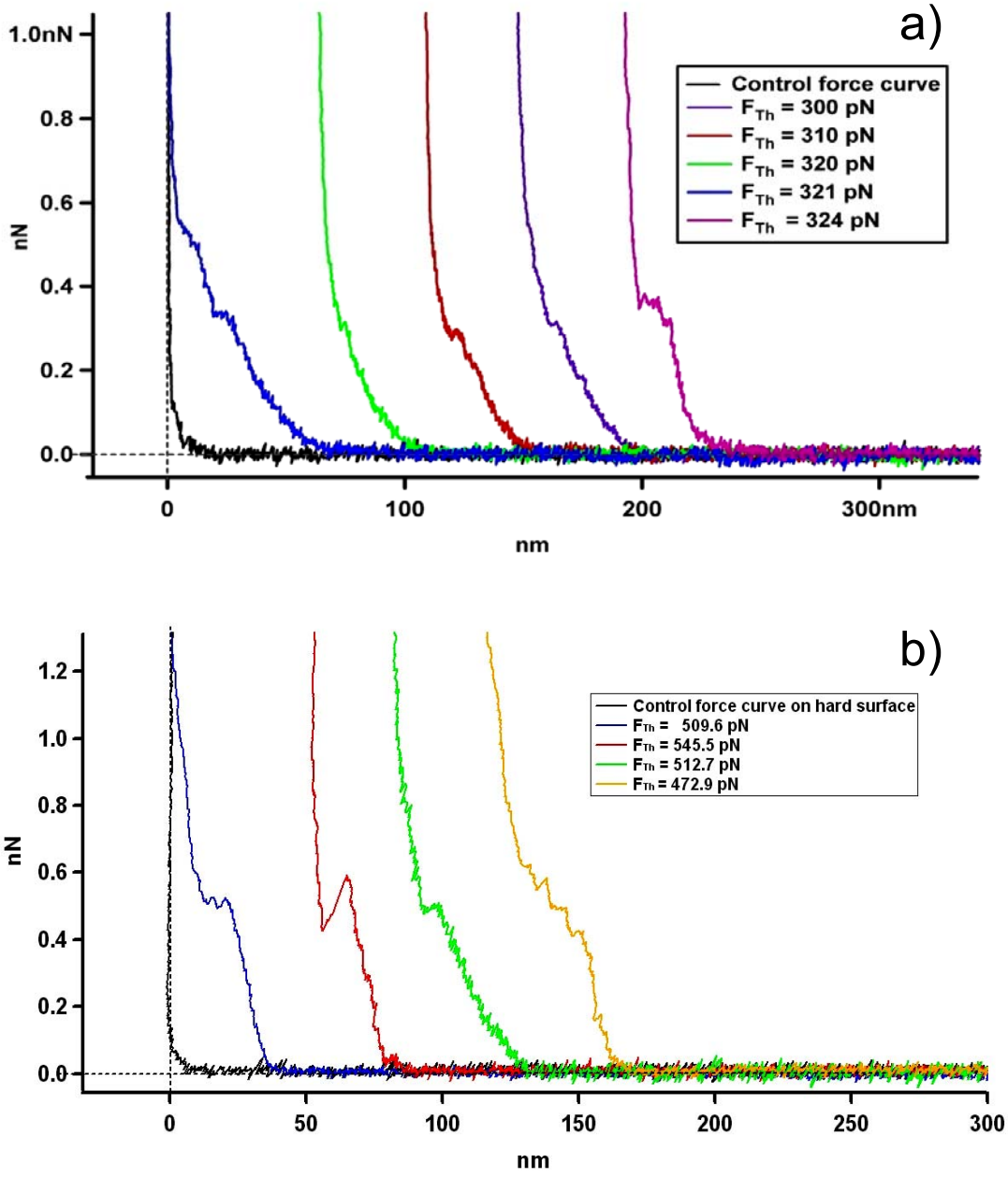

Figure 6.24 Representative force-separation curves for the case of a) neutral pH, and b) acidic pH.

the case of neutral pH, to 470 – 550 pN for acidic pH. Also, the shape of the force curves during a failure changed more drastically in low pH as compared with the neutral pH. Repetitive indentations onto Rubella-like particles showed that in neutral and acidic pH only the low regime of loading forces (<150 pN) provided a fully elastic and reversible force response. For larger compressions of up to 2nN

the particles suffer irreversible structural damage and did not fully recover. To observe if the possible internal structural changes that Rubella VLPs could suffer when changing from neutral to acidic pH were reversible, the VLPs were transferred back into neutral pH. Nanoindentations were performed. The observed behaviour was intermediate between that observed at in neutral pH and acidic pH (data not shown). Hence the pH – induced changes were not fully reversible.

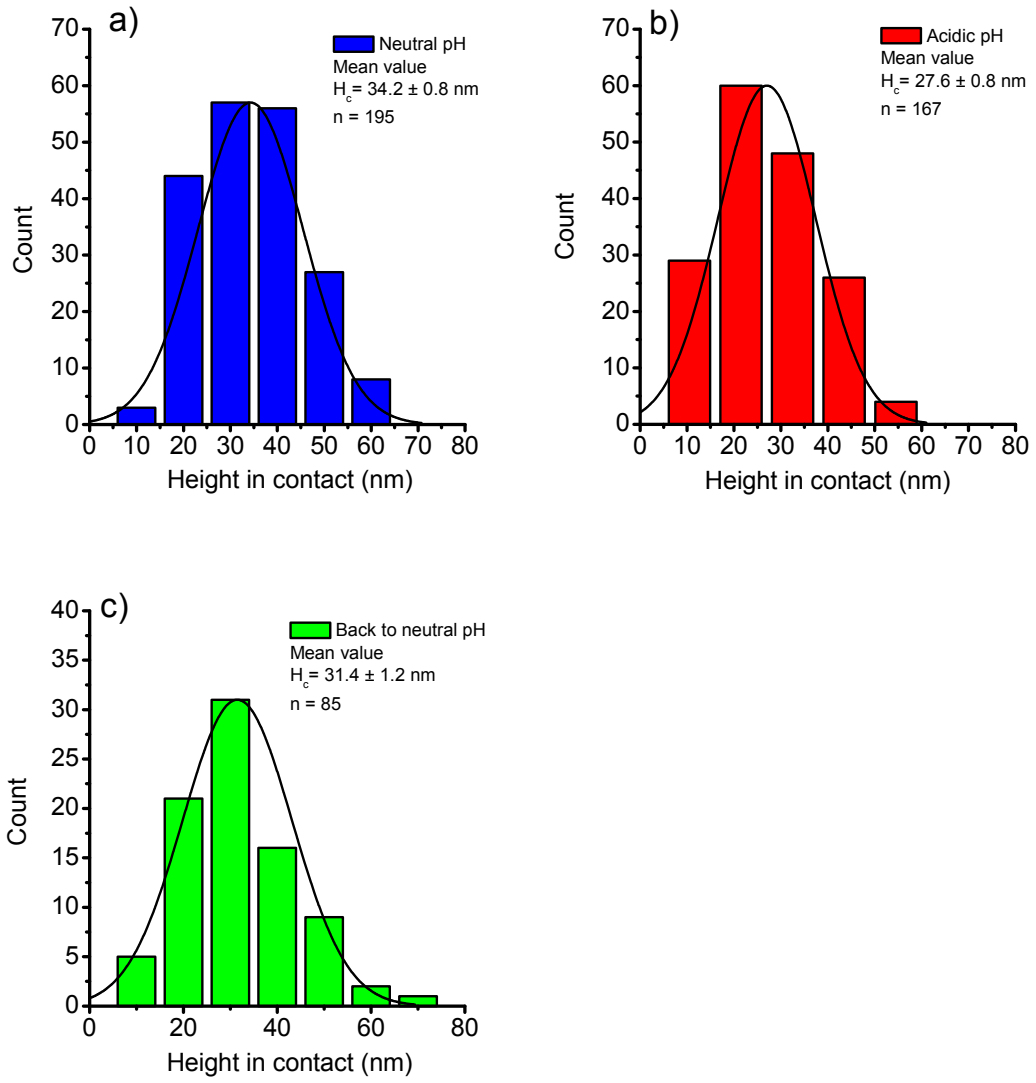

Figure 6.25 Histograms for the height in contact H_c after 2 nN indentations of Rubella VLPs.

An alternative approach to account for the size of the Rubella VLPs was through their height in contact H_c. As before with the Norovirus-like particles, we define the "height in contact" as the distance travelled by the tip in first contact until the full compression of a Rubella VLP (region 5 in figure 6.22). Since the VLPs were very sensible to shear forces during imaging and prone to deformation by the AFM tip, the height in contact seems to be a more reliable parameter for estimation of their size. Figure 6.25 show histograms for the obtained H_c for each case. Gaussian-like distributions were obtained for H_c in neutral and acidic pH as well as after transfer back to neutral pH. Rubella VLPs in solution have a diameter of about 60 nm. However, if attached onto a surface, certain reduction on size due adhesion is expected to occur and the VLP height with respect to the surface will be smaller than its diameter when in solution. The true VLP height should be larger than H_C due the remaining compressed material between the tip and the support. The latter includes the capsid, the lipid membrane, and the spike proteins in a flattened state. One could then make an estimation of the VLP true height H_R when attached to the substrate with $H_R = H_c + 2\Delta$, where Δ is the distance occupied by the lipid envelope and capsid wall thickness in a compressed state.

The compressibility of the lipid membrane itself is too low to yield a noticeable compression. The envelope could in fact be deformed, but is unlikely that the AFM tip can puncture through it under such loading forces. A similar reasoning should be true for the compression of a capsid wall, as in the case of a flattened capsid. If we assume that a protein decorated lipid bilayer in a compressed state occupy a space of Δ = 9 nm (bilayer = 5 nm + compressed spike proteins = 4 nm), and taking a capsid wall thickness of 4 nm from structurally similar Alphavirus [218], using the mean value given in histogram a) in figure 6.24, we then obtain a value of 60 nm for the real height of the Rubella VLP. This obtained value for the size of a VLP is in agreement with studies devoted to the morphological characterization of RV where the diameter was measured by electron microscopy.

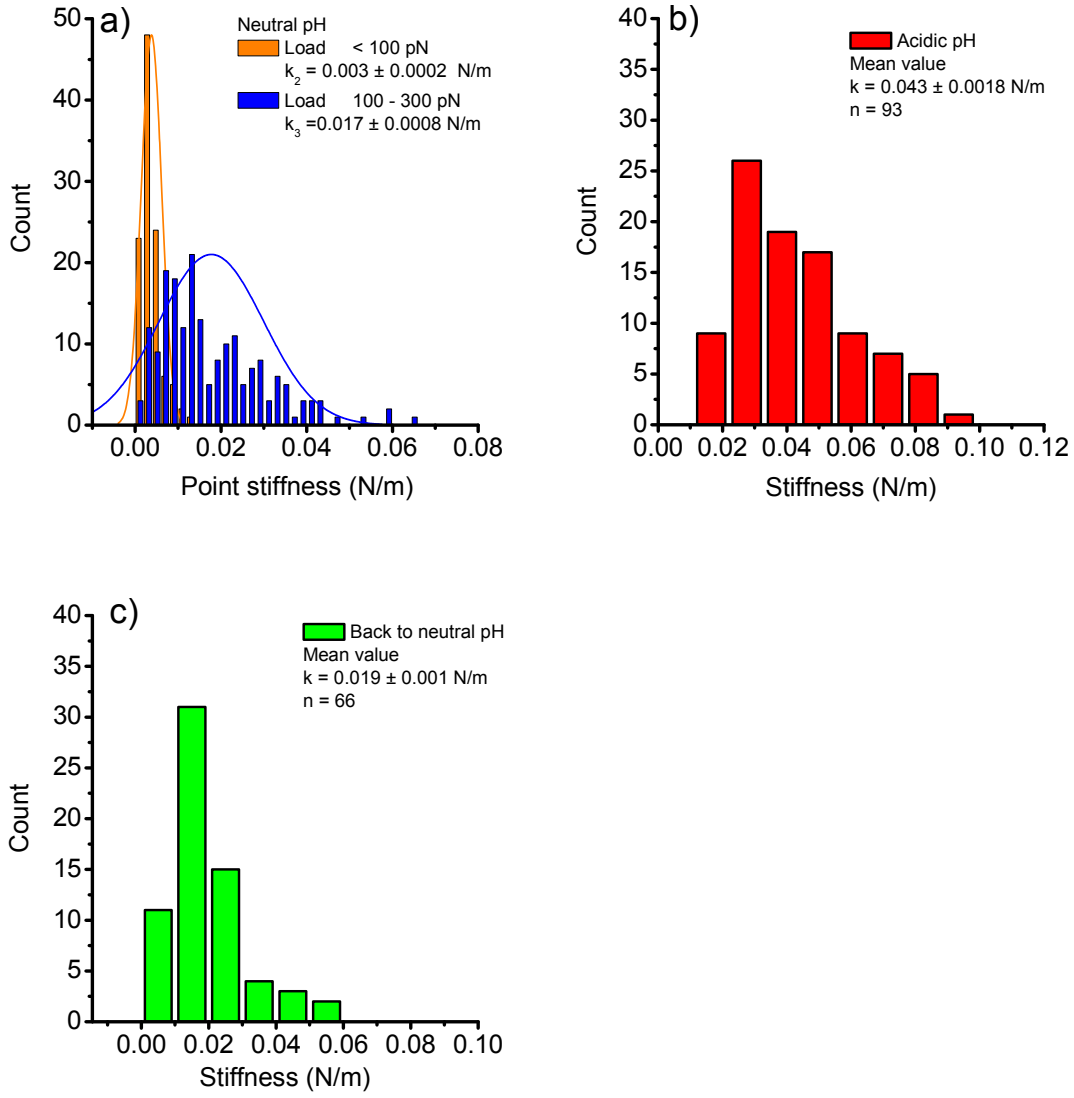

Figure 6.25 Histograms for the capsid stiffness at a) neutral, b) acidic and c) back to neutral.

From the H_c data, an interesting finding was that the change in pH from neutral to acidic induced an apparent *"contraction"* in the VLP. This can be observed in figure 6.24 from the histograms as the centre of the distribution in a) is clearly shifted to the left in b). The mean value for the H_c decreased from 34 nm in neutral to 27 nm in acidic pH. This remarkable change in the size of the particle was reversible, as can be observed in the histogram in c) after the VLPs were exposed back to neutral pH. For this case a value of 31 nm was obtained. As noticed before in

figure 6.22, the compression of Rubella VLPs in neutral pH frequently yielded two linear regions in the force response during compression. These two force responses are regarded as the mechanical behaviour in the linear elastic regime of deformation described by Hooke's law.

Figure 6.25 show histograms for the obtained values of capsid stiffness k for each investigated case of pH.

To obtain the spring constant of the Rubella VLP particles or their stiffness k, the approach described in section 6.3 was followed.

This requires a more detailed consideration under physical grounds which is provided in the following section. The distributions for both regimes of loading force are shown in figure 6.25a). The calculated spring constants for k_2 and k_3 were 0.003 ± 0.0002 and 0.017 ± 0.0008 N/m for n = 108 and n = 197 respectively. While most of the values for k_2 gathered around the mean value, the distribution for k_3 is broad. As shown in figure 6.25b), in acidic pH, the measured Rubella VLP stiffness peaked at a mean value of 0.04 ± 0.003 N /m, which implies that the particles became four-fold stiffer in comparison with the most frequent distribution at neutral pH.

When returned back into neutral pH, the VLPs became again soft like in neutral. Figure 6.26 shows two representative force vs indentation curves in acidic and neutral pH. It is obvious that the forces vs. indentation curves are very different at these different pH values.

The Rubella VLP undergoes a clear "*hardening"* when changing from neutral to acidic environment. Indentation grows in a nonlinear manner in neutral pH, while a linear dependence is observed for acidic pH values. Fits have been included in the graphs only for sake of comparison of the indentation behaviour.

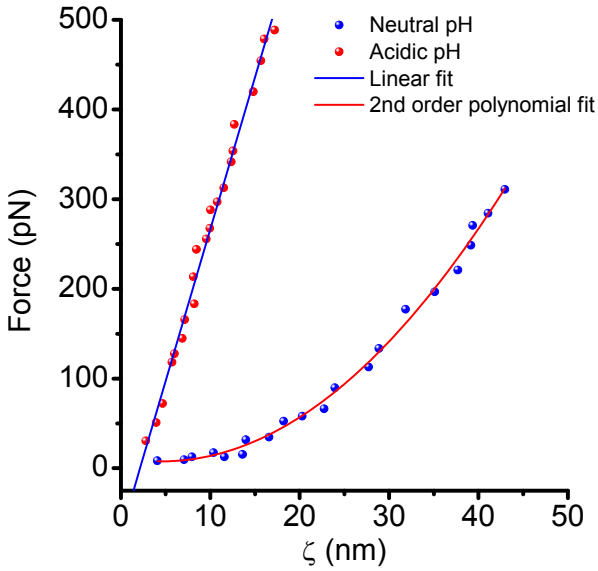

Figure 6.26 Force vs indentation curves for Rubella-like particles in neutral and acidic pH. A clear change in the induced indentation occurs as a function of the applied load.

The existence of two subsequent linear force regimes during particle compression in neutral deserves special consideration. If the VLP can be described as a solid-core shell, composed by the capsid and an elastic shell, the envelope. Any force applied to such a body from outside would immediately be transferred to both, the shell and the core. In this case only one combined nonlinear response regime should be observed.

The experimental observation of two linear regimes can only be explained, assuming that the force applied to the envelope does not lead to capsid deformation. This is only possible if, the stress inside the VLP is isotropic. For this, the material between the envelope and the capsid, called the matrix, shows a fluid-like behaviour and redistribute accordingly if the VLP is indented. Only if the interior surface of the envelope gets finally into contact with the capsid, the latter would start to deform, and, the system switch to a different mode of elastic response.

Consequently during the initial state of compression, the load induced by the AFM tip is taken by the lipid envelope and the capsid core is not affected. The pressure in the matrix increases and eventually water is squeezed out from the matrix. At a force of 100 pN the pressure increase is of the order of 4.4×10^5 bar which is in the range of physiological osmotic pressures. Therefore, the first regime of deformation may contain membrane bending and osmotic work.

The matrix is probably a protein network. The mechanical properties of the matrix are unknown. Morphological studies of Rubella virus have shown that there is a considerable space between the envelope and the capsid. It is unclear if there is a strong interaction between the capsid proteins and the inner protrusions of the fusion proteins E_1 and E_2.

The first slope stretches over about 10-12 nm, suggesting that is likely that indentation with the AFM tip bends the envelope inwardly up to a point where its inner surface comes into direct contact with the outer wall of the capsid.

At hits point the force will be consequently transmitted from the envelope to the capsid. The observed force response (k_3 in figure 6.22) we believe can be related to the compression of the capsid as well as to further osmotic work. Further compression will lead to the point where the inner walls of the empty capsid touch each other and the tip encounters an incompressible surface.

The resulting spring constants for both regimes of compression in neutral pH are significantly smaller than those found in other studies of empty viruses. The different orientations the capsid could adopt during compression, could explain the broad distribution found for the stiffness in k_3. The fully reversible mechanical response obtained at very small indentation depths, provided an exceptional low value for k_2 of 0.003 N/m. This weak force response appeared for compressions of up to 17 % of the Rubella VLP size.

Our assumption that the initial force response corresponds to bending of the envelope by the AFM tip is reinforced by the next argument. The distance of

compression by the tip over the first slope seems to match the available space of the lumen inside the VLP. Considering a Rubella VLP size of 60 nm, a capsid external diameter of 35 nm and an envelope thickness of 5 nm [218, 219]. We obtain an available distance of compression of 15 nm. This distance is in agreement with the measured compression range for k_2.

The second slope, although steeper, also shows comparatively a low spring constant. To the best of our knowledge, empty viral particles with such soft properties as observed in this study have yet not been reported.

Recently the reconstituted viral envelope of Influenza virus has been studied by AFM nanoindentations [220]. Mean values of 0.019 - 0.027N/m and 0.61 - 1.13 x 10^{-19} J were reported for the spring constant k and the bending rigidity κ respectively for the range of temperatures 13 - 17^{o} C. Forces of about 0.88 nN were necessary to puncture the envelope. Is interesting to notice that these reported results are very similar to the value obtained for Rubella VLP when applying higher loads (k_3 = 0.017 N/m). Furthermore, the same team investigated the mechanical properties of the Influenza virus itself and obtained a spring constant of 0.04 N/m [221]. It was concluded that the soft response of the virus was dominated by the envelope.

The only other enveloped viruses studied so far by nanoindentations are the HIV virus and murine Leukemia (LMV) virus [139, 140]. The particle stiffness was in both cases larger than 0.2 N/m. A separate contribution of the envelope was not observed. The obtained stiffness for HIV and LMV are at least 11-fold stiffer than Rubella VLPs in neutral pH and 5-fold stiffer for the case of low pH. A physiological related change of force – indentation curves were obtained for the LMV, where the indentation as a function of the applied loading force changes from a nonlinear behaviour in the immature state of the virus, into a linear behaviour when the virus experiences a maturation process. A finite element calculation allowed to conclude that for the range of small loading forces, the observed linear response is characteristic for a thin shell structure while a nonlinear behaviour is expected for a

thicker shell. During compression of a thick shell, the applied deformation spreads throughout the equator of the spherical shell into an increasing volume of material.

30 % of the total amount of investigated Rubella VLPs showed a fracture event upon indentation at high loading forces. Approach curves without a drop in the force displayed a sudden increase of their slope just before the hard surface was felt. Fracture usually occurred at indentations of 53–62 % of the VLP diameter. This critical indentation is larger compared to that found in previous studies. At the same time, the drop in force is smaller than with other viruses, but increased considerably when tested in low pH. Therefore this could indicate that in acidic pH, the Rubella VLP would suffer an internal structural transition which modifies its intrinsic material properties. The presence of a single defined linear slope immediately after contact in acidic pH, followed by a sudden failure in the force response could indicate that the particle changes from a soft fluffy state in neutral, to a thick shelled structure under acidic conditions.

Regarding the nature of the failure upon high loading forces the following mechanism is suggested.

One possibility is that the observed fracture events reflect the mechanical failure of the enclosed capsid. This suggestion is made based on the fact that the fractures in the force curves appeared in most cases for loads above 200 pN, indicating that not only the envelope but also the capsid were already under compression at this point. The pressure increase naturally induces an increase in the membrane tension. Therefore, it could be ruled out that membrane rupture may contribute to the observed failure. However, rupture should at the equatorial plane, which would not result in a sudden distance change upon rupture. The forces required to puncture a lipid bilayer after being entirely flattened are simply too large, being above 2 - 4 nN.

The capsid may fail at different sites depending on how the forces are distributed over the VLP. This explains the distribution of rupture forces.

This should be preferably the case if the size of the tip is smaller than the capsid diameter. According to specifications, the radius of the tip is known to be smaller than 20 nm. This means that the tip is about the size of the capsid. However, the forces between tip and capsid are modulated by the envelope. The envelope would then serve as a first contact barrier to absorb the impact of the tip and to spread the forces throughout the entire VLP. This would increase the area of compression even more. This lead us to argue that buckling and puncture are both unlikely to occur, because the ratio indentor-capsid does not allow to apply such point forces to probe individual capsomers neither to interpenetrate through the protein subunits. We believe that equatorial failure is more likely to occur because the indentations that have been performed here are large in comparison to the size of the capsid.

6.5.3 Influence of material properties of Rubella VLPs on RV life cycle

The mechanical characterization of Rubella VLPs presented in this study, were performed under conditions which mimic the natural entry pathway of Rubella virus into cells. The acidic environment in the late endosome following endocytosis by the Rubella virus triggers an irreversible conformational transition in the virus spike proteins [202]. The structural change in the spike proteins leads to the formation of a pore between the viral membrane and the endosome, which finally ends in the release of the capsid and its cargo into the cytoplasm [203].

Rubella VLPs turned out to be quite soft in neutral pH. The lack of genome inside the capsid, is however, expected to have a direct influence on the measured low stiffness.

One important difference between Rubella and the Alphaviruses family is the mechanism of virus assembly. Virus formation in alphaviruses takes place in the cytoplasm when the preassembled capsid attaches to the lower side of the spike proteins by a specific strong interaction. Following attachment, the process of budding allows the release of the new formed virions out the cell.

On the contrary, Rubella capsid assembly occurs concomitant or posterior within Cisternae vesicles in Golgi membranes [222]. Therefore, this could mean that the capsomer-capsomer interactions and require membrane assistance for their successful assembly. This difference in the formation of the virus may account for the observed pronounced softness of Rubella VLPs in neutral pH.

Nanoindentation measurements on Rubella VLPs yielded three main results concerning the particle mechanical properties when changing from neutral pH 7.4, to pH 5.0.

a) A different behaviour in the observed force response during indentation.

b) A marked increase in the stiffness of the particle after exposure to low pH.

c) An apparent reduction in size of the VLP in acidic pH.

The following arguments could be responsible for the observed changes.

I) Fusion proteins-capsid interaction. The experimental evidence concerning a pH dependency of Rubella virus is the conformational transition of the envelope glycoprotein E_1 triggered by low pH, as have already been reported by Katow [203]. An acidic environment induces a molecular extension of this fusion peptide and promotes its insertion within the opposite membrane. So for the latter case, it is possible that the mentioned conformational transition would induce a reduction of the distance between envelope and capsid. This line of reasoning is supported by the fact that the shape of the force curves in acidic pH did not show any sign of resistance which could be attributed to the envelope alone. Instead, *"hardening"* is observed from the initial point of contact onwards. So, at low pH the VLP acts as one entity and not as two decoupled springs. Hence, a strong interaction between inner spike proteins and the capsid caused by an internal conformational transition in low pH could explain the obtained results.

II) Osmotic pressure. If the change of pH causes a decrease in the osmotic pressure of the matrix material due to aggregation or condensation, water will be diffused out of the envelope and the VLP will shrink as a whole.

III) Capsid structural transition. Finally, the capsid itself could possess an inherent pH responsiveness, similar to the observed irreversible contraction of Semliki Forest virus capsid in acidic pH [176].

Figure 6.27 shows a schematic representation of the proposed hardening mechanisms.

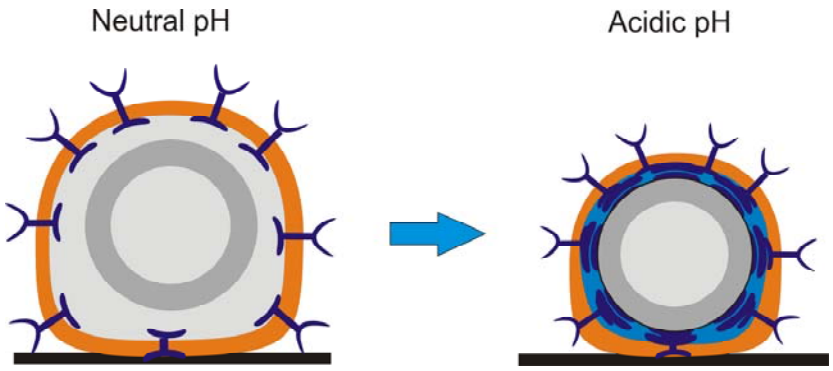

Figure 6.27 Schematic representation of internal structural transitions that the Rubella VLPs could suffer when exposed to acidic pH. As shown by the arrows, a conformational transition by the capsid, or by the inner part of the spike proteins establish a direct connection between both. The final state is a hard and more compacted particle.

Identification of the precise structural constituents causing such contraction in Rubella virus requires further investigations.

Another upcoming yet open question is, of whether and how the observed stiffness and size changes are related to fusion and release of the viral genome.

To date, the fate of the capsid and its content after the process of viral fusion remains unclear. It is not known if the capsid is disassembled afterwards or if is transported to a specific site inside the cell for posterior disassembly, or if it

proceeds by association with external proteins. Or, if the capsid swells releasing its nucleic acid through opening pores formed between capsomer units. The author of an study on the solubility of Rubella capsid have suggested that exposure of Rubella virus in acidic conditions is enough to initiate uncoating within the endosome [205].

From our results, based merely on the change in the mechanical properties of Rubella-like particles, we propose the following mechanism of cargo delivery for the Rubella virus. We consider that an acidic environment induces an internal conformational transition leading to a strong interaction between the capsid protein and the inner surface of the envelope. The capsid and the envelope are tightly bound. Simultaneously, driven by low pH, the activation of the spike proteins E_1 on the surface of the virus initiate the process of viral fusion by opening a connecting pore with the membrane of the endosome.

We propose that the capsid protein remain strongly attached to the envelope and get disrupted during the process of viral fusion as membrane tension will be transmitted to the envelope.

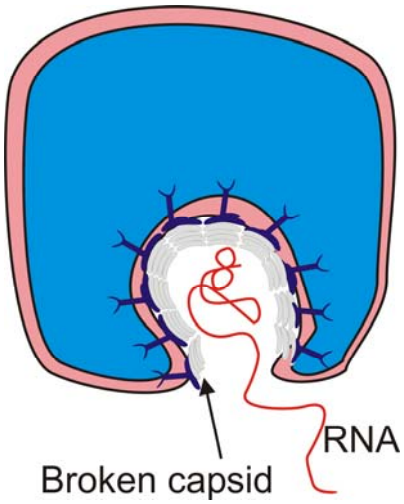

Figure 6.28 Proposed model of genome release by the Rubella virus. The capsid of Rubella virus gets tightly bound with the interior part of the envelope as a consequence of acidification. The capsid is destroyed promoted by the concomitant process of viral membrane fusion.

In such a way, unwrapping would not lead to the final delivery of intact capsids into the cytoplasm but rather to the direct release of the genome at the moment of escape from the endosome. This mechanism of cargo release is sketched in figure 6.28. The proposed scenario is based on the presented mechanistic studies of Rubella VLPs. Further studies are required to verify the proposed model of cargo delivery. Experiments on isolated empty Rubella capsids could allow identifying the origin of the increased stiffness and apparent contraction.

6.5.4 Conclusions

The work presented in this study concerned the mechanical properties of Rubella-like particles probed by AFM nanoindentations. The envelope of these VLPs is fully functional with regard to the mechanism of membrane fusion, being the key event of cell infection. Therefore, we believe that our findings may contribute to the general understanding of the mechanical properties of viruses with regard to membrane interaction processes occurring during infection.

Morphological characterization of VLPs by Atomic Force Microscopy showed that Rubella VLPs are very soft and easily deformable by the imaging process even when small loading forces in the order of 50 pN were applied.

When probing individual Rubella VLPs by nanoindentations in neutral pH 7.4, two linear force responses were identified for different regimes of compression. For the first regime of compression forces below 100 pN produced a shallow but linear force response which we attributed to deformation of the envelope structure itself. Thus, the envelope response was characterized by a very low spring constant of about 0.003 N/m. Higher loads of 100 - 300 pN, provided a second linear force response which was considered to account for the simultaneous compression of envelope and capsid. A mean spring constant of 0.017 N/m was found. A nonlinear behaviour was observed in the indentation as a function of the loading force.

Loading forces of 300 – 350 pN were required to induce a fracture or crack in the compressed VLP.

One of the principal findings of this work is that Rubella VLPs suffer an internal structural transition when exposed to acidic conditions of pH 5.0. This is reflected by a two-fold increase in the particle spring constant from 0.017 in neutral pH to 0.04 N/m in acidic pH. This internal structural transition in the VLP is also reflected in the change of the dependence of the indentation with the applied loading force, from a nonlinear behaviour observed in neutral pH, into a linear when changing to acidic pH. This hardening was accompanied by reduction of size of VLP.

From our discussion, a model for the mechanism of genome release during the process of infection by Rubella virus is proposed.

7. Summary & Outlook

The work presented here has a multidisciplinary character, having as a common factor the characterization of soft matter self-assembled nanostructures by means of Atomic Force Microscopy (AFM). AFM was employed to explore the building principles, the stability and the mechanical properties of three different systems: Virus-Like particles (VLPs), polyelectrolyte – lipid nanocomposites and polyelectrolyte brushes. All these systems are assembled from polyelectrolytes alone or in combination with lipids.

The interaction between a polyelectrolyte multilayer support and a lipid layer was studied at the single molecular level by force spectroscopy. Single molecule adsorption/desorption experiments were conducted between Poly(allyl amine) hydrochloride (PAH) attached to an AFM tip and lipid coated surfaces. Adsorption on approach as well as desorption of single chains on retraction were monitored with AFM. In this way, the binding interaction between PAH and Phosphatidylserine and Phosphatidylcholine as well with an equimolar mixture of both lipids were investigated. The results were compared with the desorption behavior on glass. It was found that adsorption of polyelectrolyte chains on fluid lipid membranes involves tangential transport of the adsorbed chain off the site of adsorption. This ensured the consecutive deposition of long chains on fluid lipid membranes.

This mechanism leads to an equilibrium chain pulling force on adsorption. This system can be considered as an element of a nanomachine. If the external pulling force is lowered below the equilibrium force, the polyelectrolyte chain gets spreads on the surface. Upon increasing the force the chain desorbs in a consecutive fashion. The binding mechanism itself is brought about by the electrostatic attraction and the subsequent formation of hydrogen bonds between the amino group and charged moieties at the lipid headgroups. Entropy increase through

release of bound water molecules and counterions contributes to the strength of binding, which is of the order of a few kT per monomer.

Further experiments in this direction will be devoted to:

- The characterization of the element nanomachine during adsorption.
- Study of the adsorption/desorption behavior for higher ionic strengths.

The change in morphology and the mechanical response of polyelectrolyte brushes was investigated by AFM nanoindentations under different ionic strengths.

The force versus distance curves were modeled with an equation of state of a compressible liquid. This allowed interpreting the behavior at different ionic strength in quantitative terms. The indentation forces depended on ionic strength weaker than expected from Debye theory. This was attributed to lateral and vertical adjustment of the flexible brush molecules as a function of ionic strength. The compressibility of the brush was obtained as a function of penetration depths. It was further shown that imaging proceeds under conditions of penetration of the tip into the brush. The penetration depth itself is a function of the loading force. The application of the model of a compressible liquid allowed defining an equilibrium brush thickness. Measurements with a colloidal probe basically quantify the repulsion behavior of the brush corona, while measurement with an ultrasharp tip probe deeper regions of the brush.

Future experiments in this direction will be devoted to:

- Study of brush compressibility at increasing loading forces with an 8 μm colloid.
- Study of brush compressibility at increasing loading forces with Tapping mode to account for the effect of tip interpenetration.

Finally, viral capsids were investigated. The choice of two unrelated viral systems with different entry pathways into the cell and with different morphological architectures was expected to reveal crucial information about the stability and mechanical resistance to deformation of these empty membrane-coated and bare viral capsids. This provided clues on the stage of particle disassembly and cargo release during the final step of the infection process.

Therefore, the mechanical stability and elastic properties of virus-like particles (VLPs) of Rubella and Norovirus were investigated by external application of loading forces with an AFM tip. The measurements were performed under conditions relevant for the virus infection mechanism.

For Norovirus capsids it was found that these protein shells were mechanically stable by repetitive AFM nanoindentations within a range of pH 2.0 – 7.5. It was observed that repetitive compression of the capsids usually provided an elastic response. However, in some cases the induced mechanical fatigue caused the capsid to fail and fractures were detected. An interesting self-healing mechanism accounted for the noncovalent interactions holding the capsomers together. A relatively constant capsid stiffness of about 0.05 N/m was obtained for pH values of 2.0 - 7.5. Using available theories for continuum mechanics allowed us to estimate the Young´s Moduli of the Norovirus capsid. A value of 30 MPa was obtained. Another major finding was that as the Norovirus capsids were exposed to increasing alkaline conditions the shells became softer and an increase in size was detected. In pH 10, the capsids lost structural stability and were easily destroyed after a single indentation. It is suggested that the soft mode observed at increasing pH values, could represent a structural requirement for capsid disassembly triggered by pH during the process of infection.

Following experiments regarding this topic are expected to:

- Investigate the mechanical properties of Norovirus VLPs under externally imposed osmotic pressures, for instance with Polyethylene glycol solutions.

- Study the mechanical stability of Norovirus VLPs at increasing ionic strengths near the values required for capsid disassembly.

The mechanical properties of empty Rubella viruses were investigated in pH values which correspond to the process of viral membrane fusion. Rubella-like particles were also probed by AFM nanoindentations in neutral 7.4 and acidic pH 5.0. Upon nanoindentations in neutral pH, the envelope, a major constituent of Rubella appear to dominate the force response at small loading forces. However, further compressions showed that up to certain load, concomitant compression of envelope and capsid occur. Therefore, when fully compressed, usually two forces responses were for Rubella VLPs were found.

A value of 0.017 N/m was found for such compression ranges. When switching to low pH, the Rubella VLP response changed, and only one linear force response was observed. The stiffness increased at least two-fold in acidic conditions. It was also observed that the Rubella VLP height was reduced in low pH. The later strongly suggest that, after exposure to low pH, an internal structural transition occurs between the capsid and the inner wall of the envelope, which yields the Rubella VLP in a more compacted state.

It was concluded that genome release occurs at the surface of the endosome as a consequence of the process of viral fusion were the capsid is destroyed.

Experiments in the near future on this topic will be devoted to:

- Characterize the mechanical properties of the wild type rubella virus in order to identify the influence of the genome to the resistance force.
- Study of the capsid morphology of Rubella Virus after separation from the envelope with Triton X. This structural characterization will allow to finally determine the architecture of Rubella virus capsid within the CK classification.

Abbreviations

AFM	-	Atomic Force Microscopy
STM	-	Scanning Tunneling Microscopy
FJC	-	Freely Jointed Chain
WLC	-	Worm Like Chain
VLP	-	Virus Like Particle
RNA	-	Ribonucleic Acid
DNA	-	Desoxiribonucleic Acid
LBL	-	Layer By Layer
PEM	-	Polyelectrolyte Multilayer
PAH	-	Poly(allyl amine) hydrochloride
PSS	-	Poly(styrene sulfonate, Sodium salt)
PolyDADMAC	-	Poly(diallyldimethylammonium chloride)
PE	-	Polyelectrolyte Brush
PSPM	-	Poly(potassium 3 – sulfopropyl methacrylate)
TEM	-	Transmission electron Microscopy
SEM	-	Scanning Electron Microscopy
CMAFM	-	Contact Mode Atomic Force Microscopy
TMAFM	-	Tapping Mode Atomic Force Microscopy
VdW	-	Van der Waals
SMFS	-	Single Molecule Force Spectroscopy
SAM	-	Self Assembled Monolayer
CCMV	-	Cowpea Chlorottic Mottle Virus
MVM	-	Minute Virus of Mice
FEM	-	Finite Element Model

LMV	-	Leukemia Murine Virus
HIV	-	Human Immune Deficiency Virus
POPS	-	Phosphatidylserine
POPC	-	Phosphatidylcholine
ATRP	-	Atom Transfer Radical Polymerization
F_{ML}	-	Minimum Loading Force
H_{eq}	-	Equilibrium Brush Thickness
H_{Dry}	-	Brush Dry Thickness
CK	-	Caspar & Klug
NV	-	Norovirus
RV	-	Rubella Virus
CRS	-	Congenital Rubella Syndrome
BEVS	-	Baculo Virus Expression System
H_m	-	Measured Height
H_c	-	Height in contact
FvK	-	Föppl von Kárman

8. Literature

1. Bishop, K.J.M., et al., *Nanoscale Forces and Their Uses in Self-Assembly.* Small, 2009. **5**(14): p. 1600-1630.
2. Min, Y.J., et al., *The role of interparticle and external forces in nanoparticle assembly.* Nature Materials, 2008. **7**(7): p. 527-538.
3. Grzelczak, M., et al., *Directed Self-Assembly of Nanoparticles.* Acs Nano, 2010. **4**(7): p. 3591-3605.
4. Evans, E. and K. Ritchie, *Dynamic strength of molecular adhesion bonds.* Biophysical Journal, 1997. **72**(4): p. 1541-1555.
5. Singh, P., M.J. Gonzalez, and M. Manchester, *Viruses and their uses in nanotechnology.* Drug Development Research, 2006. **67**(1): p. 23-41.
6. Ferrari, M., *Cancer nanotechnology: Opportunities and challenges.* Nature Reviews Cancer, 2005. **5**(3): p. 161-171.
7. Ashkin, A., et al., *OBSERVATION OF A SINGLE-BEAM GRADIENT FORCE OPTICAL TRAP FOR DIELECTRIC PARTICLES.* Optics Letters, 1986. **11**(5): p. 288-290.
8. Chen, W., et al., *Monitoring Receptor-Ligand Interactions between Surfaces by Thermal Fluctuations.* Biophysical Journal, 2008. **94**(2): p. 694-701.
9. Evans, E., *PROBING THE RELATION BETWEEN FORCE—LIFETIME—AND CHEMISTRY IN SINGLE MOLECULAR BONDS.* Annual Review of Biophysics and Biomolecular Structure, 2001. **30**(1): p. 105-128.
10. Neuman, K.C. and S.M. Block, *Optical trapping.* Review of Scientific Instruments, 2004. **75**(9): p. 2787-2809.
11. Neuman, K.C. and A. Nagy, *Single-molecule force spectroscopy: optical tweezers, magnetic tweezers and atomic force microscopy.* Nat Meth, 2008. **5**(6): p. 491-505.
12. Gerber, C. and H.P. Lang, *How the doors to the nanoworld were opened.* Nat Nano, 2006. **1**(1): p. 3-5.
13. Guck, J., et al., *The optical stretcher - A novel laser tool to micromanipulate cells.* Biophysical Journal, 2001. **80**(1): p. 277A-277A.
14. Marshall, K.L., et al., *Performance of protective polymeric coatings for nonlinear optical materials.* Journal of Applied Physics, 1988. **64**(5): p. 2279-2285.
15. Hugel, T., et al., *Single-Molecule Optomechanical Cycle.* Science, 2002. **296**(5570): p. 1103-1106.
16. Koltover, I., et al., *An Inverted Hexagonal Phase of Cationic Liposome-DNA Complexes Related to DNA Release and Delivery.* Science, 1998. **281**(5373): p. 78-81.
17. Tros de Ilarduya, C., Y. Sun, and N. Düzgüneş, *Gene delivery by lipoplexes and polyplexes.* European Journal of Pharmaceutical Sciences, 2010. **40**(3): p. 159-170.
18. Lv, H., et al., *Toxicity of cationic lipids and cationic polymers in gene delivery.* Journal of Controlled Release, 2006. **114**(1): p. 100-109.
19. Morille, M., et al., *Progress in developing cationic vectors for non-viral systemic gene therapy against cancer.* Biomaterials. **29**(24-25): p. 3477-3496.
20. Czolkos, I., A. Jesorka, and O. Orwar, *Molecular phospholipid films on solid supports.* Soft Matter, 2011. **7**(10): p. 4562-4576.
21. Steven G, B., *Molecular transport and organization in supported lipid membranes.* Current Opinion in Chemical Biology, 2000. **4**(6): p. 704-709.

22. Schönherr, H., et al., *Vesicle Adsorption and Lipid Bilayer Formation on Glass Studied by Atomic Force Microscopy.* Langmuir, 2004. **20**(26): p. 11600-11606.
23. Castellana, E.T. and P.S. Cremer, *Solid-Supported Lipid Bilayers: From Biophysical Studies to Sensor Design.* ChemInform, 2007. **38**(14): p. no-no.
24. Kiessling, V., et al., *Supported Lipid Bilayers*, in *Wiley Encyclopedia of Chemical Biology*. 2007, John Wiley & Sons, Inc.
25. Tamm, L.K. and H.M. McConnell, *Supported phospholipid bilayers.* Biophysical Journal, 1985. **47**(1): p. 105-113.
26. Sackmann, E., *Supported Membranes: Scientific and Practical Applications.* Science, 1996. **271**(5245): p. 43-48.
27. Richter, R.P., R. Bérat, and A.R. Brisson, *Formation of Solid-Supported Lipid Bilayers: An Integrated View.* Langmuir, 2006. **22**(8): p. 3497-3505.
28. Richter, R.P., J.L.K. Him, and A. Brisson, *Supported lipid membranes.* Materials Today, 2003. **6**(11): p. 32-37.
29. Schmitt, J., B. Danner, and T.M. Bayerl, *Polymer Cushions in Supported Phospholipid Bilayers Reduce Significantly the Frictional Drag between Bilayer and Solid Surface.* Langmuir, 2000. **17**(1): p. 244-246.
30. Wong, J.Y., et al., *Polymer-Cushioned Bilayers. I. A Structural Study of Various Preparation Methods Using Neutron Reflectometry.* Biophysical Journal, 1999. **77**(3): p. 1445-1457.
31. Wong, J.Y., et al., *Polymer-Cushioned Bilayers. II. An Investigation of Interaction Forces and Fusion Using the Surface Forces Apparatus.* Biophysical Journal, 1999. **77**(3): p. 1458-1468.
32. Decher, G., *Fuzzy Nanoassemblies: Toward Layered Polymeric Multicomposites.* Science, 1997. **277**(5330): p. 1232-1237.
33. Klitzing, R.v., et al., *Short range interactions in polyelectrolyte multilayers.* Current Opinion in Colloid & Interface Science, 2004. **9**(1–2): p. 158-162.
34. Dejeu, J., et al., *Early steps of the film growth mechanism in self-assembled multilayers of PAH and PSS on silica: Polymer uptake, charge balance and AFM analysis.* Colloids and Surfaces A: Physicochemical and Engineering Aspects, 2006. **288**(1–3): p. 26-35.
35. Popa, I., et al., *Attractive Electrostatic Forces between Identical Colloidal Particles Induced by Adsorbed Polyelectrolytes.* The Journal of Physical Chemistry B, 2009. **113**(25): p. 8458-8461.
36. Donath, E., et al., *Novel Hollow Polymer Shells by Colloid-Templated Assembly of Polyelectrolytes.* Angewandte Chemie International Edition, 1998. **37**(16): p. 2201-2205.
37. Borodina, T., et al., *Polyelectrolyte microcapsules as the systems for delivery of biologically active substances.* Biochemistry (Moscow) Supplemental Series B: Biomedical Chemistry, 2008. **2**(1): p. 88-93.
38. Mauser, T., C. Déjugnat, and G.B. Sukhorukov, *Reversible pH-Dependent Properties of Multilayer Microcapsules Made of Weak Polyelectrolytes.* Macromolecular Rapid Communications, 2004. **25**(20): p. 1781-1785.
39. Shi, X., R.J. Sanedrin, and F. Zhou, *Structural Characterization of Multilayered DNA and Polylysine Composite Films: Influence of Ionic Strength of DNA Solutions on the Extent of DNA Incorporation.* The Journal of Physical Chemistry B, 2002. **106**(6): p. 1173-1180.
40. Reibetanz, U., et al., *Defoliation and Plasmid Delivery with Layer-by-Layer Coated Colloids.* Macromolecular Bioscience, 2006. **6**(2): p. 153-160.
41. Crespo-Biel, O., et al., *Patterned, Hybrid, Multilayer Nanostructures Based on Multivalent Supramolecular Interactions.* Chemistry of Materials, 2006. **18**(10): p. 2545-2551.

42. Kühner, M., R. Tampé, and E. Sackmann, *Lipid mono- and bilayer supported on polymer films: composite polymer-lipid films on solid substrates.* Biophysical Journal, 1994. **67**(1): p. 217-226.
43. Kugler, R. and W. Knoll, *Polyelectrolyte-supported lipid membranes.* Bioelectrochemistry, 2002. **56**(1): p. 175-178.
44. Bunge, A., et al., *Characterization of lipid bilayers adsorbed on spherical LbL-support.* Soft Matter, 2009. **5**(17): p. 3331-3339.
45. Krishna, G., T. Shutava, and Y. Lvov, *Lipid modified polyelectrolyte microcapsules with controlled diffusion.* Chemical Communications, 2005(22): p. 2796-2798.
46. Moya, S., et al., *Lipid Coating on Polyelectrolyte Surface Modified Colloidal Particles and Polyelectrolyte Capsules.* Macromolecules, 2000. **33**(12): p. 4538-4544.
47. Fery, A., et al., *Interaction of polyelectrolyte coated beads with phospholipid vesicles.* Comptes Rendus Physique, 2003. **4**(2): p. 259-264.
48. Ge, L., H. Möhwald, and J. Li, *Polymer-stabilized phospholipid vesicles formed on polyelectrolyte multilayer capsules.* Biochemical and Biophysical Research Communications, 2003. **303**(2): p. 653-659.
49. Sackmann, E. and M. Tanaka, *Supported membranes on soft polymer cushions: fabrication, characterization and applications.* Trends in Biotechnology, 2000. **18**(2): p. 58-64.
50. Fischlechner, M., et al., *Fusion of Enveloped Virus Nanoparticles with Polyelectrolyte-Supported Lipid Membranes for the Design of Bio/Nonbio Interfaces.* Nano Letters, 2007. **7**(11): p. 3540-3546.
51. Fischlechner, M., et al., *Engineering Virus Functionalities on Colloidal Polyelectrolyte Lipid Composites.* Angewandte Chemie International Edition, 2005. **44**(19): p. 2892-2895.
52. de Meijere, K., G. Brezesinski, and H. Möhwald, *Polyelectrolyte Coupling to a Charged Lipid Monolayer.* Macromolecules, 1997. **30**(8): p. 2337-2342.
53. Fischlechner, M., et al., *Lipid layers on polyelectrolyte multilayer supports.* Soft Matter, 2008. **4**(11): p. 2245-2258.
54. Brittain, W.J. and S. Minko, *A structural definition of polymer brushes.* Journal of Polymer Science Part A: Polymer Chemistry, 2007. **45**(16): p. 3505-3512.
55. Ballauff, M. and O. Borisov, *Polyelectrolyte brushes.* Current Opinion in Colloid & Interface Science, 2006. **11**(6): p. 316-323.
56. Stuart, M.A.C., et al., *Emerging applications of stimuli-responsive polymer materials.* Nat Mater, 2010. **9**(2): p. 101-113.
57. Zhou, F. and W.T.S. Huck, *Surface grafted polymer brushes as ideal building blocks for "smart" surfaces.* Physical Chemistry Chemical Physics, 2006. **8**(33): p. 3815-3823.
58. Liu, X., et al., *Switching Water Droplet Adhesion Using Responsive Polymer Brushes.* Langmuir, 2010. **26**(14): p. 12377-12382.
59. Döbbelin, M., et al., *Tuning Surface Wettability of Poly(3-sulfopropyl methacrylate) Brushes by Cationic Surfactant-Driven Interactions.* Macromolecular Rapid Communications, 2008. **29**(11): p. 871-875.
60. Ballauff, M., *Spherical polyelectrolyte brushes.* Progress in Polymer Science, 2007. **32**(10): p. 1135-1151.
61. Ayres, N., *Polymer brushes: Applications in biomaterials and nanotechnology.* Polymer Chemistry, 2010. **1**(6): p. 769-777.
62. Lim, R.Y.H. and J. Deng, *Interaction Forces and Reversible Collapse of a Polymer Brush-Gated Nanopore.* Acs Nano, 2009. **3**(10): p. 2911-2918.

63. Comrie, J.E. and W.T.S. Huck, *Exploring Actuation and Mechanotransduction Properties of Polymer Brushes.* Macromolecular Rapid Communications, 2008. **29**(7): p. 539-546.
64. Binnig, G. and H. Rohrer, *SURFACE IMAGING BY SCANNING TUNNELING MICROSCOPY.* Ultramicroscopy, 1983. **11**(2-3): p. 157-160.
65. Eigler, D.M. and E.K. Schweizer, *Positioning single atoms with a scanning tunnelling microscope.* Nature, 1990. **344**(6266): p. 524-526.
66. Crommie, M.F., C.P. Lutz, and D.M. Eigler, *Confinement of Electrons to Quantum Corrals on a Metal Surface.* Science, 1993. **262**(5131): p. 218-220.
67. Binnig, G., C.F. Quate, and C. Gerber, *ATOMIC FORCE MICROSCOPE.* Physical Review Letters, 1986. **56**(9): p. 930-933.
68. Bustamante, C., J.C. Macosko, and G.J.L. Wuite, *Grabbing the cat by the tail: manipulating molecules one by one.* Nat Rev Mol Cell Biol, 2000. **1**(2): p. 130-136.
69. Bushell, G.R., et al., *Imaging and nano-dissection of tobacco mosaic virus by atomic force microscopy.* Journal of Microscopy, 1995. **180**(2): p. 174-181.
70. Ahn, S.J., et al., *AFM nanolithography on a mixed LB film of hexadecylamine and palmitic acid.* Ultramicroscopy, 2002. **91**(1–4): p. 171-176.
71. Senden, T. and W. Ducker, *Experimental Determination of Spring Constants in Atomic Force Microscopy.* Langmuir, 1994. **10**(4): p. 1003-1004.
72. Sader, J.E., J.W.M. Chon, and P. Mulvaney, *Calibration of rectangular atomic force microscope cantilevers.* Review of Scientific Instruments, 1999. **70**(10): p. 3967-3969.
73. Ducker, W.A., T.J. Senden, and R.M. Pashley, *Measurement of forces in liquids using a force microscope.* Langmuir, 1992. **8**(7): p. 1831-1836.
74. Cidade, G.A.G., et al., *Atomic Force Microscopy as a Tool for Biomedical and Biotechnological Studies.* Artificial Organs, 2003. **27**(5): p. 447-451.
75. Cohen, S.R. and A. Bitler, *Use of AFM in bio-related systems.* Current Opinion in Colloid & Interface Science, 2008. **13**(5): p. 316-325.
76. Hansma, H.G. and J.H. Hoh, *Biomolecular Imaging with the Atomic Force Microscope.* Annual Review of Biophysics and Biomolecular Structure, 1994. **23**(1): p. 115-140.
77. Kasas, S., et al., *Biological applications of the AFM: From single molecules to organs.* International Journal of Imaging Systems and Technology, 1997. **8**(2): p. 151-161.
78. Vansteenkiste, S.O., et al., *Scanning probe microscopy of biomedical interfaces.* Progress in Surface Science, 1998. **57**(2): p. 95-136.
79. Putman, C.A.J., et al., *Tapping mode atomic force microscopy in liquid.* Applied Physics Letters, 1994. **64**(18): p. 2454-2456.
80. Frederix, P.L.T.M., P.D. Bosshart, and A. Engel, *Atomic Force Microscopy of Biological Membranes.* Biophysical Journal, 2009. **96**(2): p. 329-338.
81. Mingeot-Leclercq, M.-P., et al., *Atomic force microscopy of supported lipid bilayers.* Nat. Protocols, 2008. **3**(10): p. 1654-1659.
82. Möller, C., et al., *Tapping-Mode Atomic Force Microscopy Produces Faithful High-Resolution Images of Protein Surfaces.* Biophysical Journal, 1999. **77**(2): p. 1150-1158.
83. Muller, D.J. and A. Engel, *Atomic force microscopy and spectroscopy of native membrane proteins.* Nat. Protocols, 2007. **2**(9): p. 2191-2197.
84. Ohnesorge, F.M., et al., *AFM review study on pox viruses and living cells.* Biophysical journal, 1997. **73**(4): p. 2183-2194.
85. Feiler, A., M.A. Plunkett, and M.W. Rutland, *Atomic Force Microscopy Measurements of Adsorbed Polyelectrolyte Layers. 1. Dynamics of Forces and Friction.* Langmuir, 2003. **19**(10): p. 4173-4179.

86. Spitzner, E.-C., C. Riesch, and R. Magerle, *Subsurface Imaging of Soft Polymeric Materials with Nanoscale Resolution.* Acs Nano, 2010. **5**(1): p. 315-320.
87. Leporatti, S., et al., *Scanning Force Microscopy Investigation of Polyelectrolyte Nano- and Microcapsule Wall Texture.* Langmuir, 2000. **16**(9): p. 4059-4063.
88. Kuznetsov, Y.G., et al., *Imaging of viruses by atomic force microscopy.* Journal of General Virology, 2001. **82**(9): p. 2025-2034.
89. Anselmetti, D., et al., *Single Molecule DNA Biophysics with Atomic Force Microscopy.* Single Molecules, 2000. **1**(1): p. 53-58.
90. Bezanilla, M., et al., *Motion and enzymatic degradation of DNA in the atomic force microscope.* Biophysical Journal, 1994. **67**(6): p. 2454-2459.
91. Allison, D.P., et al., *Direct atomic force microscope imaging of EcoRI endonuclease site specifically bound to plasmid DNA molecules.* Proceedings of the National Academy of Sciences, 1996. **93**(17): p. 8826-8829.
92. Milling, A. and S. Biggs, *Direct Measurement of the Depletion Force Using an Atomic Force Microscope.* Journal of Colloid and Interface Science, 1995. **170**(2): p. 604-606.
93. Milling, A., P. Mulvaney, and I. Larson, *Direct Measurement of Repulsive van der Waals Interactions Using an Atomic Force Microscope.* Journal of Colloid and Interface Science, 1996. **180**(2): p. 460-465.
94. Senden, T.J., C.J. Drummond, and P. Kekicheff, *Atomic Force Microscopy: Imaging with Electrical Double Layer Interactions.* Langmuir, 1994. **10**(2): p. 358-362.
95. Butt, H.-J., *Measuring electrostatic, van der Waals, and hydration forces in electrolyte solutions with an atomic force microscope.* Biophysical Journal, 1991. **60**(6): p. 1438-1444.
96. Butt, H.-J., M. Jaschke, and W. Ducker, *Measuring surface forces in aqueous electrolyte solution with the atomic force microscope.* Bioelectrochemistry and Bioenergetics, 1995. **38**(1): p. 191-201.
97. Heinz, W.F. and J.H. Hoh, *Spatially resolved force spectroscopy of biological surfaces using the atomic force microscope.* Trends in biotechnology, 1999. **17**(4): p. 143-150.
98. Xu, W., et al., *Atomic force microscope measurements of long-range forces near lipid-coated surfaces in electrolytes.* Biophysical Journal, 1997. **72**(3): p. 1404-1413.
99. Munday, J.N., F. Capasso, and V.A. Parsegian, *Measured long-range repulsive Casimir-Lifshitz forces.* Nature, 2009. **457**(7226): p. 170-173.
100. Noy, A., D.V. Vezenov, and C.M. Lieber, *CHEMICAL FORCE MICROSCOPY.* Annual Review of Materials Science, 1997. **27**(1): p. 381-421.
101. Florin, E., V. Moy, and H. Gaub, *Adhesion forces between individual ligand-receptor pairs.* Science, 1994. **264**(5157): p. 415-417.
102. Grandbois, M., et al., *How Strong Is a Covalent Bond?* Science, 1999. **283**(5408): p. 1727-1730.
103. Moy, V., E. Florin, and H. Gaub, *Intermolecular forces and energies between ligands and receptors.* Science, 1994. **266**(5183): p. 257-259.
104. Hugel, T. and M. Seitz, *The Study of Molecular Interactions by AFM Force Spectroscopy.* Macromolecular Rapid Communications, 2001. **22**(13): p. 989-1016.
105. Zhang, X., C. Liu, and Z. Wang, *Force spectroscopy of polymers: Studying on intramolecular and intermolecular interactions in single molecular level.* Polymer, 2008. **49**(16): p. 3353-3361.
106. Dufrene, Y.F., *Using nanotechniques to explore microbial surfaces.* Nat Rev Micro, 2004. **2**(6): p. 451-460.

107. Butt, H.-J., B. Cappella, and M. Kappl, *Force measurements with the atomic force microscope: Technique, interpretation and applications.* Surface Science Reports, 2005. **59**(1–6): p. 1-152.
108. Cui, S., et al., *Single Molecule Force Spectroscopy on Polyelectrolytes: Effect of Spacer on Adhesion Force and Linear Charge Density on Rigidity.* Macromolecules, 2004. **37**(3): p. 946-953.
109. Cui, S., et al., *Desorption Force per Polystyrene Segment in Water.* Macromolecules, 2003. **36**(11): p. 3779-3782.
110. Geisler, M., B.N. Balzer, and T. Hugel, *Polymer Adhesion at the Solid–Liquid Interface Probed by a Single–Molecule Force Sensor.* Small, 2009. **5**(24): p. 2864-2869.
111. Horinek, D., et al., *Peptide adsorption on a hydrophobic surface results from an interplay of solvation, surface, and intrapeptide forces.* Proceedings of the National Academy of Sciences, 2008. **105**(8): p. 2842-2847.
112. Hugel, T., et al., *Elasticity of Single Polyelectrolyte Chains and Their Desorption from Solid Supports Studied by AFM Based Single Molecule Force Spectroscopy.* Macromolecules, 2001. **34**(4): p. 1039-1047.
113. Kühner, F., et al., *Friction of Single Polymers at Surfaces.* Langmuir, 2006. **22**(26): p. 11180-11186.
114. Seitz, M., et al., *Probing Solid Surfaces with Single Polymers.* ChemPhysChem, 2003. **4**(9): p. 986-990.
115. Sonnenberg, L., et al., *Choose Sides: Differential Polymer Adhesion.* Langmuir, 2007. **23**(12): p. 6660-6666.
116. Friedsam, C., et al., *Polymer Functionalized AFM tips for Long-Term Measurements in Single-Molecule Force Spectroscopy.* ChemPhysChem, 2004. **5**(3): p. 388-393.
117. Bowen, W.R., R.W. Lovitt, and C.J. Wright, *Application of atomic force microscopy to the study of micromechanical properties of biological materials.* Biotechnology Letters, 2000. **22**(11): p. 893-903.
118. Chizhik, S.A., et al., *Micromechanical Properties of Elastic Polymeric Materials As Probed by Scanning Force Microscopy.* Langmuir, 1998. **14**(10): p. 2606-2609.
119. Domke, J. and M. Radmacher, *Measuring the Elastic Properties of Thin Polymer Films with the Atomic Force Microscope.* Langmuir, 1998. **14**(12): p. 3320-3325.
120. Ebenstein, D.M. and L.A. Pruitt, *Nanoindentation of biological materials.* Nano Today, 2006. **1**(3): p. 26-33.
121. Fang, T.-H., W.-J. Chang, and S.-L. Tsai, *Nanomechanical characterization of polymer using atomic force microscopy and nanoindentation.* Microelectronics Journal, 2005. **36**(1): p. 55-59.
122. Fraxedas, J., et al., *Nanoindentation: Toward the sensing of atomic interactions.* Proceedings of the National Academy of Sciences, 2002. **99**(8): p. 5228-5232.
123. Laney, D.E., et al., *Changes in the Elastic Properties of Cholinergic Synaptic Vesicles as Measured by Atomic Force Microscopy.* Biophysical Journal, 1997. **72**(2, Part 1): p. 806-813.
124. Lieber, S.C., et al., *Aging increases stiffness of cardiac myocytes measured by atomic force microscopy nanoindentation.* American Journal of Physiology - Heart and Circulatory Physiology, 2004. **287**(2): p. H645-H651.
125. Mermut, O., et al., *Structural and Mechanical Properties of Polyelectrolyte Multilayer Films Studied by AFM.* Macromolecules, 2003. **36**(23): p. 8819-8824.

126. Passeri, D., et al., *Indentation modulus and hardness of viscoelastic thin films by atomic force microscopy: A case study.* Ultramicroscopy, 2009. **109**(12): p. 1417-1427.
127. Pera, I., et al., *Using the Atomic Force Microscope to Study the Interaction between Two Solid Supported Lipid Bilayers and the Influence of Synapsin I.* Biophysical Journal, 2004. **87**(4): p. 2446-2455.
128. Schaap, I.A.T., et al., *Elastic Response, Buckling, and Instability of Microtubules under Radial Indentation.* Biophysical journal, 2006. **91**(4): p. 1521-1531.
129. de Pablo, P.J., et al., *Deformation and Collapse of Microtubules on the Nanometer Scale.* Physical Review Letters, 2003. **91**(9): p. 098101.
130. Delorme, N. and A. Fery, *Direct method to study membrane rigidity of small vesicles based on atomic force microscope force spectroscopy.* Physical Review E, 2006. **74**(3): p. 030901.
131. F. Dufrene, Y., et al., *Characterization of the physical properties of model biomembranes at the nanometer scale with the atomic force microscope.* Faraday Discussions, 1999. **111**: p. 79-94.
132. Landau, L.D. and E.M. Lifshitz, *Theory of Elasticity: Transl. from the Russian*. 1959.
133. Ivanovska, I.L., et al., *Bacteriophage capsids: Tough nanoshells with complex elastic properties.* Proceedings of the National Academy of Sciences of the United States of America, 2004. **101**(20): p. 7600-7605.
134. Michel, J.P., et al., *Nanoindentation studies of full and empty viral capsids and the effects of capsid protein mutations on elasticity and strength.* Proceedings of the National Academy of Sciences, 2006. **103**(16): p. 6184-6189.
135. Carrasco, C., et al., *DNA-mediated anisotropic mechanical reinforcement of a virus.* Proceedings of the National Academy of Sciences, 2006. **103**(37): p. 13706-13711.
136. Carrasco, C., et al., *Manipulation of the mechanical properties of a virus by protein engineering.* Proceedings of the National Academy of Sciences, 2008. **105**(11): p. 4150-4155.
137. Ivanovska, I., et al., *Internal DNA pressure modifies stability of WT phage.* Proceedings of the National Academy of Sciences, 2007. **104**(23): p. 9603-9608.
138. Kasas, S. and G. Dietler, *Probing nanomechanical properties from biomolecules to living cells.* Pflügers Archiv European Journal of Physiology, 2008. **456**(1): p. 13-27.
139. Kol, N., et al., *Mechanical Properties of Murine Leukemia Virus Particles: Effect of Maturation.* Biophysical Journal, 2006. **91**(2): p. 767-774.
140. Kol, N., et al., *A Stiffness Switch in Human Immunodeficiency Virus.* Biophysical Journal, 2007. **92**(5): p. 1777-1783.
141. Liashkovich, I., et al., *Exceptional mechanical and structural stability of HSV-1 unveiled with fluid atomic force microscopy.* Journal of Cell Science, 2008. **121**(14): p. 2287-2292.
142. Buenemann, M. and P. Lenz, *Mechanical limits of viral capsids.* Proceedings of the National Academy of Sciences, 2007. **104**(24): p. 9925-9930.
143. Šiber, A., *Buckling transition in icosahedral shells subjected to volume conservation constraint and pressure: Relations to virus maturation.* Physical Review E, 2006. **73**(6): p. 061915.
144. Vliegenthart, G. and G. Gompper, *Mechanical properties of icosahedral virus capsids.* Journal of Computer-Aided Materials Design, 2007. **14**(0): p. 111-119.
145. Vliegenthart, G.A. and G. Gompper, *Mechanical Deformation of Spherical Viruses with Icosahedral Symmetry.* Biophysical Journal, 2006. **91**(3): p. 834-841.
146. Zandi, R. and D. Reguera, *Mechanical properties of viral capsids.* Physical Review E, 2005. **72**(2): p. 021917.

147. Arkhipov, A., et al., *Elucidating the Mechanism behind Irreversible Deformation of Viral Capsids.* Biophysical Journal, 2009. **97**(7): p. 2061-2069.
148. Roos, W., et al., *Viral capsids: Mechanical characteristics, genome packaging and delivery mechanisms.* Cellular and Molecular Life Sciences, 2007. **64**(12): p. 1484-1497.
149. Roos, W.H. and G.J.L. Wuite, *Nanoindentation Studies Reveal Material Properties of Viruses.* Advanced Materials, 2009. **21**(10-11): p. 1187-1192.
150. Itano, M., et al., *Particle removal from silicon wafer surface in wet cleaning process.* Semiconductor Manufacturing, IEEE Transactions on, 1993. **6**(3): p. 258-267.
151. Li, J.K., R.M.A. Sullan, and S. Zou, *Atomic Force Microscopy Force Mapping in the Study of Supported Lipid Bilayers†.* Langmuir, 2010. **27**(4): p. 1308-1313.
152. Majidi, C., *Remarks on formulating an adhesion problem using Euler's elastica (draft).* Mechanics Research Communications, 2007. **34**(1): p. 85-90.
153. Majidi, C., *Shear adhesion between an elastica and a rigid flat surface.* Mechanics Research Communications, 2009. **36**(3): p. 369-372.
154. Behrens, S.H. and D.G. Grier, *The charge of glass and silica surfaces.* The Journal of Chemical Physics, 2001. **115**(14): p. 6716-6721.
155. Tsujii, Y., et al., *Structure and Properties of High-Density Polymer Brushes Prepared by Surface-Initiated Living Radical PolymerizationSurface-Initiated Polymerization I*, R. Jordan, Editor. 2006, Springer Berlin / Heidelberg. p. 1-45.
156. Barbey, R., et al., *Polymer Brushes via Surface-Initiated Controlled Radical Polymerization: Synthesis, Characterization, Properties, and Applications.* Chemical Reviews, 2009. **109**(11): p. 5437-5527.
157. O'Shea, S.J., M.E. Welland, and T. Rayment, *An atomic force microscope study of grafted polymers on mica.* Langmuir, 1993. **9**(7): p. 1826-1835.
158. Hayashi, S., et al., *Polyelectrolyte Brush Layers Studied by Surface Forces Measurement: Dependence on pH and Salt Concentrations and Scaling.* Langmuir, 2002. **18**(10): p. 3932-3944.
159. Abraham, T., et al., *Direct Measurements of Interactions between Hydrophobically Anchored Strongly Charged Polyelectrolyte Brushes.* Langmuir, 2000. **16**(9): p. 4286-4292.
160. Butt, H.-J., et al., *Steric Forces Measured with the Atomic Force Microscope at Various Temperatures.* Langmuir, 1999. **15**(7): p. 2559-2565.
161. Guffond, M.C., D.R.M. Williams, and E.M. Sevick, *End-Tethered Polymer Chains under AFM Tips: Compression and Escape in Theta Solvents.* Langmuir, 1997. **13**(21): p. 5691-5696.
162. Halperin, A. and E.B. Zhulina, *Atomic Force Microscopy of Polymer Brushes: Colloidal versus Sharp Tips.* Langmuir, 2010. **26**(11): p. 8933-8940.
163. Block, S. and C.A. Helm, *Measurement of long-ranged steric forces between polyelectrolyte layers physisorbed from 1M NaCl.* Physical Review E, 2007. **76**(3): p. 030801.
164. Drechsler, A., et al., *Interaction Forces between Microsized Silica Particles and Weak Polyelectrolyte Brushes at Varying pH and Salt Concentration.* Langmuir, 2009. **26**(9): p. 6400-6410.
165. Block, S. and C.A. Helm, *Conformation of Poly(styrene sulfonate) Layers Physisorbed from High Salt Solution Studied by Force Measurements on Two Different Length Scales.* The Journal of Physical Chemistry B, 2008. **112**(31): p. 9318-9327.
166. Pincus, P., *Colloid stabilization with grafted polyelectrolytes.* Macromolecules, 1991. **24**(10): p. 2912-2919.

167. Pesavento, J.B., et al., *Structures of Rotavirus Reassortants Demonstrate Correlation of Altered Conformation of the VP4 Spike and Expression of Unexpected VP4-Associated Phenotypes.* Journal of Virology, 2003. **77**(5): p. 3291-3296.
168. Smith, A.E. and A. Helenius, *How Viruses Enter Animal Cells.* Science, 2004. **304**(5668): p. 237-242.
169. Zlotnick, A., *Are weak protein–protein interactions the general rule in capsid assembly?* Virology, 2003. **315**(2): p. 269-274.
170. Bruinsma, R.F., et al., *Viral Self-Assembly as a Thermodynamic Process.* Physical Review Letters, 2003. **90**(24): p. 248101.
171. Baker, T.S., N.H. Olson, and S.D. Fuller, *Adding the Third Dimension to Virus Life Cycles: Three-Dimensional Reconstruction of Icosahedral Viruses from Cryo-Electron Micrographs.* Microbiology and Molecular Biology Reviews, 2000. **64**(1): p. 237.
172. Smith, D.E., et al., *The bacteriophage [phis]29 portal motor can package DNA against a large internal force.* Nature, 2001. **413**(6857): p. 748-752.
173. Caspar, D.L.D. and A. Klug, *Physical Principles in the Construction of Regular Viruses.* Cold Spring Harbor Symposia on Quantitative Biology, 1962. **27**: p. 1-24.
174. Twarock, R., *Mathematical virology: a novel approach to the structure and assembly of viruses.* Philosophical Transactions of the Royal Society A: Mathematical, Physical and Engineering Sciences, 2006. **364**(1849): p. 3357-3373.
175. Lidmar, J., L. Mirny, and D.R. Nelson, *Virus shapes and buckling transitions in spherical shells.* Physical Review E, 2003. **68**(5): p. 051910.
176. Söderlund, H., et al., *Properties of Semliki Forest virus nucleocapsid: II. An irreversible contraction by acid pH.* Virology, 1972. **47**(3): p. 753-760.
177. Pesavento , J.B., et al., *pH-Induced Conformational Change of the Rotavirus VP4 Spike: Implications for Cell Entry and Antibody Neutralization.* Journal of Virology, 2005. **79**(13): p. 8572-8580.
178. Dimitrov, D.S., *Virus entry: molecular mechanisms and biomedical applications.* Nat Rev Micro, 2004. **2**(2): p. 109-122.
179. Mukherjee, S., et al., *A Quantitative Description of In Vitro Assembly of Human Papillomavirus 16 Virus-Like Particles.* Journal of Molecular Biology, 2008. **381**(1): p. 229-237.
180. Lavelle, L., J.-P. Michel, and M. Gingery, *The disassembly, reassembly and stability of CCMV protein capsids.* Journal of Virological Methods, 2007. **146**(1–2): p. 311-316.
181. Bancroft, J.B., G.J. Hills, and R. Markham, *A study of the self-assembly process in a small spherical virus formation of organized structures from protein subunits in vitro.* Virology, 1967. **31**(2): p. 354-379.
182. Noad, R. and P. Roy, *Virus-like particles as immunogens.* Trends in Microbiology, 2003. **11**(9): p. 438-444.
183. Cadena-Nava, R.D., et al., *Exploiting Fluorescent Polymers To Probe the Self-Assembly of Virus-like Particles.* The Journal of Physical Chemistry B, 2011. **115**(10): p. 2386-2391.
184. Ren, Y., S.-M. Wong, and L.-Y. Lim, *In vitro-reassembled plant virus-like particles for loading of polyacids.* Journal of General Virology, 2006. **87**(9): p. 2749-2754.
185. Uchida, M., et al., *Biological Containers: Protein Cages as Multifunctional Nanoplatforms.* Advanced Materials, 2007. **19**(8): p. 1025-1042.
186. Donaldson, E.F., et al., *Norovirus pathogenesis: mechanisms of persistence and immune evasion in human populations.* Immunological Reviews, 2008. **225**(1): p. 190-211.

187. Hardy, M.E., *Norovirus protein structure and function.* FEMS Microbiology Letters, 2005. **253**(1): p. 1-8.
188. Bu, W., et al., *Structural Basis for the Receptor Binding Specificity of Norwalk Virus.* Journal of Virology, 2008. **82**(11): p. 5340-5347.
189. Bertolotti-Ciarlet, A., et al., *Structural Requirements for the Assembly of Norwalk Virus-Like Particles.* Journal of Virology, 2002. **76**(8): p. 4044-4055.
190. Jiang, X., et al., *Expression, self-assembly, and antigenicity of the Norwalk virus capsid protein.* Journal of Virology, 1992. **66**(11): p. 6527-6532.
191. Prasad, B.V., et al., *Three-dimensional structure of baculovirus-expressed Norwalk virus capsids.* Journal of Virology, 1994. **68**(8): p. 5117-5125.
192. Prasad, B.V.V., et al., *X-ray Crystallographic Structure of the Norwalk Virus Capsid.* Science, 1999. **286**(5438): p. 287-290.
193. Chen, R., et al., *Inter- and Intragenus Structural Variations in Caliciviruses and Their Functional Implications.* Journal of Virology, 2004. **78**(12): p. 6469-6479.
194. White, L.J., M.E. Hardy, and M.K. Estes, *Biochemical characterization of a smaller form of recombinant Norwalk virus capsids assembled in insect cells.* Journal of Virology, 1997. **71**(10): p. 8066-72.
195. Donaldson, E.F., et al., *Viral shape-shifting: norovirus evasion of the human immune system.* Nat Rev Micro, 2010. **8**(3): p. 231-241.
196. Risco, C., J.L. Carrascosa, and T.K. Frey, *Structural maturation of rubella virus in the Golgi complex.* Virology, 2003. **312**(2): p. 261-269.
197. Best, J., et al., *MORPHOLOGICAL CHARACTERISTICS OF RUBELLA VIRUS.* The Lancet, 1967. **290**(7509): p. 237-239.
198. Lee, J.-Y. and D.S. Bowden, *Rubella Virus Replication and Links to Teratogenicity.* Clinical Microbiology Reviews, 2000. **13**(4): p. 571-587.
199. Frey, T.K., *Molecular Biology of Rubella Virus*, in *Advances in Virus Research*, F.A.M. Karl Maramorosch and J.S. Aaron, Editors. 1994, Academic Press. p. 69-160.
200. Oker-Blom, C., et al., *Rubella virus contains one capsid protein and three envelope glycoproteins, E1, E2a, and E2b.* Journal of Virology, 1983. **46**(3): p. 964-973.
201. von Bonsdorff, C.-H. and A. Vaheri, *Growth of Rubella Virus in BHK 21 Cells: Electron Microscopy of Morphogenesis.* Journal of General Virology, 1969. **5**(1): p. 47-48,NP1-NP3,49-51.
202. Petruzziello, R., et al., *Pathway of rubella virus infectious entry into Vero cells.* Journal of General Virology, 1996. **77**(2): p. 303-308.
203. Katow, S. and A. Sugiura, *Low pH-induced Conformational Change of Rubella Virus Envelope Proteins.* Journal of General Virology, 1988. **69**(11): p. 2797-2807.
204. Käsermann, F. and C. Kempf, *Low pH-induced pore formation by spike proteins of enveloped viruses.* Journal of General Virology, 1996. **77**(12): p. 3025-3032.
205. Mauracher, C.A., et al., *pH-dependent solubility shift of rubella virus capsid protein.* Virology, 1991. **181**(2): p. 773-777.
206. Hitchman, R.B., R.D. Possee, and L.A. King, *Baculovirus Expression Systems for Recombinant Protein Production in Insect Cells.* Recent Patents on Biotechnology, 2009. **3**(1): p. 46-54.
207. Mourez, T., et al., *Baculovirus expression of HCoV-OC43 nucleocapsid protein and development of a Western blot assay for detection of human antibodies against HCoV-OC43.* Journal of Virological Methods, 2007. **139**(2): p. 175-180.

208. Hobman, T.C., et al., *Assembly of Rubella Virus Structural Proteins into Virus-like Particles in Transfected Cells.* Virology, 1994. **202**(2): p. 574-585.
209. Mannige, R.V. and C.L. Brooks, *Geometric considerations in virus capsid size specificity, auxiliary requirements, and buckling.* Proceedings of the National Academy of Sciences, 2009. **106**(21): p. 8531-8536.
210. Ausar, S.F., et al., *Conformational Stability and Disassembly of Norwalk Virus-like Particles.* Journal of Biological Chemistry, 2006. **281**(28): p. 19478-19488.
211. Tan, M., R.S. Hegde, and X. Jiang, *The P Domain of Norovirus Capsid Protein Forms Dimer and Binds to Histo-Blood Group Antigen Receptors.* Journal of Virology, 2004. **78**(12): p. 6233-6242.
212. Gibbons, M.M. and W.S. Klug, *Nonlinear finite-element analysis of nanoindentation of viral capsids.* Physical Review E, 2007. **75**(3): p. 031901.
213. Klug, W.S., et al., *Failure of Viral Shells.* Physical Review Letters, 2006. **97**(22): p. 228101.
214. Donath, E., *Biosensors: Viruses for ultrasensitive assays.* Nat Nano, 2009. **4**(4): p. 215-216.
215. Radmacher, M., et al., *Imaging adhesion forces and elasticity of lysozyme adsorbed on mica with the atomic force microscope.* Langmuir, 1994. **10**(10): p. 3809-3814.
216. Liang, X., G. Mao, and K.Y. Simon Ng, *Probing small unilamellar EggPC vesicles on mica surface by atomic force microscopy.* Colloids and Surfaces B: Biointerfaces, 2004. **34**(1): p. 41-51.
217. Enzmann, P.J. and F. Weiland, *Studies on the morphology of alphaviruses.* Virology, 1979. **95**(2): p. 501-510.
218. Zhang, W., et al., *Placement of the Structural Proteins in Sindbis Virus.* Journal of Virology, 2002. **76**(22): p. 11645-11658.
219. Mancini, E.J., et al., *Cryo-Electron Microscopy Reveals the Functional Organization of an Enveloped Virus, Semliki Forest Virus.* Molecular cell, 2000. **5**(2): p. 255-266.
220. Li, S., et al., *Bending and Puncturing the Influenza Lipid Envelope.* Biophysical journal, 2011. **100**(3): p. 637-645.
221. Eghiaian, F., et al., *The Influenza Virus Mechanical Properties Are Dominated By Its Lipid Envelope.* Biophysical journal, 2009. **96**(3, Supplement 1): p. 15a.
222. Murphy, F.A., P.E. Halonen, and A.K. Harrison, *Electron microscopy of the development of rubella virus in BHK-21 cells.* Journal of Virology, 1968. **2**(10): p. 1223-1227.

Parts of this Work are Published or is to be Published in

Cuellar, J.L., Meinhoevel, F., Hoehne, M., Donath, E., 2010. *Size and mechanical stability of Norovirus capsids depend on pH: a nanoindentation study.* Journal of General Virology. 91, 2449-2456.

J.L. Cuéllar and E. Donath (2012). *Force Microscopy – A Tool to Elucidate the Relationship Between Nanomechanics and Function in Viruses*, Atomic Force Microscopy Investigations into Biology - From Cell to Protein, Christopher L. Frewin (Ed.), ISBN: 978-953-51-0114-7, InTech,

Martin Fischlechner, Markus Zaulig, Stefan Meyer, Irina Estrela-Lopis, **Luis Cuéllar**, Joseba Irigoyen, Paula Pescador, Milan Brumen, Paul Messner, Sergio Moya and Edwin Donath. *Lipid layers on polyelectrolyte multilayer supports*. Soft Matter. 2008. 4(11). p. 2245-2258.

Publications in progress.

Luis Cuellar, Iturri Jagoba, Llarena Irantzu, Moya Sergio and Edwin Donath. ***"****Atomic Force Spectroscopy studies of highly charged Poly sulfo propyl methacrylate polyelectrolyte brushes under variable ionic strength conditions****".***

Luis Cuellar, Beruda Thomas, Pescador Paula and Edwin Donath. *"Polyelectrolyte-Lipid interactions probed by single molecule force spectroscopy".*

Luis Cuellar, Fischlechner Martin, Koehler Guido and Edwin Donath.
"*Mechanical Properties of Rubella-Like particles: Modulation of Capsid Elasticity by Viral Envelope".*